Theoretical and Analytical Investigation of Electromagnetic Problems Using Dispersive Material and the Kramers-Kronig Transformations

Dissertation

zur Erlangung des akademischen Grades eines Doktors der Ingenieurwissenschaften (Dr.-Ing.)

der Christian-Albrechts-Universität zu Kiel

vorgelegt von

Mostafa Mohamed Bakry Mohamed

aus

Qena, Ägypten

Jahr

2022

1. Gutachter:	Prof. Dr.-Ing. Ludger Klinkenbusch
2. Gutachter:	Prof. Dr.-Ing. Michael Höft
Prüfungsdatum:	27.01.2023

Abstract

In reality, there is no material with constant permittivity, permeability, and conductivity values over the entire frequency spectrum. The variation in these parameters is well-known as the dispersion phenomenon, which can be analytically interpreted using the Kramers-Kronig relations. Through this thesis, we extensively explain how to take advantage of the dispersion in these parameters to numerically investigate some electromagnetic problems. Among these is a practical problem of separating the electric conductive losses from the dielectric losses of any dispersive lossy material. On the other hand, the performance of particular electrically small antennas is improved by exploiting the frequency dispersion in the dielectric and magnetic material. Electrically small antennas have great attention in many applications due to their drastically reduced size. However, the size reduction comes at the expense of performance degradation, such as increasing the internally stored electromagnetic energy, narrowing the operating bandwidth, decreasing radiation efficiency, and poor matching to surrounding media, particularly when the antenna element has direct contact with a lossy medium like biomedical tissues. Therefore, we try to numerically investigate the performance of these antennas by coating them with dispersive dielectric or magnetic material. For this purpose, the multipole spherical expansion method has been proposed to describe the radiated electromagnetic field everywhere around the electrically small antenna element. By utilizing this method, it is possible to obtain the optimum values of the permittivity and permeability of the material used to enhance the antenna's performance. In this thesis, some artificially synthesized material with frequency-dependent permittivity, permeability, and electric conductivity values over a wide range of frequencies are suggested to represent the dispersive lossy material. The Kramers-Kronig (KK) relations are employed as a mathematical solution to interrelate the real and imaginary parts of the suggested frequency-dependent relative permittivity and permeability values of the artificial material. Finally, the solution methods are verified by applying them to real-world material found in the literature.

Zusammenfassung

In der Realität gibt es kein Material mit konstanten Permittivitäts-, Permeabilitäts- und Leitfähigkeitswerten über das gesamte Frequenzspektrum. Die Streuung dieser Parameter ist als Dispersionsphänomen bekannt, das durch die Kramers-Kronig Relationen analytisch interpretiert werden kann. Durch diese Dissertation wird ausführlich erklärt, wie man die Streuung in diesen Parametern ausnutzt, um einige elektromagnetische Probleme numerisch untersuchen zu können. Unter diesen Problemen ist das praktische Problem der Trennung der elektrischen Leitfähigkeitsverluste von den dielektrischen Verlusten eines dispersiven verlustbehafteten Materials. Andererseits wird die Leistung insbesondere elektrisch kleiner Antennen verbessert, indem die Dispersion in dielektrischen und magnetischen Materialien ausgenutzt wird. Elektrisch kleine Antennen haben aufgrund ihrer drastisch reduzierten Größe in vielen Anwendungen große Aufmerksamkeit gefunden. Die Größenreduzierung resultiert jedoch in einer Leistungsverschlechterung, wie zum Beispiel der Erhöhung der gespeicherten elektromagnetischen Energie, der Reduktion der Betriebsbandbreite, der Verringerung der Leistungsfähigkeit, und einer schlechten Anpassung an die umgebenden Medien, vornehmlich wenn das Antennenelement direkten Kontakt mit einem verlustbehafteten Material, wie beispielsweise biologische Gewebe hat. Infolgedessen wird versucht die Leistung solcher Antennen numerisch zu untersuchen, indem sie in dispersives dielektrisches oder magnetisches Material eingeschlossen werden. Zu diesem Zweck wurde die sphärische Multipolentwicklung vorgeschlagen, um die abgestrahlten elektromagnetischen Felder überall um das elektrisch kleine Antennenelement herum zu berechnen. Durch Anwendung dieser Methode ist es möglich, die optimalen Werte von Permittivität und Permeabilität der verwendeten Materialien zu berechnen, um die Leistung der Antenne zu verbessern. In dieser Dissertation werden zuerst unechte Materialien mit frequenzabhängigen Permittivitäts-, Permeabilitäts- und Leitfähigkeitswerten über einen breiten Frequenzbereich vorgeschlagen, um das dispersive verlustbehaftete Material darzustellen. Danach werden die Kramers-Kronig (KK) Relationen als mathematische Lösung verwendet, um die Real- und Imaginärteile der frequenzabhängigen Permittivitäts- und Permeabilitätswerte des verwendeten Materials miteinander in Beziehung zu setzen. Abschließend werden die Lösungsmethoden verifiziert, indem sie auf in der Literatur gefundene natürliche Materialien angewendet werden.

Acknowledgement

First and foremost I want to thank my supervisor Prof. Dr.-Ing. Ludger Klinkenbusch. It has been an honour to be one of his Ph.D. students. I appreciate all his contributions of time, ideas, and recommendations to make my doctoral studies productive and stimulating. I would also like to express my sincere gratitude to my mother for her prayers, my wife and my daughter for their patience and their support throughout my Ph.D. study. I can not forget to thank my colleagues in the chair of Computational Electromagnetics for all the unconditional support in this academic work. My sincere gratitude to my brothers, my friends, and for any one who consciously or unconsciously motivated me throughout my Ph.D.

Furthermore, many thanks to the German Academic Exchange Service (DAAD) and the German-Egyptian Research Long-Term Scholarship (GERLS) for funding my Ph.D. project and letting me be a part of this incredible leaders' network.

Contents

1. Introduction

Most of the natural and manufactured materials, such as composite materials, and biological tissues, have dispersion in their permittivity and permeability values [1–6]. Although the dispersion in these values degrades material's quality in some applications, it can be an advantage in many others, e.g., in electromagnetic absorbers with band-gap structures [7], frequency selective surfaces [8], [9], or composite materials [10–12], the frequency dispersion in permittivity and permeability values is essential in broadening the frequency range over which the electromagnetic absorption occurs. Yaghjian [13] investigated the effect of the dispersion in materials to increase the operating bandwidth of electrically small antennas, where the lower bounds of the antenna's quality factor was halved using lumped elements containing highly dispersive dielectric or magnetic material. Arbabi *et al.* [14] evaluated the optimum gain of an electrically small antenna containing lossy material. In [15], [16], the electrically small dipole antenna was matched to a lossy medium by circumscribing the antenna element with a meta-material. In biomedical applications like thermal, radiation, and chemical therapies, electromagnetic devices like antennas [17] or biosensors [18] are utilized in direct or indirect contact with the biological tissues, the compatibility between the bio-tissue and the utilized device is essential. Bio-tissues are frequency-dependent materials and show dispersion in their permittivity and conductivity values over the entire frequency spectrum [19]. Therefore, unavoidable reflections of the radiated electromagnetic waves or complexity in measurements arise due to the frequency dispersion in biological tissues [20]. Consequently, determining the permittivity and conductivity values over a particular frequency range is essential in determining the optimum method of measurements in biomedical applications [21]. However, in practice, predicting the frequency dispersion in materials is not a trivial task and relies on many factors, e.g., the weighting factor is essential in composite materials to get the desired dispersion in permittivity and permeability values [10], [22]. Therefore, we take advantage of dispersive materials and employ them in electromagnetic problems.

1.1 The Objective of the Thesis

In this dissertation, we investigate the dielectric and magnetic materials dispersion and its effect on some electromagnetic problems. Among these problems is the poor matching between electrically small antennas and biological tissues in biomedical applications. Since the antenna element is placed close to or interior of a dispersive biological tissue, most of the radiated electromagnetic energy is scattered and reflected away from the antenna, degrading its performance [23]. Consequently, we strive to handle this problem by enclosing the antenna with a highly dispersive lossy dielectric material to improve the matching between

the antenna and the surrounding biological tissue.

Additionally, the high increase in the stored electric energy of the electrically small disk monopole antenna reduces the antenna's radiation resistance and efficiency and increases its quality factor, leading to a degradation of the antenna performance. Therefore, we enclose the antenna with a highly dispersive magnetic material to reduce the stored electric energy, increase the radiation resistance, and improve its performance.

Moreover, the practical problem of separating the electric conductivity from the complex-valued relative permittivity in dispersive materials is another problem that is extensively discussed in this thesis. For this purpose, some artificially synthesized materials with randomly selected values of permittivity and permeability are assumed to represent the dispersive lossy material.

1.2 Thesis Structure

The Thesis is organized as follows:

- Maxwell's equations and the spherical multipole expansion of the electromagnetic fields, along with some concepts and constitutive relations in electromagnetics utilized through the thesis, are discussed in detail in Chapter 2. Moreover, the dispersion relations known as the Kramers-Kronig (KK) relations and the solution method of their integral equations are extensively discussed in this chapter. The Kramers-Kronig relations are unique integral equations that interrelate the real and imaginary parts of any complex-valued function describing a causal system. Finally, the obtained solution method of the KK integrations will be used throughout the thesis to verify the consistency between the real and imaginary parts of the artificially synthesized lossy material.

- While measuring the effective permittivity of dispersive material, it may be interesting to distinguish between conductivity losses (caused by free electrons) and dielectric losses (caused by bounded electrons), which are included in the imaginary part. This usually turns out to be a non-trivial task unless suitable dispersion models for the dielectric and the conductivity properties of the material are assumed. In Chapter 3, we present a more general method based on the Kramers-Kronig transformations described in Chapter 2 to separate the electric conductivity from the effective complex permittivity of a dispersive lossy material. The proposed method is tested by first assuming some fictitious values of the complex permittivity satisfying the KK-transformations. After that, different conductivity values are added, changing the imaginary part of the effective permittivity while the real part remains the same. The effective permittivity (including a conductivity part) does generally not satisfy the KK-transformations. This fact will be employed to retrieve the conductivity from that effective complex permittivity. Finally, the method is applied to measured values quoted from the literature to retrieve the conductivity from the effective permittivity

of composite materials.

- In biomedical applications like radiation therapy or thermal therapy, antennas are utilized to transmit electromagnetic energy in the human body [24]. However, the direct contact between the antenna element and the biological tissues degrades the antenna's performance due to the reflections of the transmitted fields, leading to a poor matching between the antenna element and the surrounding bio-tissue. In Chapter 4, we suggest a method to get the optimum matching between the antenna and the surrounding bio-tissue. The antenna element is placed in the center of a multi-layered sphere. The outer sphere is filled with the bio-tissue, while the middle sphere contains the dispersive lossy dielectric material. The radiated electromagnetic fields by the antenna element are represented by the spherical multipole expansion method. This method calculates the optimum permittivity and permeability values of the dispersive lossy material required to match the antenna element to the biological tissue.

- Chapter 5 investigates the effect of the dispersive magnetic material on the performance of the electrically small disk monopole antenna [25]. The capacitive loading of the upper disk of this antenna drastically increases the stored electric energy, decreasing the radiation resistance and increasing the antenna's quality factor. In this chapter, we extensively discussed the published paper [25] on improving the performance of the disk monopole antenna by enclosing it with a highly dispersive magnetic material. The optimum permeability values of the magnetic material, leading to the optimum performance, are analytically calculated depending on the geometrical dimensions of the antenna and the magnetic material. The obtained results are then numerically verified using the frequency-domain solver CST©.

MATLAB© software and the frequency-domain solver CST© provided by the chair of Computational Electromagnetics in the Faculty of Engineering, Kiel University are utilized for most of the obtained results through the thesis.

2. Kramers-Kronig Transformations and Spherical Multipole Expansion

This chapter outlines the fundamental relations and concepts of the electromagnetic fields and their spherical multipole expansion that will be utilized in the rest of this thesis. Additionally, it explains the frequency dispersion phenomenon in linear and homogeneous dielectric and magnetic materials. This phenomenon arises due to the non-local temporal connection between the incident electric fields $\vec{E}$ and $\vec{D}$ or the magnetic fields $\vec{H}$ and $\vec{B}$ on any dielectric or magnetic material. This leads to a temporal frequency dispersion in the values of the material parameters such as permittivity ε, permeability μ and conductivity σ provided the causality connection between the incident fields and the material polarization exists [26]. Consequently, some effects arise from the dispersion in the values of ε and μ. For instance, the real and the imaginary parts of ε and μ are interrelated by the Kramers-Kronig relations. The latter will be the most crucial part of this chapter. Moreover, the derivation and the solution methods of the integrals representing these relations are discussed in detail.

2.1 Maxwell Equations

The Maxwell equations describe the relations between the electric field intensity $\vec{E}$, the magnetic field intensity $\vec{H}$, the electric flux density $\vec{D}$, the magnetic flux density $\vec{B}$, the electric current density $\vec{J}_e$, and the electric charge density ϱ in time t and space $\vec{r}$ [26]- [27]. If we adopt the SI units, the Maxwell equations can be represented in time-domain as follows

$$\vec{\nabla} \times \vec{E}(\vec{r},t) = -\frac{\partial}{\partial t}\vec{B}(\vec{r},t) \tag{2.1a}$$

$$\vec{\nabla} \times \vec{H}(\vec{r},t) = \frac{\partial}{\partial t}\vec{D}(\vec{r},t) + \vec{J}_e(\vec{r},t) \tag{2.1b}$$

$$\vec{\nabla} \cdot \vec{D}(\vec{r},t) = \varrho(\vec{r},t) \tag{2.1c}$$

$$\vec{\nabla} \cdot \vec{B}(\vec{r},t) = 0. \tag{2.1d}$$

We Assume the phasor $\vec{F}(\vec{r})$ of a time harmonic function $\vec{F}(\vec{r},t)$ with a positive time notation $e^{j\omega t}$ is defined and omitted throughout this thesis, in the usual form as

$$\vec{F}(\vec{r},t) = \mathrm{Re}\{\vec{F}(\vec{r})e^{j\omega t}\}. \tag{2.2}$$

By applying the Fourier transforms [26] on (2.1), the set of Maxwell equations can be rewritten in the phasor-domain as

$$\vec{\nabla} \times \vec{E}(\vec{r},\omega) = -j\omega\vec{B}(\vec{r},\omega) \tag{2.3a}$$
$$\vec{\nabla} \times \vec{H}(\vec{r},\omega) = j\omega\vec{D}(\vec{r},\omega) + \vec{J}_e(\vec{r},\omega) \tag{2.3b}$$
$$\vec{\nabla} \cdot \vec{D}(\vec{r},\omega) = \varrho(\vec{r},\omega) \tag{2.3c}$$
$$\vec{\nabla} \cdot \vec{B}(\vec{r},\omega) = 0, \tag{2.3d}$$

where ω is the angular frequency. The electric and magnetic flux densities are related to the electric and magnetic field intensities according to

$$\vec{D}(\vec{r},\omega) = \varepsilon_0\vec{E}(\vec{r},\omega) + \vec{P}(\vec{r},\omega) \tag{2.4a}$$
$$\vec{B}(\vec{r},\omega) = \mu_0\vec{H}(\vec{r},\omega) + \vec{M}(\vec{r},\omega) \tag{2.4b}$$
$$\vec{J}_e(\vec{r},\omega) = \sigma_e(\omega)\vec{E}(\vec{r},\omega) + \vec{J}_e^{\,imp}(\vec{r},\omega), \tag{2.4c}$$

respectively. Where σ_e is the electric conductivity, ε_0 and μ_0 are the free space permittivity and permeability, respectively, and $\vec{J}_e^{\,imp}$ is the impressed electric current. The second parts of the right side in (2.4a) and (2.4b) are the material polarization $\vec{P}$ and magnetization $\vec{M}$, respectively. They are generally defined in terms of the microscopically bound charges and the currents in the material [26] and related to the fields $\vec{E}$ and $\vec{H}$ as

$$\vec{P}(\vec{r},\omega) = \varepsilon_0\chi_e(\omega)\vec{E}(\vec{r},\omega) \tag{2.5a}$$
$$\vec{M}(\vec{r},\omega) = \mu_0\chi_m(\omega)\vec{H}(\vec{r},\omega), \tag{2.5b}$$

where χ_e and χ_m are the electric and magnetic susceptibilities. Generally, the functions χ_e and χ_m can be real-valued or frequency-dependent (complex-valued) depending on the electric and magnetic losses, respectively. Throughout this thesis, frequency-dependent values for these quantities will be assumed. Substituting (2.5) into (2.4), we may write

$$\vec{D}(\vec{r},\omega) = \varepsilon_0\varepsilon_r(\omega)\vec{E}(\vec{r},\omega) \tag{2.6a}$$
$$\vec{B}(\vec{r},\omega) = \mu_0\mu_r(\omega)\vec{H}(\vec{r},\omega), \tag{2.6b}$$

where the relative permittivity ε_r and the relative permeability μ_r are defined as

$$\varepsilon_r(\omega) = 1 + \chi_e(\omega) \tag{2.7a}$$
$$\mu_r(\omega) = 1 + \chi_m(\omega), \tag{2.7b}$$

respectively. Since the susceptibilities are considered complex functions, Eq. (2.7) is recast as

$$\varepsilon_r(\omega) = \varepsilon'(\omega) - j\varepsilon''(\omega) \qquad \{\varepsilon', \varepsilon''\} \in \mathbb{R} \tag{2.8a}$$
$$\mu_r(\omega) = \mu'(\omega) - j\mu''(\omega) \qquad \{\mu', \mu''\} \in \mathbb{R}. \tag{2.8b}$$

The real parts of (2.8a) and (2.8b) refer to the material polarization and magnetization, whereas the imaginary parts denote the dielectric and magnetic losses. In the following sections, it will be shown that the real and the imaginary parts of (2.8) are interrelated by the integral formulas of the dispersion relations, which are also known as the Kramers-Kronig relations.

2.2 Basic Solutions of the Vectorial Homogeneous Helmholtz Equations in Spherical Coordinates

Applying the curl on both sides of equations (2.3)a and (2.3)b and after some simplifications, the vectorial differential equations of $\vec{E}$ and $\vec{H}$ are written according to [28] as

$$\vec{\nabla} \times \vec{\nabla} \times \vec{E}(\vec{r},\omega) - \kappa^2 \vec{E}(\vec{r},\omega) = -j\omega\mu \vec{J}_e^{imp}(\vec{r},\omega) - \vec{\nabla} \times \vec{J}_m^{imp}(\vec{r},\omega) \tag{2.9a}$$

$$\vec{\nabla} \times \vec{\nabla} \times \vec{H}(\vec{r},\omega) - \kappa^2 \vec{H}(\vec{r},\omega) = -j\omega\varepsilon \vec{J}_m^{imp}(\vec{r},\omega) + \vec{\nabla} \times \vec{J}_e^{imp}(\vec{r},\omega), \tag{2.9b}$$

where the wavenumber κ is a frequency dependent quantity

$$\kappa(\omega) = \omega\sqrt{\varepsilon(\omega)\mu(\omega)}. \tag{2.10}$$

We are interested in solving (2.9) with no impressed electric or magnetic currents ($\vec{J}_e^{im} = \vec{J}_m^{imp} = 0$). Thus, the vectorial differential equation is rewritten as

$$\vec{\nabla} \times \vec{\nabla} \times \vec{F}(\vec{r},\omega) - \kappa^2 \vec{F}(\vec{r},\omega) = 0. \tag{2.11}$$

Equation (2.11) can be simplified through the use of vector identity $\nabla^2\vec{F} = \vec{\nabla}\vec{\nabla}\cdot\vec{F} - \vec{\nabla}\times\vec{\nabla}\times\vec{F}$ as

$$\nabla^2 \vec{F}(\vec{r},\omega) + \kappa^2 \vec{F}(\vec{r},\omega) = 0, \tag{2.12}$$

where the divergence of the vector function $\vec{\nabla} \cdot \vec{F} = 0$ for a homogeneous medium with $\kappa \neq 0$. Equation (2.12) is known as the homogeneous vectorial Helmholtz equation and has two independent vector solutions defined as

$$\vec{M}(\vec{r}) = \left(\vec{r} \times \vec{\nabla}\right)\Psi(r) \tag{2.13a}$$

$$\vec{N}(\vec{r}) = \left[\frac{1}{\kappa}\vec{\nabla} \times (\vec{r} \times \vec{\nabla})\right]\Psi(\vec{r}). \tag{2.13b}$$

These solutions apply only if the scalar function $\Psi(\vec{r})$ is a solution of the scalar Helmholtz differential equation

$$\nabla^2\Psi(\vec{r}) + \kappa^2\Psi(\vec{r}) = 0. \tag{2.14}$$

Using the vector identity of ∇^2 in spherical coordinates [26], the Helmholtz equation (2.14) can be solved using separation of variables $\Psi(r,\vartheta,\varphi) = z(r)Y(\vartheta,\varphi)$. The radial equation takes the form

$$\frac{d}{dr}\left(r^2\frac{d}{dr}z_v(\kappa r)\right) + \left[(\kappa r)^2 - v(v+1)^2\right]z_v(\kappa r) = 0, \tag{2.15}$$

while the transversal part is a solution of the eigenvalue equation of the surface spherical harmonics and is written as

$$-(\vec{r} \times \vec{\nabla})^2 Y_v(\vartheta,\varphi) = v(v+1)Y_v(\vartheta,\varphi), \tag{2.16}$$

with the operator

$$(\vec{r} \times \vec{\nabla})^2 = \frac{1}{\sin\vartheta}\frac{\partial}{\partial\vartheta}(\sin\vartheta\frac{\partial}{\partial\vartheta}) + \frac{1}{\sin^2\vartheta}\frac{\partial^2}{\partial\varphi^2}, \tag{2.17}$$

and $v(v+1)$ is the separation constant. It is obvious that (2.15) represents the differential equation of the spherical Bessel functions of the order $v(v+1)$ with a general solution defined as

$$z_v(\kappa r) = \sqrt{\frac{\pi}{2\kappa r}} Z_{v+1/2}(\kappa r). \tag{2.18}$$

We will be later interested only in the following special case of (2.18)

$$h_v^{(1,2)}(\kappa r) = \sqrt{\frac{\pi}{2\kappa r}} H_{v+1/2}^{(1,2)}(\kappa r) \qquad \text{spherical Hankel functions of } 1^{st} \text{ and } 2^{nd} \text{ kinds.} \tag{2.19a}$$

The solution of the transversal equation (2.16) takes the form

$$Y_{n,m}(\vartheta,\varphi) = \sqrt{\frac{2n+1}{4\pi}\frac{(n-m)!}{(n+m)!}} P_n^m(\cos\vartheta) e^{jm\varphi}, \tag{2.20}$$

where $Y_{n,m}$ is the normalized form of the spherical harmonic functions and P_n^m represents the associated Legendre polynomials [26] with a general form defined as

$$P_n^m(x) = (-1)^m \frac{(1-x^2)^{(m/2)}}{2^n n!} \frac{d^{n+m}(x^2-1)^n}{dx^{n+m}}. \tag{2.21}$$

While the order n of the spherical harmonics can include all integer positive values of $0 < n < \infty$, the degree m can only take the integer values $-n \le m \le +n$. The spherical harmonic function represents a complete set of orthogonal functions on the entire spherical surface as

$$\int_0^{\pi}\int_0^{2\pi} Y_{n,m} Y^*_{n',m'} \sin\vartheta d\vartheta d\varphi = \delta_{n,n'}\delta_{m,m'}, \tag{2.22}$$

where δ is the Kronecker delta symbol

$$\delta_{i,j} = \begin{cases} 1 & i = j \\ 0 & i \neq j. \end{cases}$$

A particular solution of the scalar Helmholtz equation (2.14) in spherical coordinates can be given by

$$\Psi_{n,m}(r,\vartheta,\varphi) = z_n(r) Y_{n,m}(\vartheta,\varphi) \qquad n \ge 0,\ -n \le m \le +n. \tag{2.23}$$

2.2.1 Bounded Integrals of the Spherical Bessel Functions

Assume $R_n(\alpha r)$ and $Q_n(\beta r)$ are two arbitrary solutions of (2.15), where α and β are complex numbers [29]- [30]. Equation (2.15) can be recast as

$$\frac{d}{dr}\left(r^2 \frac{d}{dr} R_n(\alpha r)\right) + \left((\alpha r)^2 - n(n+1)^2\right) R_n(\alpha r) = 0 \tag{2.24a}$$

$$\frac{d}{dr}\left(r^2 \frac{d}{dr} Q_n(\beta r)\right) + \left((\beta r)^2 - n(n+1)^2\right) Q_n(\beta r) = 0. \tag{2.24b}$$

We multiply (2.24a) by Q_n and (2.24b) by R_n and then subtract (2.24a) from (2.24b) and we obtain

$$\frac{d}{dr}\left(r^2\left[R_n(\alpha r)\frac{dQ_n(\beta r)}{dr} - Q_n(\beta r)\frac{dR_n(\alpha r)}{dr}\right]\right) = r^2(\beta^2-\alpha^2)R_n(\alpha r)Q_n(\beta r). \tag{2.25}$$

By integrating both sides of (2.25), we get

$$\int_r R_n(\alpha r)Q_n(\beta r)r^2dr = \frac{r^2}{\beta^2-\alpha^2}\left[R_n(\alpha r)\frac{dQ_n(\beta r)}{dr} - Q_n(\beta r)\frac{dR_n(\alpha r)}{dr}\right]. \tag{2.26}$$

The integral (2.26) is known as Lummel's integral formula [29]. So long as $R_n(\alpha r)$ and $Q_n(\beta r)$ are solutions for the spherical Bessel equation, they follow the same properties of the spherical Bessel functions. Consequently, the conjugation of a Bessel function results in the conjugation of its argument. By setting $Q_n = R_n^*$, $\alpha = \alpha^*$ and using the following recurrence relation

$$\frac{dR_n(\alpha r)}{dr} = \frac{n}{r}R_n(\alpha r) - \alpha R_{n+1}(\alpha r)$$

, and after some mathematical operations, (2.26) can be rewritten as

$$\begin{aligned}\int_r R_n(\alpha r)R_n^*(\alpha r)r^2dr &= \int_r \left|R_n(\alpha r)\right|^2 r^2dr \\ &= \frac{r^2}{\alpha^2-\alpha^{*2}}\left[\alpha R_{n+1}(\alpha r)R_n^*(\alpha r) - \alpha^* R_{n+1}^*(\alpha r)R_n(\alpha r)\right].\end{aligned} \tag{2.27}$$

Equation (2.27) is utilized if α is complex, i.e., in a medium with a frequency-dependent permittivity or permeability. In case of a lossless medium, $\alpha^* \longrightarrow \alpha$ and equation (2.27) must be recast using l'Hôpital's rule as

$$\begin{aligned}&\int_r \left|R_n(\alpha r)\right|^2 r^2dr \\ &\qquad = \frac{r^2}{2\alpha}\left[\alpha r R_{n+1}(\alpha r)\frac{R_n^*(\alpha r)}{d(\alpha r)} - \alpha r R_n(\alpha r)\frac{R_{n+1}^*(\alpha r)}{d(\alpha r)} - R_{n+1}^*(\alpha r)R_n(\alpha r)\right].\end{aligned} \tag{2.28}$$

2.2.2 Definition of the Multipole Functions $\vec{\mathbf{M}}_{\mathbf{n,m}}$ and $\vec{\mathbf{N}}_{\mathbf{n,m}}$

Substitution of the final solution of the scalar Helmholtz equation (2.23) into (2.13), the spherical multipole function $\vec{M}_{n,m}$ is defined as

$$\begin{aligned}\vec{M}_{n,m}(\vec{r}) &= (\vec{r}\times\vec{\nabla})z_n(\kappa r)Y_{n,m}(\vartheta,\varphi) \\ &= z_n(\kappa r)\vec{m}_{n,m}(\vartheta,\varphi),\end{aligned} \tag{2.29}$$

while the function $\vec{N}_{n,m}$ is

$$\begin{aligned}\vec{N}_{n,m}(\vec{r}) &= \frac{1}{\kappa}\vec{\nabla}\times\left((\vec{r}\times\vec{\nabla})z_n(\kappa r)Y_{n,m}(\vartheta,\varphi)\right) \\ &= -\frac{z_n(\kappa r)}{\kappa r}n(n+1)Y_{n,m}(\vartheta,\varphi)\hat{r} - \frac{1}{\kappa r}\frac{d}{dr}(rz_n(\kappa r))\vec{n}_{n,m}(\vartheta,\varphi).\end{aligned} \tag{2.30}$$

The transversal functions $\vec{m}_{n,m}$ and $\vec{n}_{n,m}$ of the multipole functions are defined in

$$\vec{m}_{n,m}(\vartheta,\varphi) = -\frac{1}{\sin\vartheta}\frac{\partial Y_{n,m}(\vartheta,\varphi)}{\partial\varphi}\hat{\vartheta} + \frac{\partial Y_{n,m}(\vartheta,\varphi)}{\partial\vartheta}\hat{\varphi} \tag{2.31a}$$

$$\vec{n}_{n,m}(\vartheta,\varphi) = \quad \frac{\partial Y_{n,m}(\vartheta,\vartheta)}{\partial\vartheta}\hat{\vartheta} + \frac{1}{\sin\vartheta}\frac{\partial Y_{n,m}(\vartheta,\varphi)}{\partial\varphi}\hat{\varphi}, \tag{2.31b}$$

respectively. We observe that the functions $\vec{m}_{n,m}$ and $\vec{n}_{n,m}$ depend on the spherical harmonic function $Y_{n,m}$ and thus represent a complete set of orthogonal functions on the entire spherical surface $0 \leq \vartheta \leq \pi$ and $0 \leq \varphi \leq 2\pi$ according to

$$\int_0^{\pi}\int_0^{2\pi} \vec{m}_{n,m}(\vartheta,\varphi)\cdot\vec{m}^*_{n',m'}(\vartheta,\varphi)\sin\vartheta d\vartheta d\varphi = n(n+1)\delta_{nn'}\delta_{mm'} \tag{2.32a}$$

$$\int_0^{\pi}\int_0^{2\pi} \vec{n}_{n,m}(\vartheta,\varphi)\cdot\vec{n}^*_{n',m'}(\vartheta,\varphi)\sin\vartheta d\vartheta d\phi = n(n+1)\delta_{nn'}\delta_{mm'} \tag{2.32b}$$

$$\int_0^{\pi}\int_0^{2\pi} \vec{m}_{n,m}(\vartheta,\varphi)\cdot\vec{n}^*_{n',m'}(\vartheta,\varphi)\sin\vartheta d\vartheta d\varphi = 0. \tag{2.32c}$$

Equations (2.32) represent the orthogonality relations of the spherical Bessel functions [28]. A corollary for the multipole functions is that they can be coupled together through the following relations

$$\vec{\nabla}\times\vec{M}_{n,m}(\vartheta,\varphi) = \kappa\vec{N} \tag{2.33a}$$

$$\vec{\nabla}\times\vec{N}_{n,m}(\vartheta,\varphi) = \kappa\vec{M}. \tag{2.33b}$$

2.3 Frequency Dispersion Properties in Dielectric Materials

Conductors and insulators (dielectrics) are two main classes of materials. Unlike dielectrics, where the charges are bound to the atoms, the conductors' charges (electrons) are free-moving. In reality, there is no ideal lossless material where the propagating electromagnetic waves experience distortion due to the interception of the bound charges (dielectric loss) or the moving charges (conductive loss) [31, 32]. Therefore, the propagation velocity can not be treated as constant over the entire frequency spectrum, except in certain cases, it can be considered constant only over a limited frequency range or in a vacuum. We are interested in interpreting the permittivity and permeability dispersion in any material. If an electric field is applied to an isotropic and homogeneous dielectric material, most bound and free-moving charges are rearranged in the same direction as the applied field. The equation of motion for an electron of a charge $-q$ under the effect of the externally applied electric field $\vec{E}(\vec{r},t)$ according to ([26], Ch. 7) is given by

$$m\frac{\partial^2\vec{r}}{\partial t^2} + m\Gamma_o\frac{\partial\vec{r}}{\partial t} + m\omega_o^2\vec{r} = -q\vec{E}(\vec{r},t), \tag{2.34}$$

where ω_0 is the resonant frequency and m is the electron mass, while Γ_o is the damping force. Using the Fourier transforms, (2.34) can be rewritten in the frequency-domain as

$$\vec{r}(\omega) = \frac{-q}{m}\frac{E(\omega)}{\omega_0^2 - \omega^2 + j\omega\Gamma_o}. \tag{2.35}$$

The induced dipole moment due to the applied electric field to the dielectric material is given by

$$\vec{p} = -q\vec{r} = \zeta\vec{E}, \tag{2.36}$$

where ζ is the polarizability of every single atom. If we assume that there are N molecules per unit volume in the dielectric material, then the total polarization can be written using (2.36) as

$$\vec{P} = -Nq\vec{r} = N\zeta\vec{E}. \tag{2.37}$$

By substituting of (2.35) into (2.37) and using (2.5a) with the constitutive relation $\varepsilon_r(\omega) = 1 + \chi_e(\omega)$, the relative permittivity can be given by

$$\varepsilon_r(\omega) = 1 + \frac{Nq^2}{m\varepsilon_o}\frac{1}{\omega_0^2 - \omega^2 + j\omega\Gamma_o}. \tag{2.38}$$

The second part of the right side of (2.38) indicates the dielectric susceptibility χ_e. It is evident from (2.38) that the permittivity is a complex-valued quantity and a function of the angular frequency ω. This equation clearly describes the frequency dispersion in the relative permittivity of any dielectric material.

2.4 The Causality Principle and the Kramers-Kronig Relations

In practice, all dielectric and magnetic material show dispersion in permittivity, permeability, and conductivity over the entire frequency spectrum. This is well-known as the dispersion phenomenon [33–36]. This phenomenon occurs in any medium exposed to an external effect, such as electromagnetic fields. Subsequently, the concept of the dispersion phenomenon is closely related to the causality principle. The latter means that the effect can never precede the cause. However, an essential consequence of causality is that the Fourier transform of any causal function shows an analytical continuation of the transformed function into any portion of the complex frequency plane [37]. In other words, the Fourier transformed function can be expanded to a complex function with its real and imaginary parts eventually represented in integral relations known as the dispersion or the Kramers-Kronig relations. These integral relations were firstly derived by Kramers [38], and Kronig [39]. Kramers showed that an optical system's real part of the refractive index (closely related to the real part of the complex permittivity and permeability) could be calculated from the absorbed light, i.e., from the imaginary part of the complex permittivity. Kronig demonstrated that the dispersion in a medium is a direct consequence of the causality principle. The Kramers-Kronig (will be denoted as KK) relations generally relate the real and the imaginary parts of any complex quantity describing a causal system. Therefore, the real part can be uniquely calculated from the imaginary part over either a limited or whole spectrum range and vice versa. In the following section, it will be shown that the transformations mentioned above are applicable to the dielectric and the magnetic material provided that the causality condition is present.

2.4.1 Causality and Analyticity of $\chi_e(\omega)$ and $\chi_m(\omega)$

The electromagnetic fields $\vec{D}, \vec{E}$ and $\vec{B}, \vec{H}$ in (2.4) can be connected to each other in the time domain by the following convolution integrals ([26] Ch. 7)

$$\vec{D}(\vec{r},t) = \varepsilon_0\vec{E}(\vec{r},t) + \int_{-\infty}^{\infty} \varepsilon_0\chi_e(\tau)\vec{E}(\vec{r},t-\tau)d\tau \tag{2.39a}$$

$$\vec{B}(\vec{r},t) = \mu_0\vec{H}(\vec{r},t) + \int_{-\infty}^{\infty} \mu_0\chi_m(\tau)\vec{H}(\vec{r},t-\tau)d\tau \tag{2.39b}$$

. Where χ_e and χ_m are the time-varying electric and magnetic susceptibilities, respectively. It can be noticed in (2.39) that the fields are non-locally interrelated in the time-domain, i.e. in (2.39a), the electric displacement $\vec{D}$ at time t relies on the electric field $\vec{E}$ at times before t as well. Consequently, only the electric field intensity at times prior to that time t contributes to determining the electric displacement, which gives the same definition of the causality principle. Equations (2.39a) and (2.39b) are equivalent and describe the causality principle in the dielectric and magnetic materials, respectively. Next, we study the case of the dispersion in the dielectric materials, and the same procedure is applicable for the magnetic materials.

By assuming no electric field is present at times $t < 0$, the temporal relation between $\vec{D}$ and $\vec{E}$ is causal, and (2.39a) is recast as

$$\vec{D}(\vec{r},t) = \varepsilon_0\vec{E}(\vec{r},t) + \int_{0}^{\infty} \varepsilon_0\chi_e(\tau)\vec{E}(\vec{r},t-\tau)d\tau. \tag{2.40}$$

It is obvious in (2.40) that $\chi_e(\tau)$ is defined only on the positive time-domain, i.e. $\chi_e(\tau) = 0$ for $\tau < 0$. The part $\chi_e(\tau)$ is the inverse Fourier transform of $\chi_e(\omega)$, which is defined by

$$\chi_e(\omega) = \int_{0}^{\infty} \chi_e(\tau)e^{-j\omega\tau}d\tau. \tag{2.41}$$

$$\chi_e(\omega) = \chi_e'(\omega) - j\chi_e''(\omega). \tag{2.42}$$

However, in reality, the susceptibility function $\chi_e(\tau)$ is purely real in time-domain. Thus, it has even and odd symmetries for its real and imaginary components, respectively, in the frequency-domain [26]

$$\chi_e'(-\omega) = \chi_e'(\omega) \qquad \text{even symmetry} \tag{2.43a}$$

$$\chi_e''(-\omega) = -\chi_e''(\omega) \qquad \text{odd symmetry.} \tag{2.43b}$$

From the derivations mentioned above, it has been shown that the causal property of any function in the time-domain leads to analytical properties of this function in the frequency-domain, i.e., the function encompasses real and imaginary parts represented as a complex function.

Since the electric and magnetic fields depend on each other, as in (2.3), the magnetic field, like the electric field, follows the principle of causality. Consequently, the magnetic susceptibility $\chi_m(\omega)$ will have the same analytical properties as $\chi_e(\omega)$ and can be represented in the complex frequency-domain as

$$\chi_m(\omega) = \chi_m'(\omega) - j\chi_m''(\omega). \tag{2.44}$$

The real and imaginary parts of (2.42) and (2.44) are not independent and connected through the KK integral relations, which will be shown in the following section, provided that the causality and the analyticity of the function hold.

2.5 Kramers-Kronig Relations for $\chi_e(\omega)$ and $\chi_m(\omega)$

There is a close relationship between the analyticity of the complex-valued functions and Cauchy's integral theorem [40]. This theorem can interrelate the real and imaginary parts of the functions $\chi_e(\omega)$ and $\chi_m(\omega)$ if they have an analytical continuation in the upper half-plane of the complex frequency. The Kramers-Kronig relations are derived using this argument of Cauchy's integrals for the complex-valued functions [40]. The derivation is discussed in detail in the Appendix A. Therefore, the integrals of the real and the imaginary parts in (A.9), (A.13) can be directly applied to calculate the electric and magnetic susceptibilities. By expanding these integrals over the whole real frequency axis of ω, the integral equations for $X'_e(\omega)$ and $X''_e(\omega)$ in any dispersive dielectric material can be given by

$$\chi'_e(\omega) = \frac{2}{\pi}\int_0^\infty \frac{\psi\chi''_e(\psi) - \omega\chi''_e(\omega)}{\psi^2-\omega^2}d\psi \tag{2.45a}$$

$$\chi''_e(\omega) = \frac{-2\omega}{\pi}\int_0^\infty \frac{\chi'_e(\psi) - \chi'_e(\omega)}{\psi^2-\omega^2}d\psi, \tag{2.45b}$$

where ψ is the angular integration frequency. By substituting (2.45) into (2.7), expressions for real and imaginary parts of the relative permittivity can be obtained as

$$\varepsilon'(\omega) = 1 + \frac{2}{\pi}\int_0^\infty \frac{\psi\varepsilon''(\psi) - \omega\varepsilon''(\omega)}{\psi^2-\omega^2}d\psi \tag{2.46a}$$

$$\varepsilon''(\omega) = \frac{-2\omega}{\pi}\int_0^\infty \frac{\varepsilon'(\psi) - \varepsilon'(\omega)}{\psi^2-\omega^2}d\psi. \tag{2.46b}$$

The analyticity and linearity of the integrations (2.46) lead to an analytical continuation of the relative permittivity in the lower half-plane of the complex frequency; thus, its real and imaginary parts are connected by the Kramers-Kronig relations. These relations are also known in the literature as the dispersion relations or the Hilbert transforms [40].

Likewise, the dispersion in the magnetic material can be interpreted by the Kramers-Kronig relations provided that the causal connection between the magnetization $\vec{M}$ and the applied magnetic field $\vec{H}$ in the time-domain is satisfied. The real and the imaginary parts of the complex dispersive permeability are related to each other by

$$\mu'(\omega) = 1 + \frac{2}{\pi}\int_0^\infty \frac{\psi\mu''(\psi) - \omega\mu''(\omega)}{\psi^2-\omega^2}d\psi \tag{2.47a}$$

$$\mu''(\omega) = \frac{-2\omega}{\pi}\int_0^\infty \frac{\mu'(\psi) - \mu'(\omega)}{\psi^2-\omega^2}d\psi. \tag{2.47b}$$

It is evident in (2.46) and (2.47) that the values of either the real or the imaginary part can be obtained by solving the integrals over the whole frequency spectrum [0, ∞]. However, in reality, no experimental method can measure any material's permittivity, permeability, and conductivity over the whole frequency spectrum. Therefore, in the following sections, some constraints for the Kramers-Kronig relations will be discussed to validate their solutions over a limited frequency range.

2.6 Constraints of the Kramers-Kronig Relations

Although the Kramers-Kronig relations can interrelate the real and the imaginary parts of any frequency-dependent complex function, some constraints are indirectly mentioned in the former sections to validate them:

1. The causality connection between any external effect and the response of the system must be present [33]. For instance, the polarization $\vec{P}$ in dielectric materials due to the microscopically bounded charges can not exist without an externally applied electric field $\vec{E}$.

2. The relation between the external effect (electric or magnetic field) and the response of the system (polarization or magnetization) must be linear and stable, i.e., the system response must decay as the time increases after removing the effect [41].

3. The desired function (relative permittivity or permeability) must vanish at infinite frequencies $\omega \rightarrow \infty$ [40]. For instance, consider the function $\varepsilon_r(\omega) = A - jB$ where A and B (closely related to ε' and ε'') are constants, then $\lim_{\omega\rightarrow\infty} \varepsilon_r(\omega) \neq 0$. Consequently, ε' and ε'' are completely unrelated.

These constraints are consistent and indissociable, i.e., if one constraint is not satisfied, the validation of the Kramers-Kronig relations will be violated [41]. Subsequently, any system that satisfies the above-mentioned constraints must satisfy the Kramers-Kronig relations. From this point, the KK relations are purely a mathematical problem, and its integrations are solvable provided that the range of frequencies over which the function is measured is wide enough that the integrals of (2.46) can be calculated.

2.7 Kramers-Kronig Integrals Solution Over a Limited Frequency Range

Usually, the Kramers-Kronig integrals should be evaluated over a semi-infinite frequency range ($0 \leq \omega \leq \infty$). In contrast, the given data (always refers to the measured data) of the real and the imaginary parts of the complex-valued function is taken only over a limited frequency range. Consequently, unavoidable integration errors arise while solving the integrals (2.46) and (2.47) over the limited range of frequencies. For instance, if $\varepsilon''(\omega)$ in (2.46a) is given over a definite frequency interval $[\omega_1, \omega_2]$, a mismatch between $\varepsilon'(\omega)$, calculated from the integral (2.46a), and its corresponding $\varepsilon'(\omega)$ of the original or given data will arise. In such a case, it can be interpreted that either the original data of $\varepsilon''(\omega)$ and $\varepsilon'(\omega)$ are unrelated to each another, or one of them violates the constraints of the KK relations mentioned in the former section. For solving such a problem, some methods were introduced in [33], [42], [43] to solve the KK integrations over a narrow band of frequencies.

The optimal solution to this problem is that the frequency range over which the obtained data is given must be selected sufficiently wide to be close to the lower and the upper-frequency bounds of the KK integrations $\omega = 0$ and $\omega = \infty$, respectively. For instance, the experimental method must be performed on a semi-infinite range of frequencies ($0 \leq \omega \leq \infty$). However, no experimental method can cover such a wide range of frequencies. Consequently, we

mathematically investigate this problem of solving the KK integrations over a limited frequency range. Firstly, we begin by solving (2.46b) at a single frequency $\omega = \omega_k$. The integral formula (2.46b) can be broken up into three integrals as

$$\varepsilon''(\omega_k) = \frac{-2\omega_k}{\pi}\Bigg\{ \int_0^{\psi_{\min}} \frac{\varepsilon'(\psi) - \varepsilon'(\omega_k)}{\psi^2 - \omega_k^2} d\psi + \int_{\psi_{\min}}^{\psi_{\max}} \frac{\varepsilon'(\psi) - \varepsilon'(\omega_k)}{\psi^2 - \omega_k^2} d\psi + \int_{\psi_{\max}}^{\infty} \frac{\varepsilon'(\psi) - \varepsilon'(\omega_k)}{\psi^2 - \omega_k^2} d\psi \Bigg\}. \tag{2.48}$$

To solve the integrals of (2.48), the function $\varepsilon'(\psi)$ should have a mathematical form in addition to the location of the pole ω_k must be known. If the pole is chosen positive and much smaller than the upper bound of the first integral $\omega_k \ll \psi_{\min}$, then ω_k^2 can be neglected in comparison with $\psi_{\max}^2$ in the denominator of the third integral. Therefore, (2.48) is rewritten as

$$\varepsilon''(\omega_k) \simeq \frac{-2\omega_k}{\pi}\Bigg\{ \int_0^{\psi_{\min}} \frac{\varepsilon'(\psi) - \varepsilon'(\omega_k)}{\psi^2 - \omega_k^2} d\psi + \int_{\psi_{\min}}^{\psi_{\max}} \frac{\varepsilon'(\psi) - \varepsilon'(\omega_k)}{\psi^2 - \omega_k^2} d\psi + \int_{\psi_{\max}}^{\infty} \big\{\varepsilon'(\psi) - \varepsilon'(\omega_k)\big\} \frac{d\psi}{\psi^2} \Bigg\}. \tag{2.49}$$

If the function $\varepsilon'(\psi)$ is considered nearly constant over the frequency interval $[\psi_{\max}, \infty]$ and very close to $\varepsilon'(\omega_k)$, then the contribution of the third integral in (2.49) is finite and can be neglected.

Now suppose ω_k is chosen very large, where $\omega_k \gg \psi_{\max}$, then (2.48) is recast as

$$\varepsilon''(\omega_k) \simeq \frac{-2\omega_k}{\pi}\Bigg\{ \int_0^{\psi_{\min}} \big\{\varepsilon'(\omega_k) - \varepsilon'(\psi)\big\} \frac{d\psi}{\omega_k^2} + \int_{\psi_{\min}}^{\psi_{\max}} \frac{\varepsilon'(\psi) - \varepsilon'(\omega_k)}{\psi^2 - \omega_k^2} d\psi + \int_{\psi_{\max}}^{\infty} \frac{\varepsilon'(\psi) - \varepsilon'(\omega_k)}{\psi^2 - \omega_k^2} d\psi \Bigg\}, \tag{2.50}$$

where in this case, ψ^2 is neglected in comparison with ω_k^2 in the denominator of the first integral. If the frequency ω_k is taken where $\psi_{\min} \leq \omega_k \leq \psi_{\max}$, then the contribution of ω can not be neglected from the second integral.

When solving (2.48) for a given $\varepsilon'(\psi)$, unavoidable integration errors will arise due to the contribution of the first and third integrals if they are entirely ignored. To avoid such errors, the bounds of the second integral are chosen sufficiently large and the values of $\varepsilon'(\psi)$ are supposed to be slightly changeable as a function of the frequency over the low and high frequencies, i.e., $\varepsilon'(\psi) \simeq \varepsilon'(\psi_{\min})$ over the frequency interval $[0, \psi_{\min}]$ and $\varepsilon'(\psi) \simeq \varepsilon'(\psi_{\max})$ over the frequency interval $[\psi_{\max}, \infty]$. We omit k from ω_k and rewrite (2.48) using (2.49) and (2.50) for any frequency ω as

$$\varepsilon''(\omega) \simeq \frac{-2\omega}{\pi}\Bigg\{ \big(\varepsilon'(\omega) - \varepsilon'(\psi_{\min})\big) \int_0^{\psi_{\min}} \frac{d\psi}{\omega^2} + \int_{\psi_{\min}}^{\psi_{\max}} \frac{\varepsilon'(\psi) - \varepsilon'(\omega)}{\psi^2 - \omega^2} d\psi + \big(\varepsilon'(\psi_{\max}) - \varepsilon'(\omega)\big) \int_{\psi_{\max}}^{\infty} \frac{d\psi}{\psi^2} \Bigg\}, \tag{2.51}$$

where $\varepsilon'(\psi_{\min})$ and $\varepsilon'(\psi_{\max})$ are assumed constant and do not contribute to the integration parts of (2.51).

Usually, $\varepsilon'(\omega)$ refers to the original (measured) data and is given on a limited frequency range, while $\varepsilon'(\psi)$ is an extrapolated function as will be discussed later. Therefore, we assume that $\varepsilon'(\omega)$ in (2.51) is limited on a frequency interval $[\omega_1, \omega_2]$. After that, choose ω_1 to be much larger than the lower bound of the integration frequency as $\omega_1 \gg \psi_{\min}$, i.e., $\psi_{min} : \omega_1$ is smaller than $1 : 100$. For instance, we take $\omega_1 = 10^8$ s^{-1}, whereas $\psi_{\min} = 10^6$ s^{-1}, then the first integral in (2.51) is evaluated as

$$\frac{-2\omega}{\pi}\int_0^{\psi_{\min}} \big(\varepsilon'(\omega) - \varepsilon'(\psi_{\min})\big)\frac{d\psi}{\omega^2} \simeq 6.4\text{x}10^{-3}\big\{\varepsilon'(\psi_{\min}) - \varepsilon'(\omega)\big\}. \tag{2.52}$$

Now chose the frequency ω_2 to be much smaller than the upper bound of the integration frequency as $\omega_2 \ll \psi_{\max}$, i.e., $\psi_{\max} : \omega_2$ is larger than $1000 : 1$. Assuming $\omega_2 = 10^{10}$ s^{-1} whereas $\psi_{\max} = 10^{13}$ s^{-1}, the third integral in (2.51) is evaluated as

$$\frac{-2\omega}{\pi}\int_{\psi_{\max}}^{\infty} \big(\varepsilon'(\psi_{\max}) - \varepsilon'(\omega)\big)\frac{d\psi}{\psi^2} \simeq 6.4\text{x}10^{-4}\big\{\varepsilon'(\omega) - \varepsilon'(\psi_{\max})\big\}. \tag{2.53}$$

Substituting of (2.52) and (2.53) into (2.51), the imaginary part of the relative permittivity $\varepsilon''(\omega)$ is written in the form of

$$\varepsilon''(\omega) \simeq \frac{-2\omega}{\pi}\int_{\psi_{\min}}^{\psi_{\max}} \frac{\varepsilon'(\psi) - \varepsilon'(\omega)}{\psi^2 - \omega^2}d\psi + e_1\big\{\varepsilon'(\psi_{\min}), \varepsilon'(\psi_{\max}), \varepsilon'(\omega)\big\}, \tag{2.54}$$

where e_1 represents the contribution of the first and the third integrals and is evaluated from (2.52) and (2.53) as

$$e_1\big\{\varepsilon'(\psi_{\min}), \varepsilon'(\psi_{\max}), \varepsilon'(\omega)\big\} = 6.4\text{x}10^{-3}\big\{\varepsilon'(\psi_{\min}) - \varepsilon'(\omega)\big\} + 6.4\text{x}10^{-4}\big\{\varepsilon'(\omega) - \varepsilon'(\psi_{\max})\big\}. \tag{2.55}$$

Following the same procedure, the real part of the relative permittivity $\varepsilon'(\omega)$ can be evaluated in terms of the imaginary part $\varepsilon''(\omega)$ using (2.46a) as

$$\varepsilon'(\omega) \simeq 1 + \frac{2}{\pi}\int_{\psi_{\min}}^{\psi_{\max}} \frac{\psi\varepsilon''(\psi) - \omega\varepsilon''(\omega)}{\psi^2 - \omega^2}d\psi + e_2\big\{\varepsilon''(\psi_{\min}), \varepsilon''(\psi_{\max})\big\}, \tag{2.56}$$

where e_2 is evaluated as

$$e_2\big\{\varepsilon''(\psi_{\min}), \varepsilon''(\psi_{\max}), \varepsilon''(\omega)\big\} = 3.2\text{x}10^{-5}\big\{\varepsilon''(\psi_{\max}) - \varepsilon''(\omega)\big\}. \tag{2.57}$$

It is obvious from (2.55) and (2.57) that e_1 and e_2 depend on $\psi_{\min}$ and $\psi_{\max}$. By selecting $\varepsilon'(\psi_{\min})$ and $\varepsilon'(\psi_{\max})$ to be slightly changeable over the low and high frequencies and close to $\varepsilon'(\omega)$ and $\varepsilon''(\omega)$, respectively, i.e., $\varepsilon'(\psi_{\min}) \simeq \varepsilon'(\omega)$, whereas $\varepsilon'(\psi_{\max}) \simeq \varepsilon'(\omega)$, then the contribution of e_1 can be sufficiently minimized in (2.54). Likewise for e_2, its contribution can be sufficiently reduced in (2.56).

2.7.1 Numerical Calculation of the Kramers-Kronig Integrals

Practically, the functions $\varepsilon'(\omega)$ and $\varepsilon''(\omega)$ are experimentally obtained data and do not have a specific mathematical expression to be integrable. Consequently, the integrals in (2.54) and (2.56) can only be evaluated when the functions $\varepsilon'(\psi)$ and $\varepsilon''(\psi)$ are interpolated from the precalculated values of $\varepsilon'(\omega)$ and $\varepsilon''(\omega)$ using high-order polynomials to avoid the errors resulting from the data fitting [44]. However, high-order polynomials are very sensitive to a data error, especially over the curve margins of the given function, because they generate predictions that diverge significantly from the true value. In other words, if the given function like $\varepsilon'(\omega)$ or $\varepsilon''(\omega)$ is highly dispersive, the high-order interpolating polynomials are not the best choice to fit the original data. Accordingly, we suggest the spline interpolation method, where the whole range of the given values is subdivided into n-subsets, and each subset is interpolated using a low-order polynomial [45]. In (2.54), the values of $\varepsilon'(\psi)$ in the numerator are subdivided into n-subsets as follows:

$$\varepsilon'_n(\psi) = q_n(\psi) = \begin{cases} \sum_{m=0}^{M} a_m \psi^m & \text{for} \quad \psi_{\text{n-1}} \leq \psi \leq \psi_{\text{n}} \\ 0 & \text{elsewhere,} \end{cases} \tag{2.58}$$

where $q(\psi)$ is an M-order polynomial representing the function $\varepsilon'_n(\psi)$ and n refers to the number of the spline polynomials. By substituting (2.58) into (2.54), a final expression for the KK integration can be given by

$$\varepsilon''(\omega) \simeq \frac{-2\omega}{\pi} \sum_{n=1}^{N} \int_{\psi_{n-1}}^{\psi_n} \frac{q_n(\psi) - \varepsilon'(\omega)}{\psi^2 - \omega^2} d\psi + e_1\big\{\varepsilon'(\psi_{\min}), \varepsilon'(\psi_{\max}), \varepsilon'(\omega)\big\}. \tag{2.59}$$

It is preferred to interpolate $\varepsilon'_n(\psi)$ in lower-order polynomials to avoid the error between the interpolants [46].

To demonstrate the validity of the above-mentioned analytical method, we assume some artificial values for the real part of the relative permittivity (referred to as original values in Fig. 2.1a) over a frequency range $1 - 20$ GHz. From the original values of the real part, the imaginary part $\varepsilon''(\omega)$ (referred to as KK transformed in Fig. 2.1b) is evaluated using (2.59) at $\psi_{\min} = 6.2\text{x}10^8$ s^{-1} and $\psi_{\max} = 2.9\text{x}10^{11}$ s^{-1}. To make sure of the interrelation between the values of the real and imaginary parts of $\varepsilon(\omega)$, the KK-transformed values in Fig. 2.1b are utilized to recalculate the real part (referred to as double Kramers-Kroning (DKK) in Fig. 2.1a) at two different values of $\psi_{\min}$ and $\psi_{\max}$.

It is evident from Fig. 2.1, that the interrelation between the real and the imaginary parts of the frequency-dependent relative permittivity can be verified using the Kramers-Kronig relations, provided that one of them is known over a finite range of frequencies and satisfies the constraints of the KK relations.

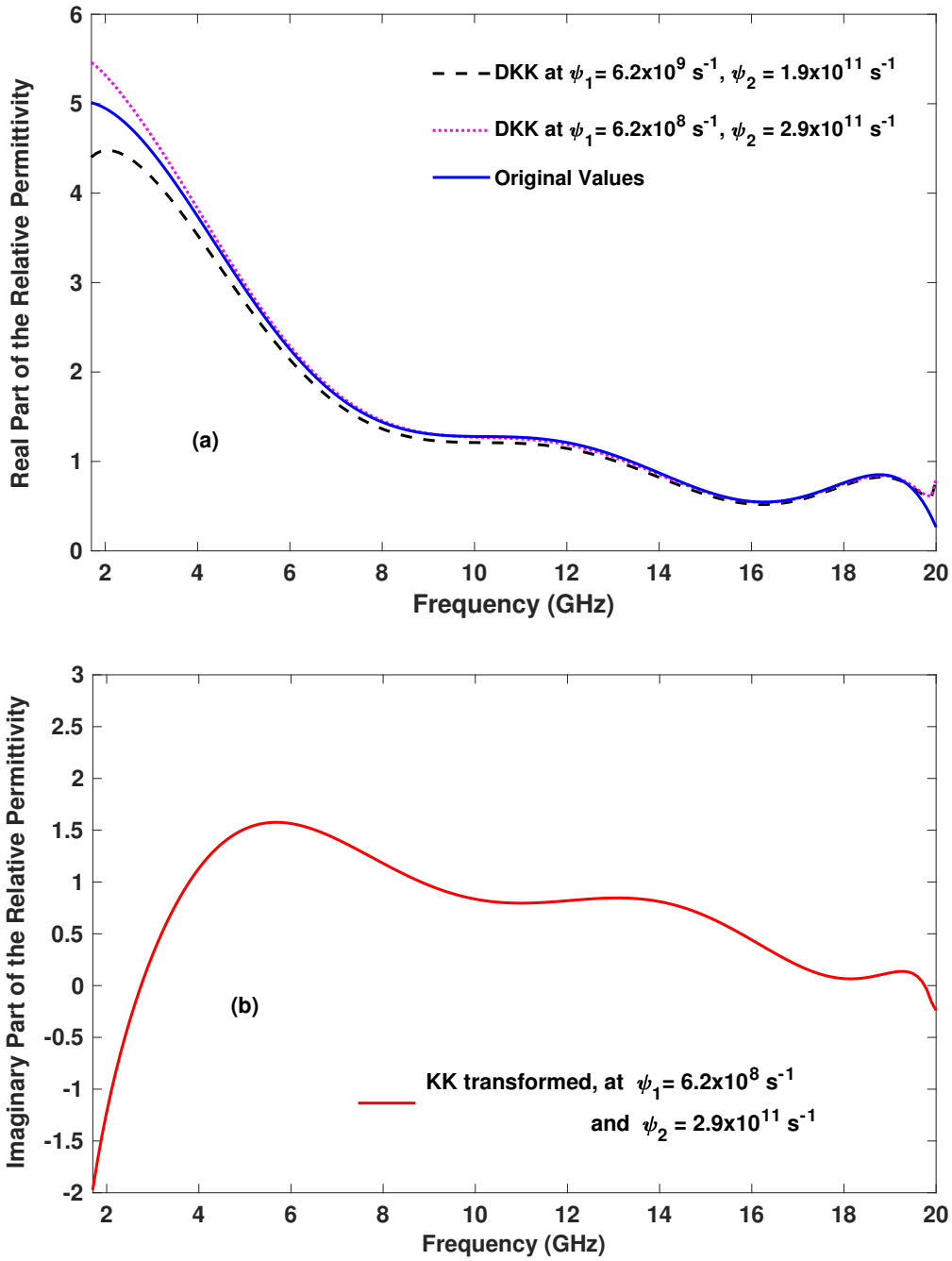

Figure 2.1: (**a**) The real part and (**b**) the imaginary parts of an artificially synthesized data set for the relative permittivity. From the original values of the synthetic real part (blue solid curve in (**a**)), the imaginary part (referred to as KK transformed in (**b**)) is evaluated by (2.54). From the red curve in (**b**), the real part (referred to as DKK in (**a**)) is recalculated (for self-consistency of the KK transforms) using (2.56) at different values of $\psi_{\min}$ and $\psi_{\max}$.

3. Conductivity Loss Separation Using the Kramers-Kronig Transformations

In this Chapter, the Kramers-Kronig transformations are applied to separate the conductive losses from the dielectric losses in highly dispersive lossy materials. In practice, when measuring the complex-valued relative permittivity of dielectric materials, particularly in highly dispersive lossy materials like composite materials, the measured values of the imaginary part may not purely indicate the dielectric losses [47] [48]. Usually, the imaginary part of the complex-valued relative permittivity and permeability in any material includes dielectric (bound charges) and conductive (free-moving charges) losses. Therefore, the conductive and dielectric losses are indistinguishable in measurements, which leads to unavoidable errors in the values of the real and the imaginary parts of the measured relative permittivity and permeability. Separating the conductive losses from the dielectric losses in dispersive lossy materials, where the relative permittivity and permeability are frequency-dependent functions, is a non-trivial task unless a suitable dispersion model for the dielectric or conductivity properties of the material is assumed. Consequently, we utilize the Kramers-Kronig relations for this purpose.

Firstly, we assume fictitious lossy dielectric materials with randomly selected values of the frequency-dependent relative permittivity and permeability. The conductive losses will be assumed to be included in the imaginary part of the complex-valued relative permittivity. After that, the Kramers-Kronig transformations are employed to calculate the conductive losses from the dielectric losses of the suggested data. The proposed method will be verified by applying it to some measured values of the relative permittivity of the composite materials.

3.1 Frequency Dispersion Model for the Conductivity

We have discussed the dispersion in the relative permittivity in Section 2.3. For high frequencies $\omega \to \infty$, the relative permittivity in (2.38) is $\varepsilon_r(\omega) = \varepsilon_\infty = 1$, while for low frequencies $\omega \to 0$, the relative permittivity could be rewritten as

$$\varepsilon_r(\omega) = \varepsilon_\infty + \frac{Nq^2}{m\varepsilon_o} \frac{1}{j\omega\left(\Gamma_o - j\omega\right)}. \tag{3.1}$$

From Maxwell-Ampere equation (2.3b) and (2.4c), we get

$$\vec{\nabla} \times \vec{H}(\vec{r},\omega) = j\omega \left(\varepsilon_r(\omega) + \frac{\sigma_e}{j\omega}\right) \vec{E}(\vec{r},\omega). \tag{3.2}$$

The term between the brackets in (3.2) indicates the effective relative permittivity $\varepsilon(\omega)$ as will be discussed later. Comparing the term in brackets in (3.2) with (3.1) we get an expression for the conductivity as

$$\sigma_e(\omega) = \frac{\sigma_0}{1 - j\omega\Gamma_o^{-1}}, \tag{3.3}$$

where $\sigma_0 = Nq^2/(m\varepsilon_o\Gamma_o)$ is the DC conductivity ([26], Section 7.5). It is evident from (3.3) that the electric conductivity is a complex-valued quantity and is a function of the frequency ω. At very low frequencies $\omega \to 0$, the real part of the conductivity in (3.3) approaches σ_0, whereas the imaginary part vanishes. For instance, the metal acts as a good conductor at very low frequencies, while as the frequency approaches infinity $\omega \to \infty$, both the real and imaginary parts of the conductivity vanish and the metal becomes transparent to the applied electromagnetic fields [26].

3.2 Conductivity and Effective Permittivity

In the absence of the impressed electric current $\vec{J}_e^{\,imp}$, equation (2.4c) can be rewritten in the time-domain by the convolution relation as

$$\vec{J}_e(\vec{r}, t) = \int_0^\infty \tilde{\sigma}_e(\tau)\vec{E}(\vec{r}, t - \tau)d\tau. \tag{3.4}$$

Likewise as in Section 2.4.1, the electric current density $\vec{J}_e$ and the electric field intensity $\vec{E}$ are non-locally interrelated in the time-domain. The electric conductivity $\sigma_e(\tau)$ is the inverse Fourier transform of $\sigma_e(\omega)$, which can be defined as

$$\sigma_e(\omega) = \int_0^\infty \tilde{\sigma}_e(\tau)e^{-j\omega\tau}d\tau. \tag{3.5}$$

It is evident that the Fourier transform of $\sigma_e(\omega)$ in (3.5) must be an analytic function of ω in the upper half plane of the complex frequency [45], [37]. Subsequently, $\sigma_e(\omega)$ can be expanded to a complex function [26] as

$$\sigma_e(\omega) = \sigma_e'(\omega) - j\sigma_e''(\omega). \tag{3.6}$$

However, only the free-moving charges cause the conductivity. Thus, in practice, the conductivity is usually treated as a real-valued quantity.

By substituting of (3.6) and (2.7a) into (2.3) we may get

$$\begin{aligned}\vec{\nabla} \times \vec{H}(\vec{r}, \omega) &= j\omega\varepsilon_0\varepsilon_r(\omega)\vec{E}(\vec{r}, \omega) + \sigma_e(\omega)\vec{E}(\vec{r}, \omega) \\ &= j\omega\varepsilon_0\varepsilon_{\text{eff}}(\omega)\vec{E}(\vec{r}, \omega),\end{aligned} \tag{3.7a}$$

where the effective relative permittivity ε_{eff} is introduced as

$$\begin{aligned}\varepsilon_{\text{eff}}(\omega) &= \varepsilon_r(\omega) - j\frac{\sigma_e(\omega)}{\omega\varepsilon_0} \\ &= \varepsilon'(\omega) - \frac{\sigma_e''(\omega)}{\omega\varepsilon_0} - j\left\{\varepsilon''(\omega) + \frac{\sigma_e'(\omega)}{\omega\varepsilon_0}\right\} \\ &= \varepsilon_{\text{eff}}'(\omega) - j\varepsilon_{\text{eff}}''(\omega).\end{aligned} \tag{3.8}$$

Equation (3.8) is a general form of the effective relative permittivity for lossy dielectric materials. By solving (3.8) for $\varepsilon'(\omega)$ and $\varepsilon''(\omega)$ we get

$$\varepsilon'(\omega) = \varepsilon'_{\text{eff}}(\omega) + \frac{\sigma''_e(\omega)}{\omega\varepsilon_0} \tag{3.9a}$$

$$\varepsilon''(\omega) = \varepsilon''_{\text{eff}}(\omega) - \frac{\sigma'_e(\omega)}{\omega\varepsilon_0}. \tag{3.9b}$$

For insulators and lossless materials, where no free-moving charges are present $\sigma_e = 0$, the real and the imaginary parts in (3.9) reduce to that of (2.8).

3.3 Kramers-Kronig Relations for the Effective Permittivity

One of the properties of any analytic function is that its summation, product, and subtraction are analytic as well [49]. Therefore, the effective permittivity in (3.8) has an analytical continuation in the upper half plane of the complex frequency due to the analytical continuation of both the relative permittivity and the electric conductivity. Additionally, the real and the imaginary parts of the effective permittivity have even and odd properties as

$$\varepsilon'_{\text{eff}}(-\omega) = \varepsilon'_{\text{eff}}(\omega) \tag{3.10a}$$

$$\varepsilon''_{\text{eff}}(-\omega) = -\varepsilon''_{\text{eff}}(\omega). \tag{3.10b}$$

These properties demonstrate that the real and the imaginary parts of the effective relative permittivity satisfy the KK relations in (2.46).

By substituting (3.9) into (2.46), the corresponding Kramers-Kronig integrals could be written for the effective permittivity in the form of

$$\varepsilon'_{\text{eff}}(\omega) + \frac{\sigma''_e(\omega)}{\omega\varepsilon_0} = 1 + \frac{2}{\pi}\int_0^\infty \frac{\psi\varepsilon''_{\text{eff}}(\psi) - \omega\varepsilon''_{\text{eff}}(\omega)}{\psi^2 - \omega^2}d\psi - \frac{2}{\pi\varepsilon_0}\int_0^\infty \frac{\sigma'_e(\psi) + \sigma'_e(\omega)}{\psi^2 - \omega^2}d\psi \tag{3.11a}$$

$$\varepsilon''_{\text{eff}}(\omega) - \frac{\sigma'_e(\omega)}{\omega\varepsilon_0} = \frac{-2\omega}{\pi}\int_0^\infty \frac{\varepsilon'_{\text{eff}}(\psi) - \varepsilon'_{\text{eff}}(\omega)}{\psi^2 - \omega^2}d\psi - \frac{2\omega}{\pi\varepsilon_0}\int_0^\infty \frac{\sigma''_e(\psi)/\psi + \sigma''_e(\omega)/\omega}{\psi^2 - \omega^2}d\psi. \tag{3.11b}$$

If the material is purely dielectric and no free-moving charges are present $\sigma_e(\omega) = 0$, the Kramers-Kronig integrals in (3.11) reduce to the conventional dispersion relations of (2.46). Although the above derivations demonstrated that the electric conductivity is a complex-valued quantity, it will be only assumed a real-valued conductivity to simplify the solution of equations 3.11. Subsequently, (3.11) can be rewritten for $\sigma''_e(\omega) = 0$ as

$$\varepsilon'_{\text{eff}}(\omega) = 1 + \frac{2}{\pi}\int_0^\infty \frac{\psi\varepsilon''_{\text{eff}}(\psi) - \omega\varepsilon''_{\text{eff}}(\omega)}{\psi^2 - \omega^2}d\psi - \frac{2}{\pi\varepsilon_0}\int_0^\infty \frac{\sigma'_e(\psi) + \sigma'_e(\omega)}{\psi^2 - \omega^2}d\psi \tag{3.12a}$$

$$\varepsilon''_{\text{eff}}(\omega) = \frac{-2\omega}{\pi}\int_0^\infty \frac{\varepsilon'_{\text{eff}}(\psi) - \varepsilon'_{\text{eff}}(\omega)}{\psi^2 - \omega^2}d\psi + \frac{\sigma'_e(\omega)}{\omega\varepsilon_0}. \tag{3.12b}$$

Equations (3.12) will be utilized for all the obtained results throughout this chapter.

3.4 Numerical Results

3.4.1 Algorithm for Calculating the Electric Conductivity

While measuring the relative permittivity of any dispersive dielectric material, the results may be ambiguous if the losses are dielectric or conductive. This ambiguity could be attributed to the contribution of the electric conductivity to the corresponding real and imaginary parts of the effective relative permittivity, as illustrated in (3.8). However, in practice, the imaginary part of the complex-valued relative permittivity is usually considered to include both the dielectric and conductive losses. Therefore, we analytically utilize the KK integrations (3.12) to separate the electric conductivity from the complex-valued relative permittivity over a broad band of frequencies. For this purpose, two algorithms are suggested [45] as follows:

(1) Assume some artificial values of the real or the imaginary parts of the effective permittivity (indicated by the initial values). After that, the KK transformations are numerically applied to the real part of the initial values to calculate the corresponding imaginary part. If the obtained values of the KK-transformed imaginary part differ from the initial values of the imaginary part, then a conductive loss exists.

(2) Apply the KK transformations on the imaginary part of the initial values in (1). If the KK-transformed values of the real part do not match the initial values of the real part, we deduce that there is a conductive loss included in the imaginary part, which can be found by solving the corresponding integral equation.

To check the validity of the proposed algorithms, we start from some artificial values of the complex permittivity and of the conductivity:

i. Beginning by (3.12a) and considering the initial values suggested in the algorithms (1) and (2), while assuming no free-moving charges exist, i.e., $\sigma_e(\omega) = 0$, the real part of the effective permittivity $\varepsilon'_{\text{eff}}(\omega)$ can be directly computed from the given $\varepsilon''_{\text{eff}}(\omega)$.

ii. To check the consistency of the KK transformations, the calculated values of $\varepsilon'_{\text{eff}}(\omega)$ in (i) are reused to recalculate $\varepsilon''_{\text{eff}}(\omega)$ using (3.12b) while keeping $\sigma_e(\omega) = 0$. Steps (i) and (ii) for zero conductivity will be indicated henceforward as conventional KK transformations.

iii. Next, for a real-valued conductivity, i.e., $\sigma'_e(\omega) > 0$, the first integral of the KK transform of (3.12a) is performed on the initial values of $\varepsilon''_{\text{eff}}(\omega)$. By subtracting from the result the values of $\varepsilon'_{\text{eff}}(\omega)$, we get an integral equation for $\sigma'_e(\omega)$. By solving this equation, the electric conductivity can be computed.

iv. Perform the KK transform of (3.12b) on the initial values of $\varepsilon'_{\text{eff}}(\omega)$ and subtract the result from the values of $\varepsilon''_{\text{eff}}(\omega)$, we directly obtain the electric conductivity $\sigma'_e(\omega)$.

The last two steps (iii) and (iv) will be utilized to separate the conductivity from the imaginary part of the effective permittivity. However, the step (iv) is preferred where it leads to a direct extraction of the real part of the electric conductivity.

3.4.2 Check of Consistency

The conventional KK transformations for $\sigma_e(\omega) = 0$ are applied to check the self-consistency between the two equations in (3.11). For non-conductive materials like dielectric insulators is the effective permittivity in (3.8) equal to the relative permittivity in (2.7a), and hence the Kramers-Kronig transforms (3.11) are equivalent to that in (2.46).

We start with a check of the self-consistency of the proposed algorithms. The red solid curve in Fig. 3.1a represents the fictitiously synthesized imaginary part of the complex relative permittivity when $\sigma_e(\omega) = 0$, while the corresponding real part of the complex relative permittivity (solid red curve in Fig. 3.1b) is numerically computed using the KK-transform in (2.7a). The latter has been reused for a self-consistency of the KK transformations using (2.7b) to recalculate the imaginary part as shown in the broken blue curve in Fig. 3.1a. Again, the obtained KK-transformed values of the blue curve in Fig. 3.1a are re-utilized using (2.7a) to recompute the real part as indicated in the broken blue curve shown in Fig. 3.1b, it is referred to as double KK-transform (DKK)). We observe that the data obtained for the real part of the relative permittivity are consistent with the initial data, even after the three-times KK transformation shows a reasonable agreement apart from a deviation at the end of the observation interval.

3.4.3 Conductivity Retrieval Using the Kramers-Kronig Integrals

This section numerically investigates the utilization of the Kramers-Kronig transformations to calculate or separate the electric conductivity from the imaginary part of the given effective permittivity. We reassume the algorithms mentioned above but with a non-zero conductivity. Consequently, two different cases of the real-valued conductivity are suggested and added to the initial values of $\varepsilon''_{\text{eff}}(\omega)$ in Fig. 3.1a, whereas the imaginary part is kept zero ($\sigma''_e(\omega) = 0$). The prime will be omitted from σ'_e:

(1) a frequency-independent conductivity $\sigma_e > 0$. For instance, at $\sigma_e = 0.8$ S/m, the imaginary part of the effective permittivity is calculated from (3.8) as $\varepsilon''_{\text{eff}}(\omega) = \varepsilon''(\omega) + 0.8/(\omega\varepsilon_0)$.

(2) a frequency-dependent conductivity $\sigma_e(\omega) > 0$, then $\varepsilon''_{\text{eff}}(\omega) = \varepsilon''(\omega) + \sigma_e(\omega)/(\omega\varepsilon_0)$.

After that, we apply step (iv) in Section 3.4.1 to retrieve the values of the electric conductivity, suggested in the two cases (1) and (2), from the imaginary part of $\varepsilon_{\text{eff}}(\omega)$. The electric conductivity $\sigma_e(\omega)$in (3.12b) is calculated using (2.59) as

$$\sigma_e(\omega) = \omega\varepsilon_0\left\{\varepsilon''_{\text{eff}}(\omega) + \sum_{n=1}^{N}\int_{\psi_{n-1}}^{\psi_n}\frac{q_n(\psi) - \varepsilon'_{\text{eff}}(\omega)}{\psi^2 - \omega^2}d\psi + e_1\left\{\varepsilon'_{\text{eff}}(\psi_{\min}), \varepsilon'_{\text{eff}}(\psi_{\max}), \varepsilon'_{\text{eff}}(\omega)\right\}\right\}. \tag{3.13}$$

The initially synthesized values of the imaginary part of the relative permittivity in Fig. 3.1a are reused, but when the electric conductivity values are non-zero $\sigma_e(\omega) > 0$. It is evident from Fig. 3.2a that the imaginary part of the effective relative permittivity is shifted upwards for every added (real-valued) electric conductivity. Performing the conventional KK transforms (2.46) on the imaginary parts of the effective permittivity shown in Fig. 3.2a

results in different curves for the real part as shown in Fig. 3.2b. It is clear from Fig. 3.2a that by adding conductivity to the imaginary part of the relative permittivity, the KK-transformed values of the real part differ from that of the initial values. Therefore, the Kramers-Kronig transforms are ineffective for these data unless the conductivity is separated from the imaginary part $\varepsilon'_{\text{eff}}(\omega)$.

Equation (3.13) is applied to the data shown in Fig. 3.2a to retrieve the added conductivity values from the effective imaginary part $\varepsilon'_{\text{eff}}(\omega)$. It is clear in Fig. 3.2a that the blue curve results from adding a constant conductivity, while the pink one is for a frequency-dependent conductivity $\sigma_(\omega)$. Consequently, we strive to retrieve them both by utilizing (3.13). The upper and lower bounds of the integral in (3.13) must be specified as large enough to obtain correct and identical values to that of the initially added values when the integral is performed. As shown in Fig. 3.3, the calculated values of the conductivity diverge from the initial values (black curves in both figures of 3.3a and 3.3b) when the upper bound of the integration frequencies $\psi_{\max}$ is small, i.e., for $\psi_{\max} = 14\text{x}10^{10}$ s^{-1}. In contrast, the calculated values of σ_e converge to the initial ones as the upper frequency bound increases.

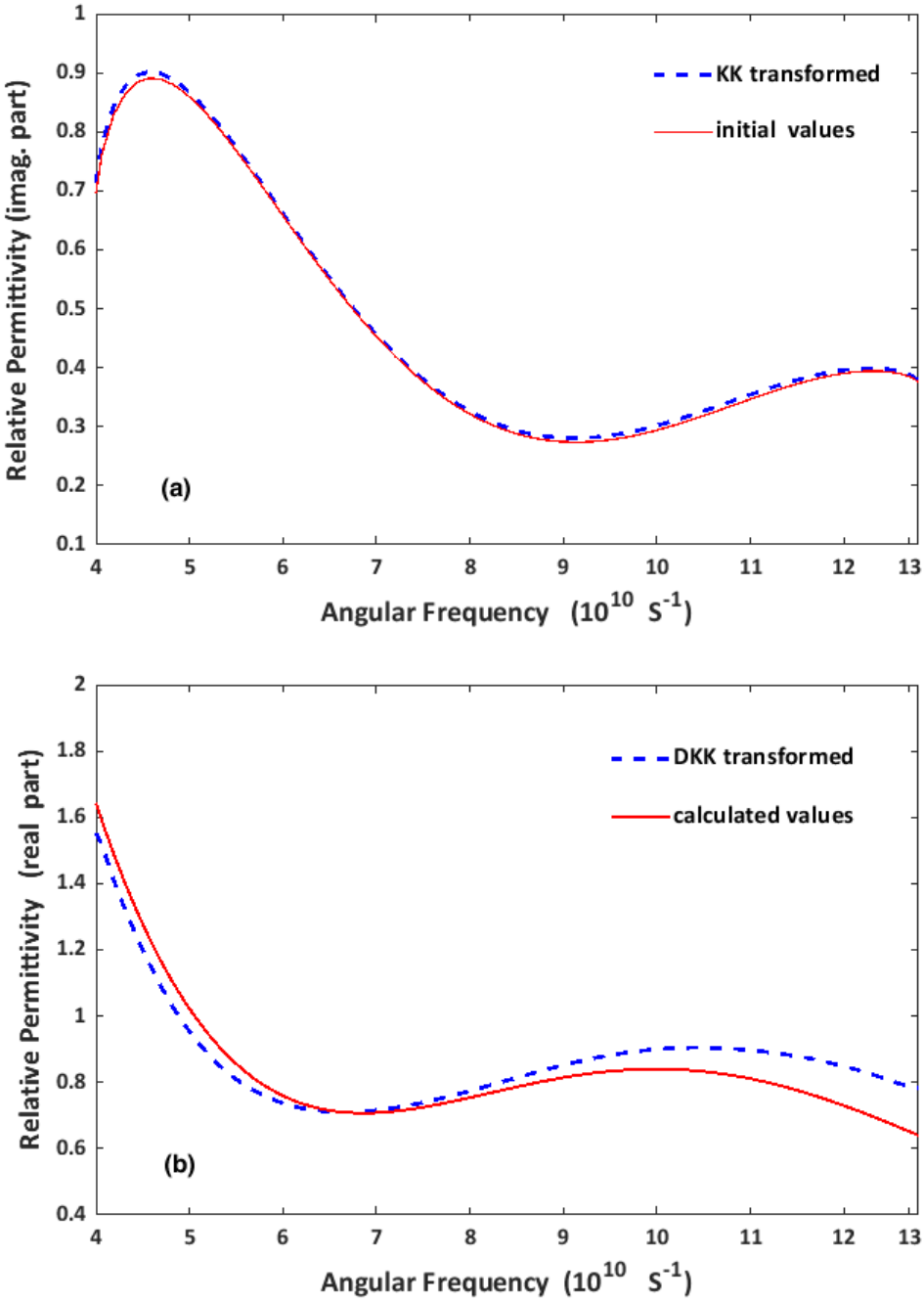

Figure 3.1: (**a**) The imaginary part and (**b**) the real part of the complex relative permittivity where no conductive losses are considered. From the initial values of $\varepsilon''_{\text{eff}}$ (red solid curve in (**a**)), the solid red curve in (**b**) is computed using (3.12a). The latter is reused (for self-consistency) to recalculate the imaginary part using (3.12b) as depicted in the broken blue curve in (**a**). The latter is also reused to recalculate the real part as shown in double KK-transformed (DKK) values [45].

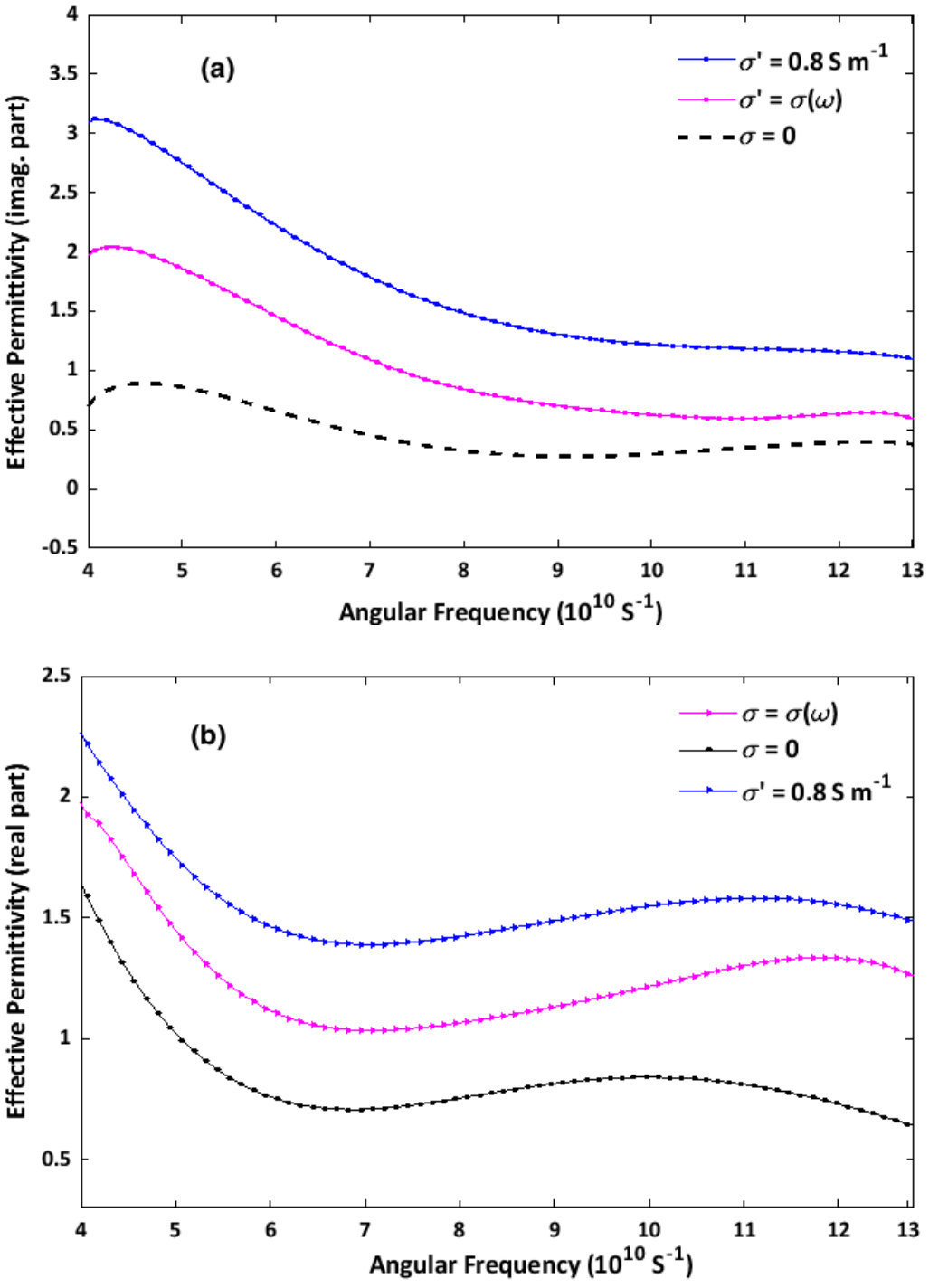

Figure 3.2: (**a**) The imaginary part of the effective complex permittivity for different values of σ_e. (**b**) the Kramers-Kronig transformed values of the real part of $\varepsilon_{\text{eff}}(\omega)$ calculated using Eq. (2.46a). Only the black curve at $\sigma_e = 0$ represent the initial values of the effective relative permittivity, while the other curves illustrate the effect of the conductivity on the real and imaginary parts of $\varepsilon_{\text{eff}}(\omega)$.

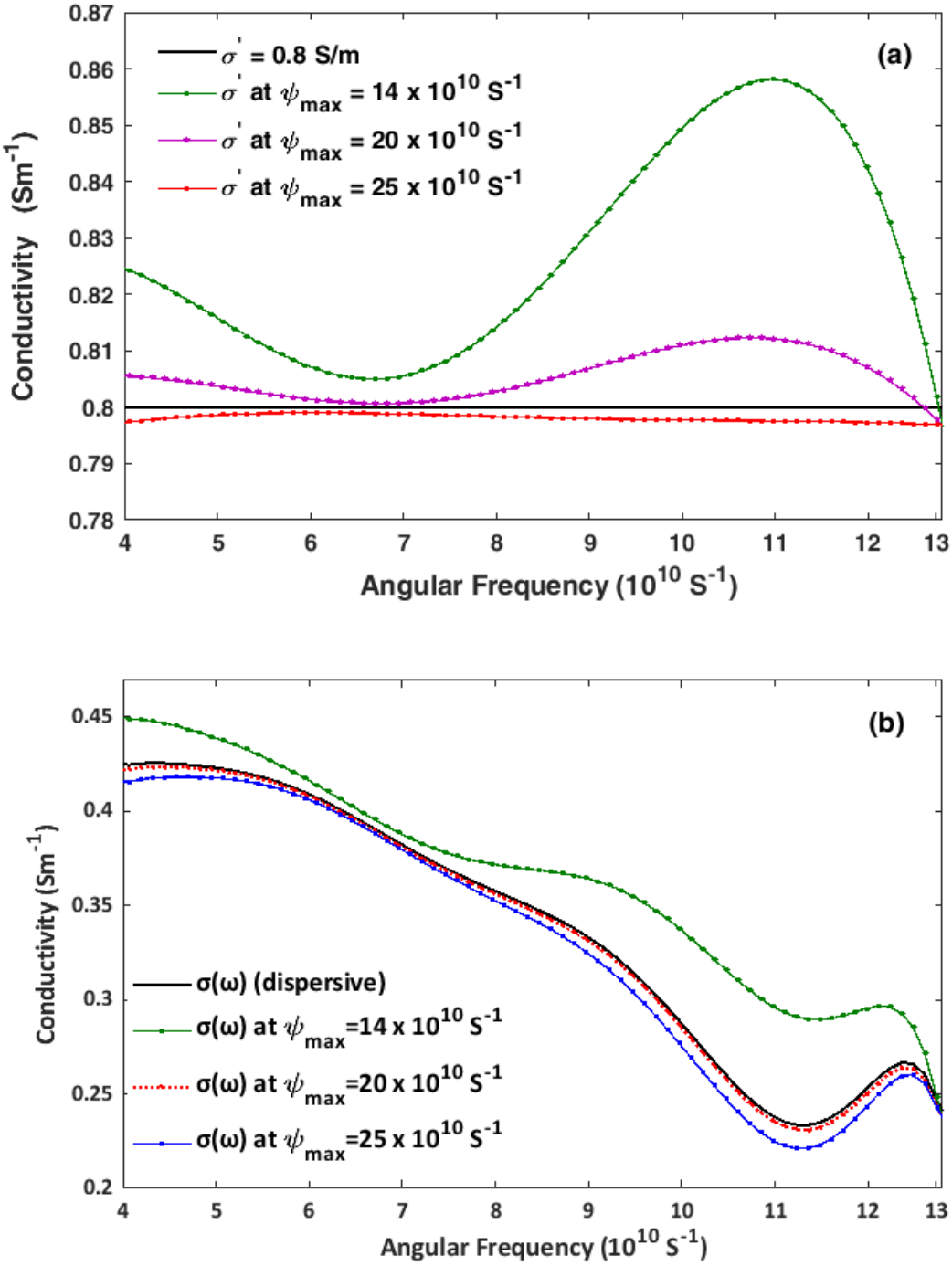

Figure 3.3: The calculated conductivity values for a (**a**) frequency-independent and (**b**) frequency-dependent conductivity added to the imaginary part of $\varepsilon_{\text{eff}}(\omega)$ shown in Fig. 3.2. The integral in (3.13) is performed at different values of $\psi_{\max}$, while $\psi_{\min}$ maintained at $0.6\text{x}10^{10}$ s^{-1}.

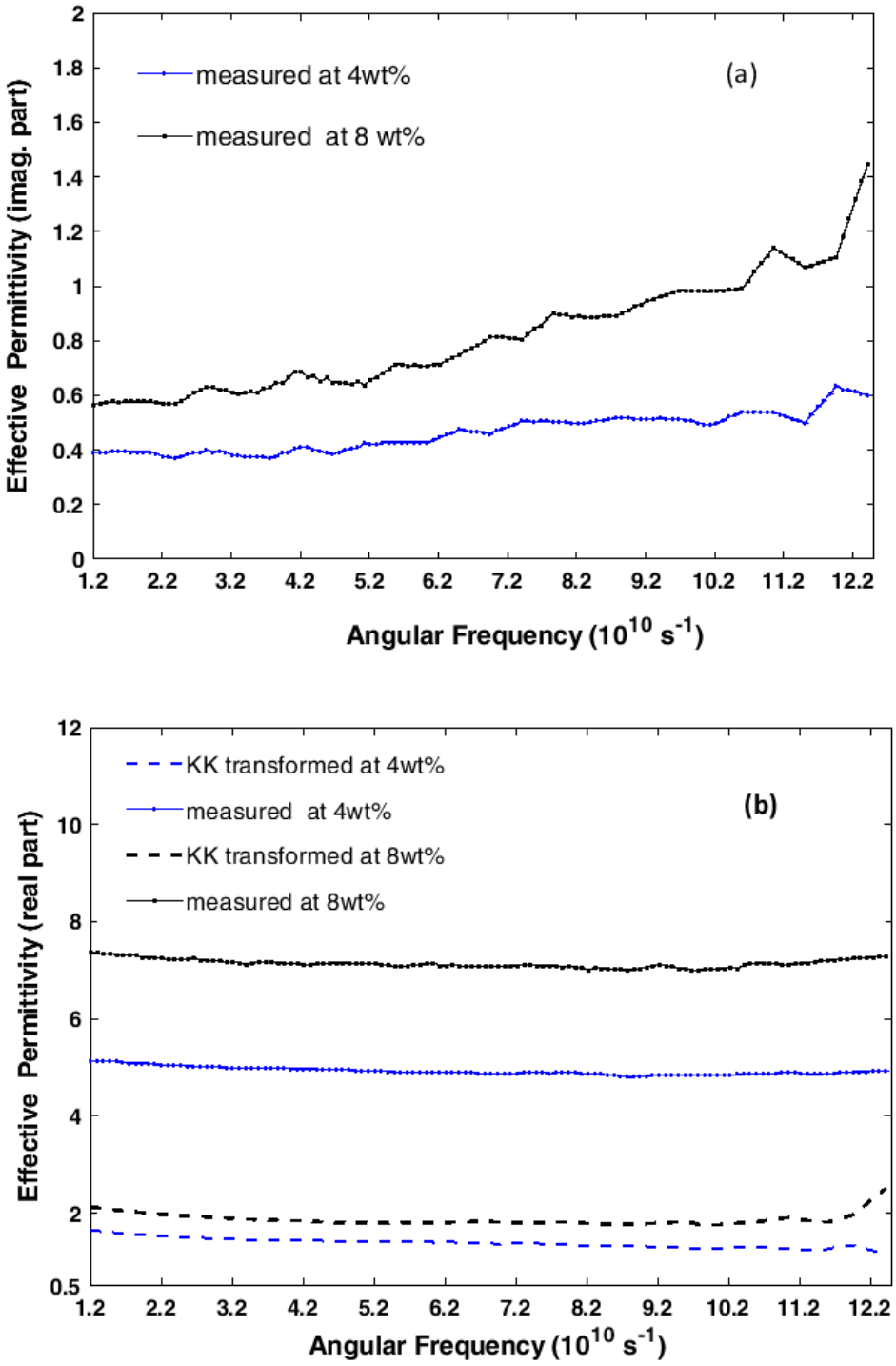

Figure 3.4: A measured effective relative permittivity for CNT composite material: (**a**) measured imaginary part (**b**) measured real part (solid curves) at different weight fractions (wt%). The broken curves in (**b**) are the KK-transformed values of the corresponding imaginary values shown in (**a**).

3.5 Conductivity Calculation from a Measured Complex Permittivity

Composite materials are engineered or natural materials made of two or more mixed materials with different chemical or physical properties to produce a material with properties different than the individual constituents [50], [51]. These materials are classified in different forms, such as layered nanostructures [52], [53] or matrix composites, where the solid nanospheres of two or more different materials are incorporated in the host material, e.g., the composition of graphene with different materials [54], [55]. The constituents can be insulators, metals, or semiconductors, provided that the size of the constituents is much smaller than the wavelength of the incident wave. According to the effective medium theory provided by Bruggeman [56] for combining two different materials, the relative permittivity ε_r of the individual material is replaced by the effective relative permittivity ε_{eff} of the composite. Different equations for calculating the effective permittivity of composite materials were derived as in [57] [58], where the effect of the dielectric and the conductive charges in the concerned material was considered. Combining different materials leads to a frequency dispersion of composite material properties such as permittivity, permeability, and conductivity.

In this section, we perform the same procedure mentioned in Section 3.4.3 for calculating the electric conductivity from the complex effective permittivity of some measured values of ε_{eff} of the Carbon nanotubes (CNTs) composite materials found in the literature [59]. The multi-walled Carbon nanotube composites are experimentally prepared with the epoxy resin at different weight fractions (wt%) for designing an electromagnetic absorber in the frequency range of 2-20 GHz. The CNTs are considered good conductors, i.e., when adding CNTs to the composite, free-moving charges exist, resulting in a change in the measured values of the imaginary part of the complex permittivity, as clearly shown in Fig. 3.4. When the weight fraction of the CNTs to the composite increases, a corresponding increase in the measured relative permittivity and permeability values occurs.

The Kramers-Kronig integrations of (3.12) and (3.13) are applied to the data shown in Fig. 3.4 to calculate or separate the conductivity values from the measured values of the imaginary part of the effective permittivity. The original values of the real and imaginary parts of the effective permittivity, referred to as measured values as in Fig. 3.4, are obtained from [59]. Firstly, we apply the KK integrations (2.46) to the imaginary parts in Fig. 3.4a, yielding the corresponding real parts of the effective permittivity (broken curves) shown in Fig. 3.4b. It is evident in Fig. 3.4b that the KK-transformed values of the real part of the effective permittivity are not matched with the corresponding original (measured) values shown in solid curves in Fig. 3.4b, i.e., the imaginary part must have conductivity, which we wish to calculate. After that, applying (3.12) to data in Fig. 3.4 a, results in calculating the desired values of the real-valued conductivity of the composite material as a function of the frequency, as depicted in Fig. 3.5. Only the real part of the dispersive conductivity is calculated according to the hypothesis mentioned above, where the conductivity does not include the imaginary part.

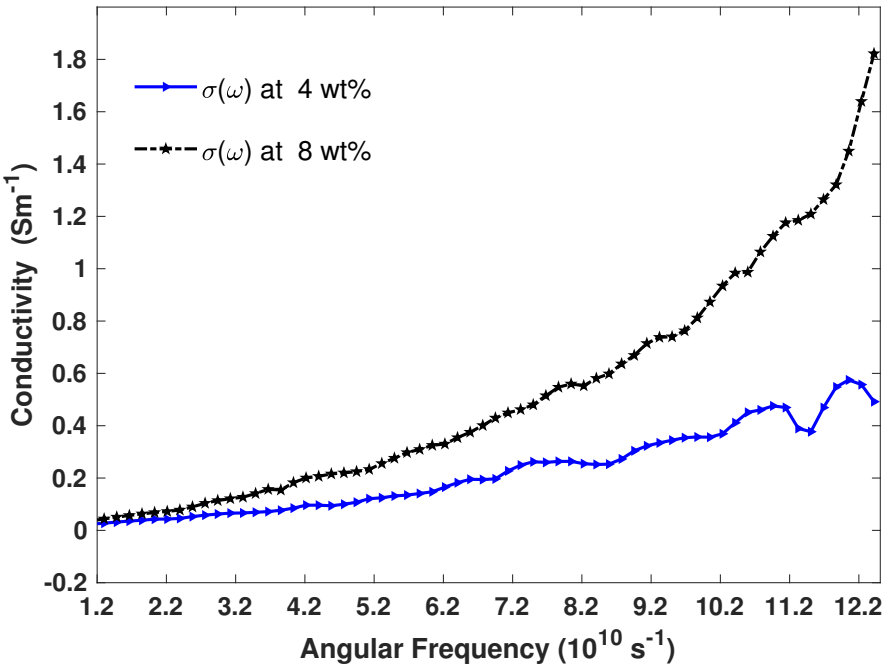

Figure 3.5: Conductivity retrieved by the proposed method from the measured values of the effective relative permittivity of Fig. 3.4 for different CNT composite materials. The measured values were found in [48].

In conclusion, the derivations mentioned above of the Kramers-Kronig integrations and the proposed algorithms for calculating the electric conductivity are numerically verified on artificial and measured values of the effective permittivity of dispersive lossy materials. The results demonstrate the robustness of the proposed method and prove that the KK transformations are valid for calculations as long as a frequency dispersion in the given data exists and the constraints mentioned in Section 2.6 are satisfied.

4. Matching of Electrically Small Antennas to Lossy Media

This chapter studies the issue of the energy transmission and matching of infinitesimally electric and magnetic antennas to lossy media like biological tissues. Most biomedical applications and radiation therapies utilize antennas as a source of electromagnetic energy transmission. Consequently, direct or indirect contact between the antenna element and the biological tissues is preferred to ensure a better energy transfer [23], [24]. However, in practice, a potential poor matching between the antenna element and the biological tissues arises due to the high dispersion characteristics in permittivity and conductivity of the bio-tissues.

Furthermore, another problem is the drastically miniaturized size of infinitesimally small electric and magnetic antennas. Due to the strongly reduced size of the radiating element, the reactively stored electric and magnetic energies in the near field region surrounding the antenna increase, leading to a significant decrease in the radiation resistance and a high increase in the Q-factor, which narrows the operating bandwidth of the antenna.

We propose a method to analytically investigate the antenna's matching problem to the biological tissues using dielectric dispersive material placed between the antenna element and the bio-tissues. The antenna element with a maximum dimension ($\kappa a \ll 1$) is supposed to be concentric in a multi-layered sphere, where a is the radius of the innermost sphere. The medium in the minimum sphere coating the antenna is lossless, while the outer sphere layers are supposed to contain dispersive materials like biological tissues. By placing the antenna at the center of the multi-layered sphere, the radiated electromagnetic fields outside the minimum sphere (for $r > a$), i.e., inside the dispersive media, can be expanded using the vectorial spherical harmonics [28]. The optimum matching between the antenna element and the surrounding dispersive media will be estimated by compensating for the stored electromagnetic energies in each sphere. The problem is firstly analyzed at a single frequency and then expanded over a broader range of frequencies using the dispersion relations of the Kramers-Kronig transformations.

4.1 Spherical Multipole Expansion of the Radiated Electromagnetic Fields

In a source-free medium, the electric and magnetic fields are coupled through the Maxwell equations

$$\vec{\nabla} \times \vec{E}(\vec{r},\omega) = -j\omega\mu(\omega)\vec{H}(\vec{r},\omega) \tag{4.1a}$$

$$\vec{\nabla} \times \vec{H}(\vec{r},\omega) = j\omega\varepsilon_{\text{eff}}(\omega)\vec{E}(\vec{r},\omega), \tag{4.1b}$$

where $\mu(\omega)$ and $\varepsilon_{\text{eff}}(\omega)$ are the frequency-dependent components of the permeability ad effective permittivity. It is noticeable in (4.1) that the radial component of the electric field is not related to the radial component of the magnetic field due to the existence of the transversal components. Therefore, we try to split the electric and the magnetic fields into two components [28] as

$$\vec{E}(\vec{r},\omega) = \vec{E}_1(\vec{r},\omega) + \vec{E}_2(\vec{r},\omega) \tag{4.2a}$$

$$\vec{H}(\vec{r},\omega) = \vec{H}_1(\vec{r},\omega) + \vec{H}_2(\vec{r},\omega). \tag{4.2b}$$

Like the multipole function $\vec{N}$ defined in section 2.2.2, which contains radial and transversal components of the electromagnetic fields and the multipole function $\vec{M}$, which contains only transversal components, the components E_1 and H_1 are considered similar to the multipole function $\vec{N}$. Subsequently, they can be represented in free space for all propagating modes as

$$\vec{E}_1(\vec{r},\omega) = \sum_{nm} a_{nm}\vec{N}_{nm}(\vec{r},\omega) \tag{4.3a}$$

$$\vec{H}_1(\vec{r},\omega) = \sum_{nm} b_{nm}\vec{N}_{nm}(\vec{r},\omega), \tag{4.3b}$$

where a_{nm} and b_{nm} are the electric and magnetic multipole amplitudes in V/m and A/m, respectively. Using the identities in (2.33), the second components E_2 and H_2 can be interrelated to H_1 and E_1 as

$$\begin{aligned}\vec{E}_2(\vec{r},\omega) &= \frac{1}{j\omega\varepsilon_{\text{eff}}(\omega)}\vec{\nabla} \times \vec{H}_1(\vec{r},\omega) \\ &= \frac{Z(\omega)}{j}\sum_{nm} b_{nm}\vec{M}_{nm}(\vec{r},\omega)\end{aligned} \tag{4.4a}$$

$$\begin{aligned}\vec{H}_2(\vec{r},\omega) &= -\frac{1}{j\omega\mu(\omega)}\vec{\nabla} \times \vec{E}_1(\vec{r},\omega) \\ &= \frac{j}{Z(\omega)}\sum_{nm} a_{nm}\vec{M}_{nm}(\vec{r},\omega),\end{aligned} \tag{4.4b}$$

where $Z = \sqrt{\mu/\varepsilon_{\text{eff}}}$ is the intrinsic impedance and is considered as a complex frequency-dependent quantity according to the frequency-dependent permittivity and permeability.

By combining (4.3) and (4.4), the general expression of the spherical multipole expansion of the electromagnetic fields is written as

$$\vec{E}(\vec{r},\omega) = \sum_{n=1}^{\infty}\sum_{m=-n}^{+n} a_{nm}\vec{N}_{nm}(\vec{r},\omega) + \frac{Z}{j}\sum_{n=1}^{\infty}\sum_{m=-n}^{+n} b_{nm}\vec{M}_{nm}(\vec{r},\omega) \tag{4.5a}$$

$$\vec{H}(\vec{r},\omega) = \frac{j}{Z}\sum_{n=1}^{\infty}\sum_{m=-n}^{+n} a_{nm}\vec{M}_{nm}(\vec{r},\omega) + \sum_{n=1}^{\infty}\sum_{m=-n}^{+n} b_{nm}\vec{N}_{nm}(\vec{r},\omega). \tag{4.5b}$$

These formulas represent a complete set of spherical electromagnetic fields in an isotropic and homogeneous medium. The following section defines a particular case of (4.5) for electrically small antennas.

4.2 Spherical Multipole Expansion of Electrically Small Antennas

Using (2.29) and (2.30), the electric and magnetic fields in (4.5) can be separated into two parts in the spherical multipole expansion. One part is associated with the electrical multipole amplitudes a_{nm}, referred to as TM_{nm} mode, and the other is related to the magnetic multipole amplitudes b_{nm}, denoted as TE mode. We will consider only the TM mode; therefore, the electromagnetic fields in (4.5) are represented for a TM mode as

$$E_r(r,\omega) = -a_{nm}(n^2+n)\frac{z_n(\kappa r)}{\kappa r}Y_{nm}(\vartheta,\varphi) \tag{4.6a}$$

$$E_\vartheta(r,\omega) = -a_{nm}\frac{1}{\kappa r}\frac{d}{dr}\big(rz_n(\kappa r)\big)\frac{\partial Y_{nm}(\vartheta,\varphi)}{\partial\vartheta} \tag{4.6b}$$

$$E_\varphi(r,\omega) = -a_{nm}\frac{1}{\kappa r}\frac{d}{dr}\big(rz_n(\kappa r)\big)\frac{1}{\sin\vartheta}\frac{\partial Y_{nm}(\vartheta,\varphi)}{\partial\varphi} \tag{4.6c}$$

$$H_r(r,\omega) = 0 \tag{4.6d}$$

$$H_\vartheta(r,\omega) = -a_{nm}\frac{j}{Z}z_n(\kappa r)\frac{1}{\sin\vartheta}\frac{\partial Y_{nm}(\vartheta,\varphi)}{\partial\varphi} \tag{4.6e}$$

$$H_\varphi(r,\omega) = a_{nm}\frac{j}{Z}z_n(\kappa r)\frac{\partial Y_{nm}(\vartheta,\varphi)}{\partial\vartheta}, \tag{4.6f}$$

where z_n represents the spherical Bessel function, while $Y_{n,m}$ is the spherical harmonic function. The degree m represents the azimuthal change $0 \leq \varphi \leq 2\pi$, while the term n represents the the multipole order, i.e. $n = 0$ represents a monopole, $n = 1$ for a dipole, $n = 2$ for a quadrupole and so on.

We consider an infinitesimally (Hertzian) electric dipole antenna (henceforward will be referred to as electrically small antenna (ESA) [60]) with a length $l \ll \lambda$ and excited with a constant electric current I_o is placed at the center of a three-layered sphere as shown in Fig. 4.1. The spherical coordinate system (r,ϑ,φ) is considered. The outermost sphere extends to infinity and is assumed to contain biological tissues. Assuming the dipole antenna is matched to free space and has a symmetric omnidirectional far field pattern in the azimuthal plane, only a TM_{10} mode exists with radiated electromagnetic fields defined in terms of the excitation current I_o according to ([61] Ch. 4) and (4.6) as

$$E_r^p|_{p=0} = -2E_o Z_p \frac{h_1^{(2)}(\kappa_p r)}{r} \cos\vartheta \tag{4.7a}$$

$$E_\vartheta^p|_{p=0} = \frac{E_o Z_p}{r} \frac{d}{d\kappa_p r}\left(\kappa_p r h_1^{(2)}(\kappa_p r)\right) \sin\vartheta \tag{4.7b}$$

$$H_\varphi^p|_{p=0} = -jE_o \kappa_p h_1^{(2)}(\kappa_p r) \sin\vartheta, \tag{4.7c}$$

where the superscript $p = 0, 1, 2$ refers to the sphere layer-order. Due to the azimuthal symmetry, the degree $m = 0$, while $n = 1$ to represent the dipole. The amplitude E_o and the spherical Hankel function $h_1^{(2)}$ are written as

$$E_o = \frac{\kappa_0 I_o l}{4\pi} \tag{4.8a}$$

$$h_1^{(2)}(\kappa_p r) = \big(-\frac{1}{\kappa_p r} - \frac{j}{(\kappa_p r)^2}\big) e^{-j\kappa_p r}. \tag{4.8b}$$

Since the antenna is in transmitting mode, the spherical Hankel function of the second kind $h_1^{(2)}$ is taken in (4.7) to represent the outwardly radiated electromagnetic fields in the three-layered sphere. The space in the minimum sphere $r < a$ surrounding the dipole element is considered lossless with permittivity and permeability of free space $\varepsilon = \varepsilon_0$ and $\mu = \mu_0$, respectively.

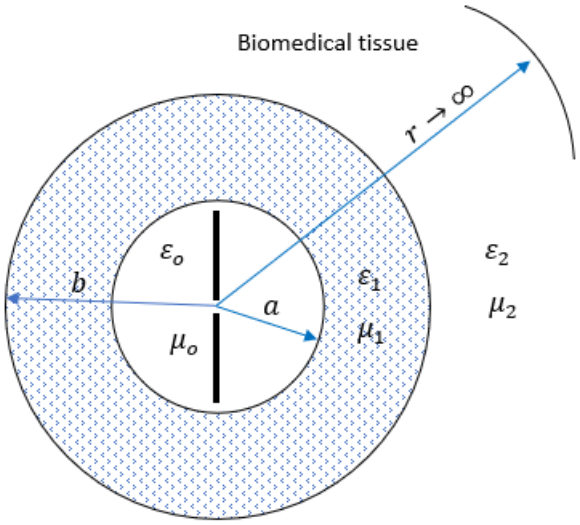

Figure 4.1: Manifestation of the infinitesimally electric dipole antenna enclosed within a three-layered sphere.

4.2.1 Multipole Expansion of ESA in a Three-layered Sphere

By placing the antenna element symmetrically at the center of the three-layered sphere, the radiated electromagnetic fields outside the minimum sphere $r > a$ can be expanded using

the spherical multipole expansion defined in (4.6). Consequently, the electric and magnetic fields in the middle sphere $a < r < b$ are represented as

$$E_r^p|_{p=1} = -\sqrt{\frac{3}{\pi}} A \cos\vartheta \frac{z_1(\kappa_p r)}{\kappa_p r} \tag{4.9a}$$

$$E_\vartheta^p|_{p=1} = \sqrt{\frac{3}{4\pi}} A \sin\vartheta \frac{1}{\kappa_p r} \frac{d}{dr}\big(r z_1(\kappa_p r)\big) \tag{4.9b}$$

$$H_\varphi^p|_{p=1} = \sqrt{\frac{3}{4\pi}} A \sin\vartheta \frac{1}{jZ_p} z_1(\kappa_p r), \tag{4.9c}$$

while for the outer sphere $r > b$

$$E_r^p|_{p=2} = -\sqrt{\frac{3}{\pi}} B_3 \cos\vartheta \frac{h_1^{(2)}(\kappa_p r)}{\kappa_p r} \tag{4.10a}$$

$$E_\vartheta^p|_{p=2} = \sqrt{\frac{3}{4\pi}} B_3 \sin\vartheta \frac{1}{\kappa_p r} \frac{d}{dr}\big(r h_1^{(2)}(\kappa_p r)\big) \tag{4.10b}$$

$$H_\varphi^p|_{p=2} = \sqrt{\frac{3}{4\pi}} B_3 \sin\vartheta \frac{1}{jZ_p} h_1^{(2)}(\kappa_p r). \tag{4.10c}$$

The material in the outer sphere $r > a$ is considered isotropic, homogeneous, and lossy with frequency-dependent permittivity and permeability ε_p, μ_p, respectively. The intrinsic impedance $Z_p = \sqrt{\mu_p/\varepsilon_p}$ and the wavenumber $\kappa_p = \omega\sqrt{\mu_p\varepsilon_p}$ are frequency-dependent quantities, while A and B_3 represent the electric multipole amplitudes in the middle and outer spheres, respectively. For the middle sphere, a combination of the first and second kind Hankel functions is preferably chosen as $z_1(\kappa_1 r) = C_1 h_1^{(1)}(\kappa_1 r) + C_2 h_1^{(2)}(\kappa_1 r)$ to represent the spherical Bessel function z_1 in (4.9), while for the outer sphere $r > b$, the spherical Bessel function z_1 is replaced by a sphere Hankel function of the second kind $h_1^{(2)}$ to represent the outwardly propagating waves. Consequently, the electromagnetic fields in the middle sphere may be rewritten in the form

$$E_r^p|_{p=1} = -\sqrt{\frac{3}{\pi}} \cos\vartheta \frac{1}{\kappa_p r}\big[B_1 h_1^{(1)}(\kappa_p r) + B_2 h_1^{(2)}(\kappa_p r)\big] \tag{4.11a}$$

$$E_\vartheta^p|_{p=1} = \sqrt{\frac{3}{4\pi}} \sin\vartheta \frac{1}{\kappa_p r} \frac{d}{d\kappa_p r}\big[\kappa_p r B_1 h_1^{(1)}(\kappa_p r) + \kappa_p r B_2 h_1^{(2)}(\kappa_p r)\big] \tag{4.11b}$$

$$H_\varphi^p|_{p=1} = \sqrt{\frac{3}{4\pi}} \sin\vartheta \frac{1}{jZ_p}\big[B_1 h_1^{(1)}(\kappa_p r) + B_2 h_1^{(2)}(\kappa_p r)\big], \tag{4.11c}$$

where $B_1 = AC_1$ and $B_2 = AC_2$ are the electric multipole amplitudes of the electromagnetic fields confined in the middle sphere $a < r < b$. The equations (4.7), (4.10), and (4.11) will be utilized to estimate the optimum matching between the antenna element and the surrounding dispersive medium.

4.2.2 Exact Solutions for the Multipole Amplitudes

By treating the three-layered sphere as a straightforward boundary-value problem, the electric multipole amplitudes B_1, B_2 and B_3 can be calculated from the tangential components

of the electric and magnetic fields of (4.7)-(4.11) as follows:
At $r = a$

$$B_1 \frac{\Gamma_{v,p}(\kappa_p a)}{\kappa_p}\Big|_{v=1,p=1} + B_2 \frac{\Gamma_{v,p}(\kappa_p a)}{\kappa_p}\Big|_{v=2,p=1} = \sqrt{\frac{4\pi}{3}} E_o Z_p \Gamma_{v,p}(\kappa_p a)|_{v=2,p=0} \tag{4.12a}$$

$$B_1 \frac{h_1^{(1)}(\kappa_p a)}{Z_p}\Big|_{p=1} + B_2 \frac{h_1^{(2)}(\kappa_p a)}{Z_p}\Big|_{p=1} = \sqrt{\frac{4\pi}{3}} E_o \kappa_p h_1^{(2)}(\kappa_p a)|_{p=0}. \tag{4.12b}$$

At $r = b$

$$B_1 \frac{\Gamma_{v,p}(\kappa_p b)}{\kappa_p}|_{v=1,p=1} + B_2 \frac{\Gamma_{v,p}(\kappa_p b)}{\kappa_p}|_{v=2,p=1} - B_3 \frac{\Gamma_{v,p}(\kappa_2 b)}{\kappa_p}|_{v=2,p=2} = 0 \tag{4.13a}$$

$$B_1 \frac{h_1^{(1)}(\kappa_p b)}{Z_p}|_{p=1} + B_2 \frac{h_1^{(2)}(\kappa_p b)}{Z_p}|_{p=1} - B_3 \frac{h_1^{(2)}(\kappa_p b)}{Z_p}|_{p=2} = 0, \tag{4.13b}$$

where Γ_1 and Γ_2 are the differentiation of the spherical Hankel functions and are defined as

$$\Gamma_{v,p}(\kappa_p r) = \kappa_p r \frac{\partial}{\partial \kappa_p r}\big(h_1^{(v)}(\kappa_p r)\big) + h_1^{(v)}(\kappa_p r), \tag{4.14}$$

with $v = 1, 2$ represents the first and second order of the spherical Hankel function. For $a < r < b$, the corresponding intrinsic impedance and wavenumber are defined as

$$Z_1(\omega) = \sqrt{\frac{\mu_1(\omega)}{\varepsilon_1(\omega)}}, \qquad \kappa_1(\omega) = \omega\sqrt{\mu_1(\omega)\varepsilon_1(\omega)},$$

while for the outer sphere $r > b$,

$$Z_2(\omega) = \sqrt{\frac{\mu_2(\omega)}{\varepsilon_2(\omega)}}, \qquad \kappa_2(\omega) = \omega\sqrt{\mu_2(\omega)\varepsilon_2(\omega)},$$

where $\varepsilon_1(\omega)$ and $\varepsilon_2(\omega)$ are complex frequency-dependent quantities. Equations (4.12) and (4.13) can be rearranged using the matrix multiplications as

$$\begin{bmatrix} \frac{\Gamma_{v,p}(\kappa_p a)}{\kappa_p}|_{v=1,p=1} & \frac{\Gamma_{v,p}(\kappa_p a)}{\kappa_p}|_{v=2,p=1} & 0 \\ \frac{\Gamma_{v,p}(\kappa_p b)}{\kappa_p}|_{v=1,p=1} & \frac{\Gamma_{v,p}(\kappa_p b)}{\kappa_p}|_{v=2,p=1} & -\frac{\Gamma_{v,p}(\kappa_p b)}{\kappa_p}|_{v=2,p=2} \\ \frac{h_1^{(1)}(\kappa_p b)}{Z_p}|_{p=1} & \frac{h_1^{(2)}(\kappa_p b)}{Z_p}|_{p=1} & -\frac{h_1^{(2)}(\kappa_p b)}{Z_p}|_{p=2} \end{bmatrix} \begin{bmatrix} B_1 \\ B_2 \\ B_3 \end{bmatrix} = \begin{bmatrix} \sqrt{\frac{4\pi}{3}} E_o Z_p \Gamma_{v,p}(\kappa_p a)|_{v=2,p=0} \\ 0 \\ 0 \end{bmatrix} \tag{4.15}$$

We assume that the outer sphere $r > b$ contains a lossy dielectric material with a complex-valued permittivity $\varepsilon_2 = 14 - j3$ while the material in the middle sphere $a < r < b$ is lossless with randomly selected permittivity values $\varepsilon_1 = 52$, and 65. The relative permeabilities μ_1 and μ_2 are chosen to be equal to unity. Assume that the infinitesimally electric dipole with a length $l = \lambda_0/30$ is fed by a constant electric current $I_o = 1$ A at a resonant frequency $f_0 = 1$ GHz, while the inner radius of the middle and the outer spheres are $a = l/2 = 5$ mm and $b = 60$ mm, respectively, (these dimensions are defined and fixed for all the obtained results in this chapter, except b is changeable). It is obvious from Fig. 4.2 that the tangential components of the electric and magnetic fields E_ϑ and H_φ are continuous across the boundaries. These results demonstrate the consistency of the above-derived equations in (4.7)-(4.15).

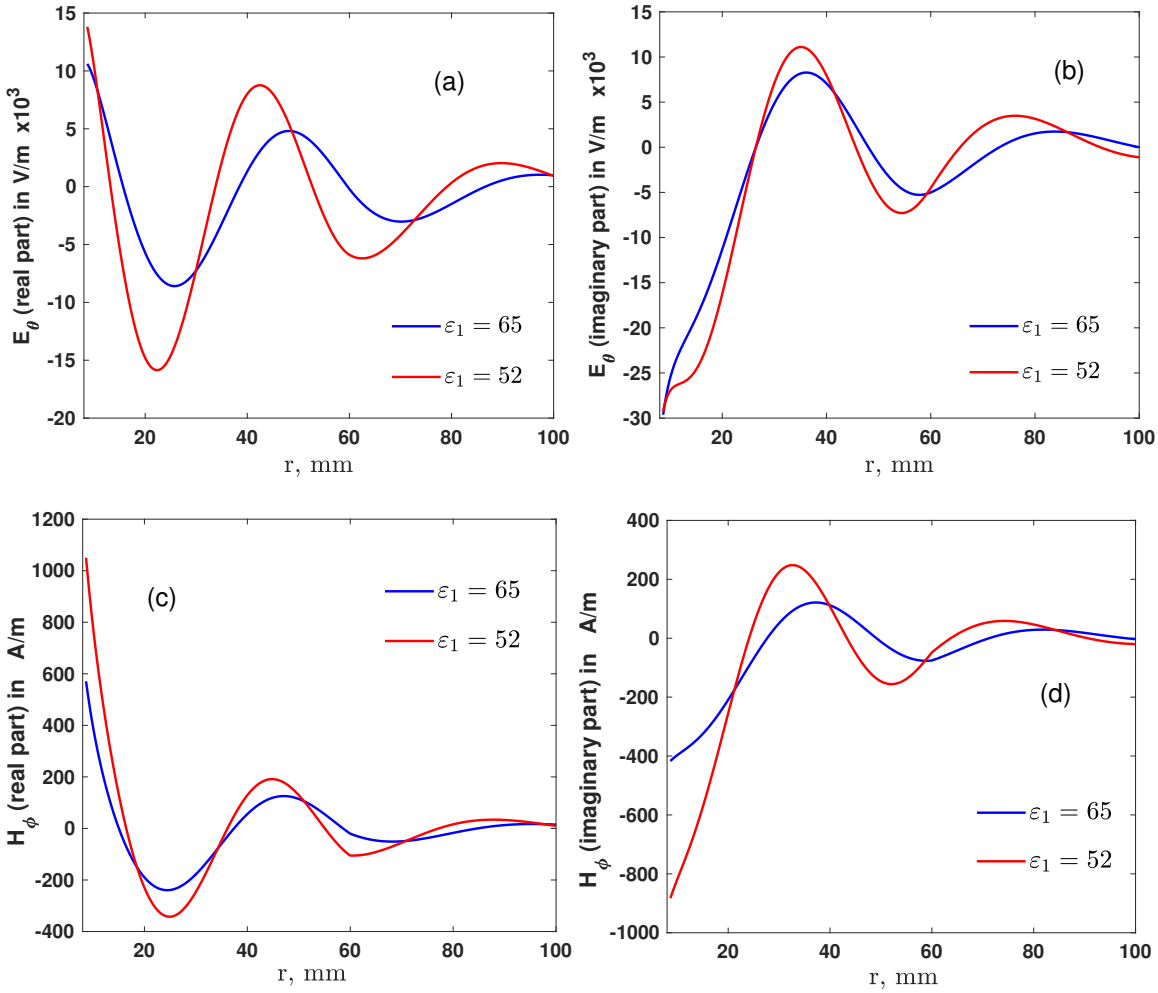

Figure 4.2: (**a**, **b**) The real and the imaginary parts of the tangential component of the electric field E_ϑ, (**c**, **d**) the real and the imaginary parts of the tangential component of the magnetic field H_φ. The outer sphere $r > b$ is assumed lossy with a complex-valued permittivity $\varepsilon_2 = 14 - j3$, while the material in the middle sphere is lossless with $\varepsilon_1 = 52$ and 65.

4.3 Definition of the Stored Electromagnetic Energies in Radiating Systems

This section investigates the stored and radiated electromagnetic energies of the electrically small antenna when the outer spheres contain lossy/dispersive materials. The time-averaged radiated power P_{rad} and the time-averaged reactive power P_{reac} flowing through the three-layered sphere are computed [62] as

$$P_{\text{rad}}(\omega) = \frac{1}{2}\text{Re}\oint_S \vec{E}\times\vec{H}^*\cdot d\vec{S} \tag{4.16a}$$

$$P_{\text{reac}}(\omega) = \frac{1}{2}\text{Im}\oint_S \vec{E}\times\vec{H}^*\cdot d\vec{S} = 2\omega(W_m(\omega) - W_e(\omega)), \tag{4.16b}$$

where S is the surface surrounding the antenna through which the power flows out, while W_e and W_m represent the stored electric and magnetic energies. It is evident in (4.16) that the stored electromagnetic energies represent the reactive energies and do not directly contribute to the radiation power of the antenna. If the materials in the spheres $r > a$ and $r > b$ are assumed highly dispersive with different values of $Z_1(\omega) \neq Z_2(\omega)$, a part of the radiated fields is reflected backwardly to the antenna, leading to a mismatch between the antenna element and the surrounding spheres. By compensating for the electromagnetic energies stored in the middle and outer spheres, i.e., the reactive power in the outer sphere is assumed to be equal in magnitude and opposite in sign to the reactive power in the middle sphere as defined in (4.17), the reactive energies can be eliminated, and better power radiation to the outer sphere can be accomplished.

$$\begin{aligned} P_{\text{reac}}^{(1)}(\omega) &= -P_{\text{reac}}^{(2)}(\omega) \\ \underbrace{W_m^{(1)}(\omega) + W_m^{(2)}(\omega)}_{W_m^t} &= \underbrace{W_e^{(1)}(\omega) + W_e^{(2)}(\omega)}_{W_e^t}, \end{aligned} \tag{4.17}$$

where the superscript refers to the sphere layer-order. We define an energy factor as

$$W_f(\omega) = \frac{W_m^t(\omega)}{W_e^t(\omega)}, \tag{4.18}$$

which evaluates the ratio between the total electric W_e^t and the total magnetic W_m^t energies stored in the middle and the outer spheres surrounding the antenna element. The resonance occurs when the stored electric and magnetic energies are equal, i.e., as the ratio between the total electric energy and magnetic energy approaches unity.

However, the definition of the stored electromagnetic energy in any radiating system is still ambiguous, where no direct and precise method describes the interaction between the radiated and the stored energies [63]. Therefore, the definition in (4.16) does not directly apply in radiating systems, particularly in lossy media. A more precise definition for the stored electric and magnetic energies was derived by McLean [64] and Yaghjian [60], where the stored electromagnetic energy is calculated by subtracting the total energy from the energy stored in the far field region around the radiating element as

$$W_e(r,\omega) = \frac{1}{4}\lim_{r\to\infty}\left\{ \iiint\limits_{v(r)} \text{Re}\left(\varepsilon_0\varepsilon_r \mid \vec{E}(r,\omega) \mid^2 dv\right) - \varepsilon_0 r \iint\limits_{\Omega} \mid \vec{\zeta}(\theta,\varphi) \mid^2 d\Omega \right\} \tag{4.19a}$$

$$W_m(r,\omega) = \frac{1}{4}\lim_{r\to\infty}\left\{ \iiint\limits_{v(r)} \text{Re}\left(\mu_0\mu_r \mid \vec{H}(r,\omega) \mid^2 dv\right) - \varepsilon_0 r \iint\limits_{\Omega} \mid \vec{\zeta}(\theta,\varphi) \mid^2 d\Omega \right\}, \tag{4.19b}$$

where $d\Omega = \sin\vartheta d\vartheta d\varphi$ is the solid angle integration element, and $\vec{\zeta}$ is the electric far field pattern [60] defined as

$$\zeta(\theta,\varphi) = \lim_{r\to\infty} r\vec{E}(r,\omega)e^{j\kappa r}. \tag{4.20}$$

The definition of the stored electromagnetic energy in (4.19) depends on the position of the chosen volume $v(r)$, i.e., the two integrals in (4.19a) or in (4.19b) do not depend on each

other, and thus, the integrals of the first part can be lonely performed unless the second integrals vanish [60]. Subsequently, an approximate definition of the stored electric and magnetic energies can be expressed as

$$\tilde{W}_e(r,\omega) \cong \frac{1}{4}\mathrm{Re}\iiint\limits_{v(r)} \varepsilon_0\varepsilon_r \mid \vec{E}(r,\omega) \mid^2 dv \tag{4.21a}$$

$$\tilde{W}_m(r,\omega) \cong \frac{1}{4}\mathrm{Re}\iiint\limits_{v(r)} \mu_0\mu_r \mid \vec{H}(r,\omega) \mid^2 dv. \tag{4.21b}$$

However, the derived formulas of the stored electromagnetic energy in (4.21) are only valid for non-dispersive materials. In case of lossy/dispersive materials, (4.21) must be recast in the form of (4.22), because the time-averaged energy in dispersive materials does not only depend on the instantaneous values of $\varepsilon_r(\omega)$ and $\mu_r(\omega)$ but also on their frequency derivatives according to Landau and Lifschitz [65] [Appendix B]

$$W_e(r,\omega) = \frac{1}{4}\mathrm{Re}\iiint\limits_{v(r)} \varepsilon_0\frac{d\big(\omega\varepsilon_r(\omega)\big)}{d\omega} \mid \vec{E}(r,\omega) \mid^2 dv \tag{4.22a}$$

$$W_m(r,\omega) = \frac{1}{4}\mathrm{Re}\iiint\limits_{v(r)} \mu_0\frac{d\big(\omega\mu_r(\omega)\big)}{d\omega} \mid \vec{H}(r,\omega) \mid^2 dv, \tag{4.22b}$$

where $\varepsilon_r(\omega) = \varepsilon'(\omega) - j\varepsilon''(\omega)$ and $\mu(\omega) = \mu'(\omega) - j\mu''(\omega)$. For a non-dispersive or lossless medium with no free charges $\sigma = 0$, the derivative of the imaginary part of $\varepsilon_r(\omega)$ and $\mu_r(\omega)$ vanishes, and the frequency derivative of the real part reduces to

$$\mathrm{Re}\big\{\big(\omega\varepsilon_r(\omega)\big)'\big\} = \varepsilon_r \tag{4.23a}$$

$$\mathrm{Re}\big\{\big(\omega\mu_r(\omega)\big)'\big\} = \mu_r, \tag{4.23b}$$

where the prime ($'$) in (4.23) refers to the partial differentiation with respect to the angular frequency ω.

We utilize (4.16a) to calculate the radiated power of the electrically small antenna into the outer spheres. We assume again that the material in the outer sphere $r > b$ is lossy with a complex-valued permittivity $\varepsilon_2 = 14 - j3$, while the material in the middle sphere $a < r < b$ is lossless with randomly selected values of ε_1. The relative permeabilities are assumed to be that of free space $\mu_1 = \mu_2 = 1$. The length of the dipole is kept as mentioned above $l = \lambda_0/30$ at $f_0 = 1$ GHz and the inner radius $a = l/2 = 5$ mm. Only the tangential components of the electric and magnetic fields E_ϑ and H_φ, respectively, contribute to computing P_{rad} in (4.16). It is evident from Fig. 4.2 that the tangential components of $\vec{E}$ and $\vec{H}$ are continuous through the boundaries; thus, the radiated power must also be continuous through the boundaries, as illustrated in Fig. 4.3. However, the lossy material in the outer sphere absorbs part of the electromagnetic energy resulting in a decrease in the radiated power for $r > b$.

4.3.1 Numerical Calculations of the Stored Electromagnetic Energies of ESA in Lossy Media

Next, we consider that the middle sphere exists ($b > a$). Thus, the stored electric and magnetic energies in the three-layered sphere shown in Fig. 4.1 can be numerically calculated

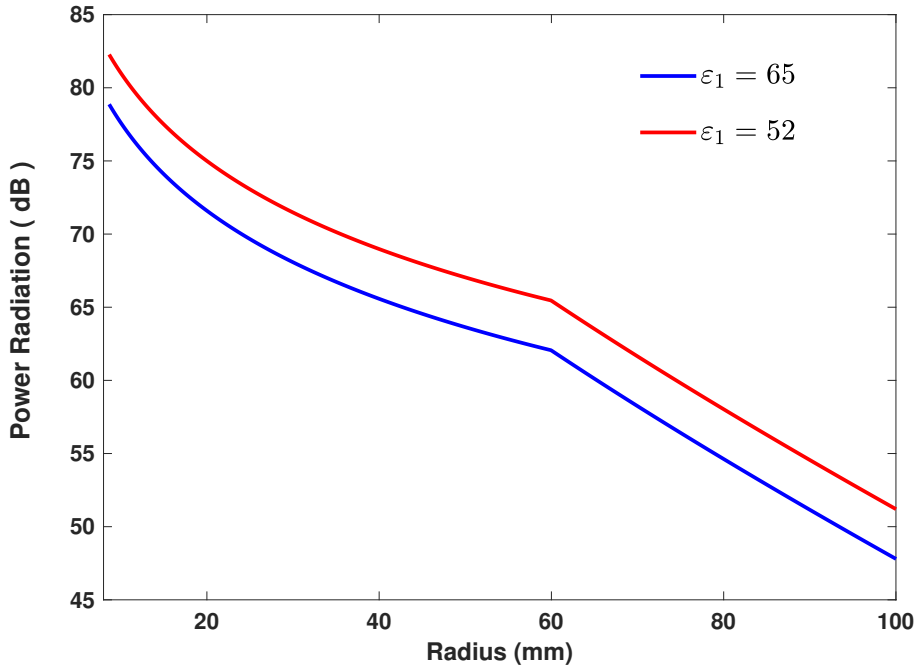

Figure 4.3: A comparison between the radiated powers of the electrically small antenna where the material in the outer sphere $r > b$ is lossy with $\varepsilon_2 = 14 - j3$, while the material in the middle sphere is lossless with $\varepsilon_1 = 52$ and 65.

according to the preceding definitions of the stored energies and the spherical multipole expansion of the electromagnetic fields. We assume that the medium in the minimum sphere enclosing the antenna element is lossless, and there is no energy stored for $r < a$. In addition, the materials in the outer spheres are assumed to be lossy with frequency-dependent permittivities $\varepsilon_1(\omega)$ and $\varepsilon_2(\omega)$. Subsequently, the stored electric and magnetic energies in each sphere can be calculated using (4.22) as

$$W_e^p(r,\omega) = \frac{1}{4}\int_r r^2 w_e^p dr \tag{4.24a}$$

$$W_m^p(r,\omega) = \frac{1}{4}\int_r r^2 w_m^p dr, \tag{4.24b}$$

with $p = 0, 1, 2$ denotes the sphere layer-order, while $w_e^{(p)}$ and $w_m^{(p)}$ are the angular integrations, which are defined as

$$w_e^p(r,\omega) = \int_0^{\pi}\int_0^{2\pi} G_e \mid \vec{E}^p(r,\omega) \mid^2 \sin\vartheta d\vartheta d\varphi \tag{4.25a}$$

$$w_m^p(r,\omega) = \int_0^{\pi}\int_0^{2\pi} G_m \mid \vec{H}^p(r,\omega) \mid^2 \sin\vartheta d\vartheta d\varphi. \tag{4.25b}$$

The functions G_e and G_m denote the frequency derivatives of the permittivity and permeability in (4.22). By substituting of the spherical multipole expansion of the electric and magnetic fields of (4.7)-(4.11) into (4.25), the stored electric and magnetic energies in the three-layered sphere can be calculated. In the middle sphere $a < r < b$, by substituting

of (4.11) into (4.25) with $G_e = (\omega\varepsilon_1(\omega))'$ and $G_m = (\omega\mu_1(\omega))'$, the angular integrations of the stored electric and magnetic energies of (4.25) are calculated as

$$w_e^p(r,\omega)|_{p=1} = \frac{2G_e}{|\kappa_p r|^2}\left\{2\left|B_1 h_1^{(1)}(\kappa_p r) + B_2 h_1^{(2)}(\kappa_p r)\right|^2 + \left|B_1\Gamma_1(\kappa_p r) + B_2\Gamma_2(\kappa_p r)\right|^2\right\} \quad (4.26a)$$

$$w_m^p(r,\omega)|_{p=1} = \frac{G_m}{2|Z_p|^2} \quad \left|B_1 h_1^{(1)}(\kappa_p r) + B_2 h_1^{(2)}(\kappa_p r)\right|^2. \quad (4.26b)$$

Substituting of (4.26) into (4.24), the radial integrations of the stored electric and magnetic energies are written as

$$W_e^p(r,\omega)|_{p=1} = \frac{G_e}{2|\kappa_p|^2}\mathrm{Re}\int_a^b \left\{2\left|B_1 h_1^{(1)}(\kappa_p r) + B_2 h_1^{(2)}(\kappa_p r)\right|^2 + \left|B_1\Gamma_1(\kappa_p r) + B_2\Gamma_2(\kappa_p r)\right|^2\right\}dr \quad (4.27a)$$

$$W_m^p(r,\omega)|_{p=1} = \frac{G_m}{2|Z_p|^2} \quad \mathrm{Re}\int_a^b \left|B_1 h_1^{(1)}(\kappa_p r) + B_2 h_1^{(2)}(\kappa_p r)\right|^2 r^2 dr. \quad (4.27b)$$

The integrals in (4.27) can be numerically solved utilizing Lummel's equations defined in section 2.2.1.

Following the same procedure for $r > b$ by substituting (4.10) in (4.25) with $G_e = (\omega\varepsilon_2(\omega))'$ and $G_m = (\omega\mu_2(\omega))'$, the radial integrations of the stored electric and magnetic energies in the outer sphere are calculated as

$$W_e^p(r,\omega)|_{p=2} = \frac{G_e}{2|\kappa_p|^2}\mathrm{Re}\int_b^\infty \left\{2\left|B_3 h_1^{(2)}(\kappa_p r)\right|^2 + \left|B_3\Gamma_2(\kappa_p r)\right|^2\right\}dr \quad (4.28a)$$

$$W_m^p(r,\omega)|_{p=2} = \frac{G_m}{2|Z_p|^2} \quad \mathrm{Re}\int_b^\infty \left|B_3 h_1^{(2)}(\kappa_p r)\right|^2 r^2 dr. \quad (4.28b)$$

The objective is to find the optimum matching between the electrically small antenna enclosed in the minimum sphere and the lossy material (which will be replaced later by bio-tissues) in the outermost sphere $r > b$. We assume that the outermost sphere contains an isotropic, homogeneous, and lossy material with known permittivity and permeability, while the middle sphere has radii and values of unknown permittivity and permeability, which we wish to calculate. First, the problem is investigated at a single frequency ($f_0 = 1$ GHz) with single values of the relative permittivity and will be later expanded to a broader frequency range. Therefore, a single arbitrary value for the complex relative permittivity of the dielectric material in the outer sphere at the same frequency is considered to be $\varepsilon_2 = 14 - j3$. Next, by compensating for the stored electric and the magnetic energies as suggested in section 4.3, the optimum values of the relative permittivity and permeability of the material in the middle sphere can be numerically calculated using the previously derived equations of the stored electromagnetic energies in (4.24)-(4.28).

The ratio between the stored electric and magnetic energies in the middle and outer spheres are evaluated by substituting (4.27) and (4.28) into (4.17). Figure 4.4a depicts the ratio of the stored energies as a function of the relative permittivity of the middle sphere at different values of the outer radius $b = 40$, 45, 60 mm. As observed, the stored electric energy predominates for small relative permittivity values. As the permittivity increases

while keeping $\mu_r = 1$, the stored magnetic energy increases until it approaches the value of the stored electric energy, and the first resonance is reached. After that, the stored electric energy predominates again as the relative permittivity increases. At higher permittivity values, while keeping the outer radius b unchanged, higher resonances are reached, i.e., the compensation between the stored electric and magnetic energies in the middle and outer spheres are achieved at different values of the relative permittivity. Furthermore, the thickness of the middle layer affects the resonance at which the stored electric and magnetic energies are equal, i.e., as the outer radius b increases while keeping the inner radius a unchanged, an energy compensation occurs at lower permittivity values.

Matching an electrically small antenna to a lossy dielectric medium can be achieved by placing a dielectric material with a relatively high permittivity value between the antenna element and the lossy medium. In contrast to permittivity, the stored electromagnetic energy in the middle sphere does not compensate for the stored electromagnetic energy in the outer sphere by changing the value of the relative permeability of the material in the middle sphere, as is clearly shown in Fig. 4.4b. It is evident that the stored electric energy predominates over a wide range of the permeability values regardless of the change in the thickness of the middle sphere, i.e., no resonance is reached.

Although utilizing a dielectric material with high permittivity values enhances the matching between the ESA and the surrounding lossy medium, the operating frequency bandwidth is still a challenging issue for electrically small antennas. Therefore, we reinvestigate the same problem over a broader frequency range, for instance, $0.6 < f < 2$ GHz. The material in the outer sphere ($r > b$) is assumed to have the same complex permittivity value of $\varepsilon_2 = 14 - j3$, while the permittivity value of the dielectric material in the middle sphere is chosen from the broken black curve shown in Fig. 4.4a, at which the first resonance occurs, i.e., $\varepsilon_1 = 52$. The inner radius is kept at $a = 5$ mm, while the outer radius is changeable with values of $b = 25, 45, 60$ mm.

Figure 4.5 shows the stored electric and magnetic energies as a function of both sphere radius and operating frequency. It is obvious that the thickness of the middle sphere affects the internally stored energies. Since the outer radius is $b = 25$ mm, the electric energy stored in the middle sphere approaches the energy stored in the outer sphere at a lower frequency value with imperfect matching as expected from the energy ratio shown in Fig. 4.4 a (green curve), where the stored electric and magnetic energies are not exactly equal at the first resonance. However, as the thickness increases $b = 45$ and $b = 60$ mm, a better matching at different frequencies occurs, i.e., as the thickness of the middle sphere increases while keeping the permittivity values in the middle and outer sphere unchanged, the stored electric energy increases enough to compensate for the stored energy in the outer sphere. However, as the frequency increases, energy compensation is accomplished over narrow frequency bandwidths, unlike for lower frequencies, where better energy compensation is accomplished. For instance, in Fig. 4.5b, with an outer radius $b = 45$ mm, barely 150 MHz of an operating bandwidth is reached around the resonance wavelength of 350 mm.

The outwardly radiated power by the electrically small antenna in the three-layered sphere as a function of the sphere radius and frequency is depicted in Fig. 4.6. The results of the radiated power are calculated using (4.16a) and the spherical multipole expansion of

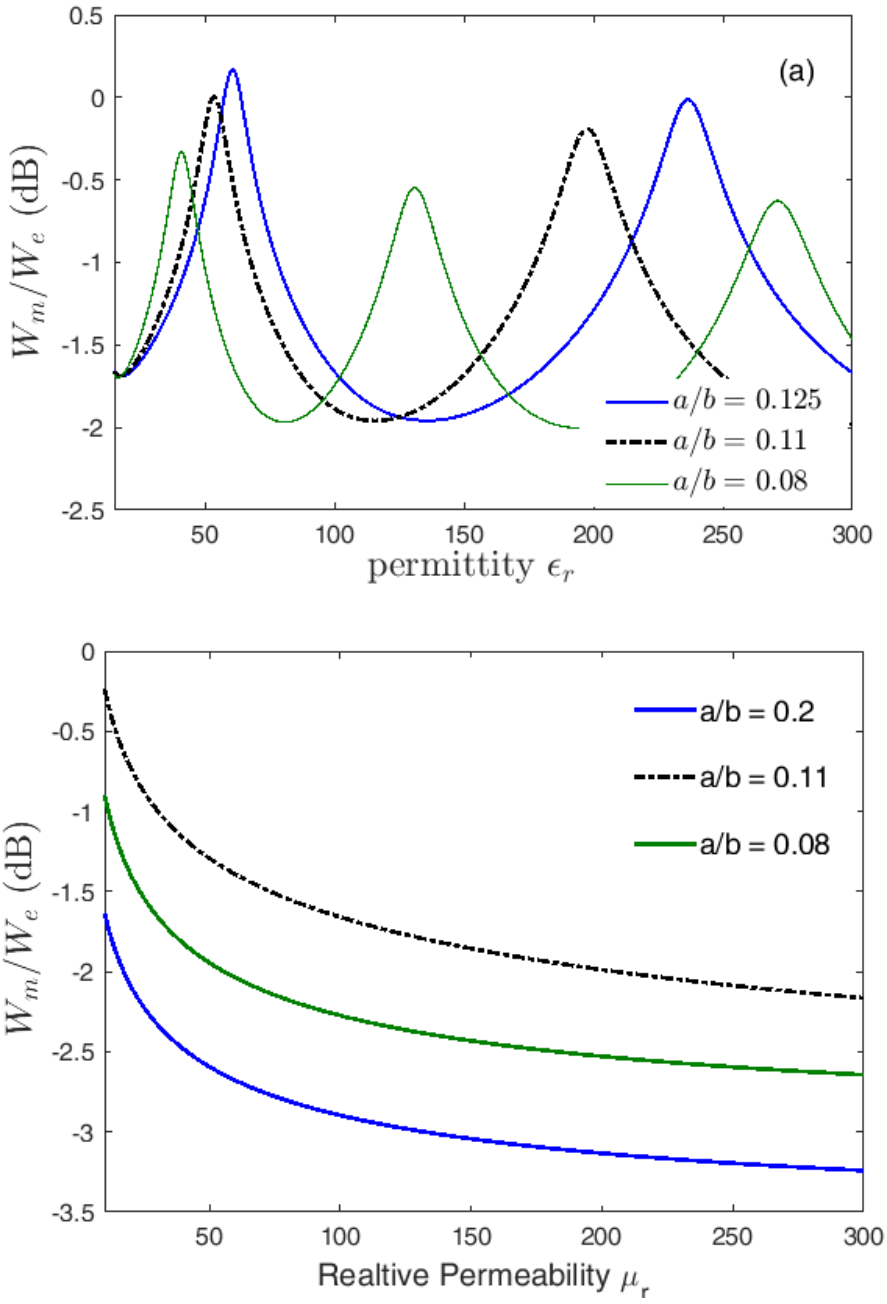

Figure 4.4: Manifestation of the ratio between the stored electric and magnetic energies of the electrically small antenna at $f_0 = 1$ GHz at different values of the outer radius of the middle sphere and as a function of the real part of (**a**) the relative permittivity and (**b**) the relative permeability of the middle sphere.

the electric and magnetic fields in the three-layered sphere derived in (4.12)-(4.15). The results show the robustness of the proposed method by placing a dielectric material between the antenna element and the surrounding lossy medium where the optimum matching is accomplished.

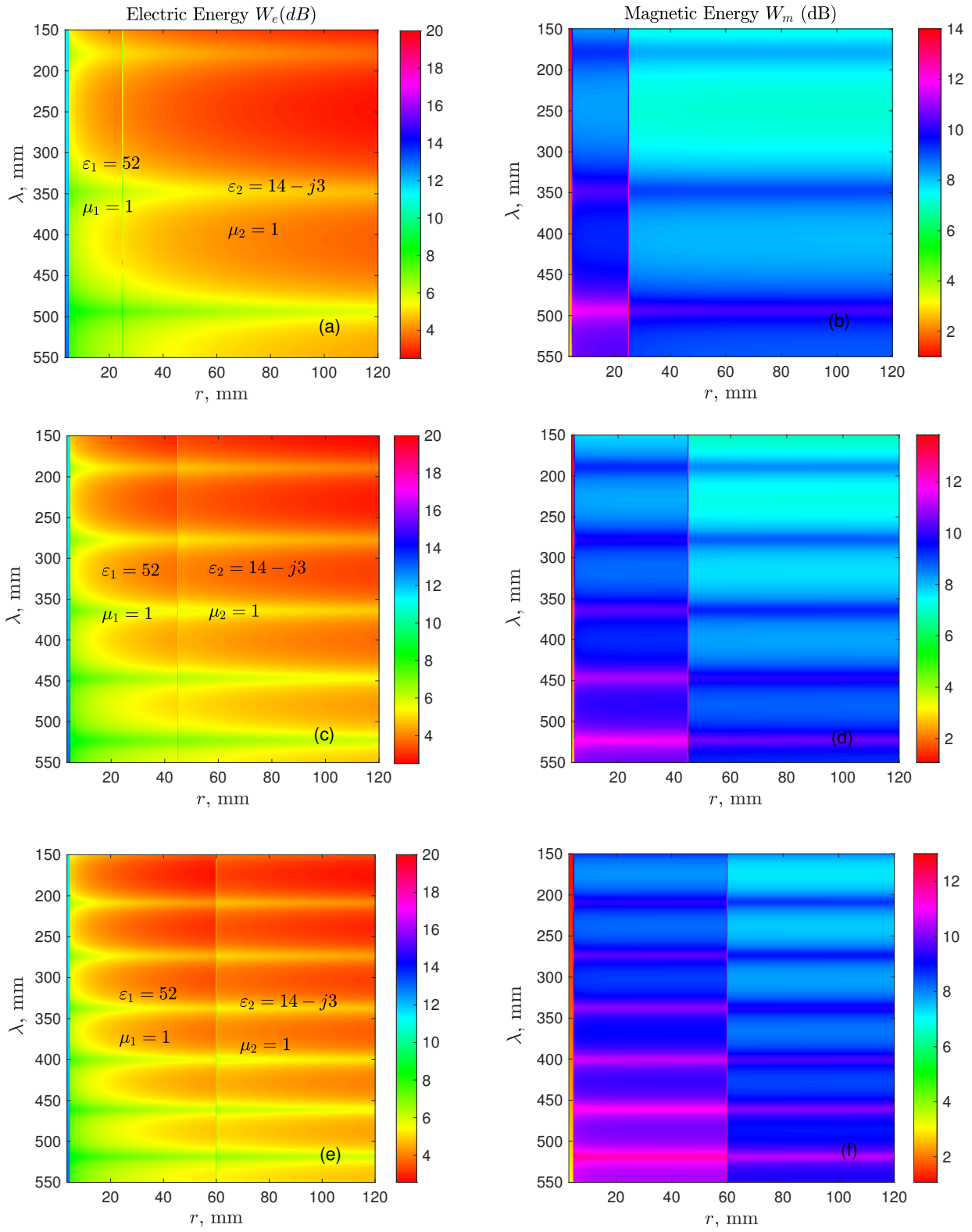

Figure 4.5: A 2-D illustration of the stored electric and magnetic energies as a function of frequency and outer radius. The relative permittivities of the middle and outer spheres are kept at $\varepsilon_1 = 52$ and $\varepsilon_2 = 14 - j3$, and the inner radius $a = 5$ mm, while (**a,b**) $b = 25$ mm (**c,d**) $b = 45$ mm (**e,f**) $b = 60$ mm.

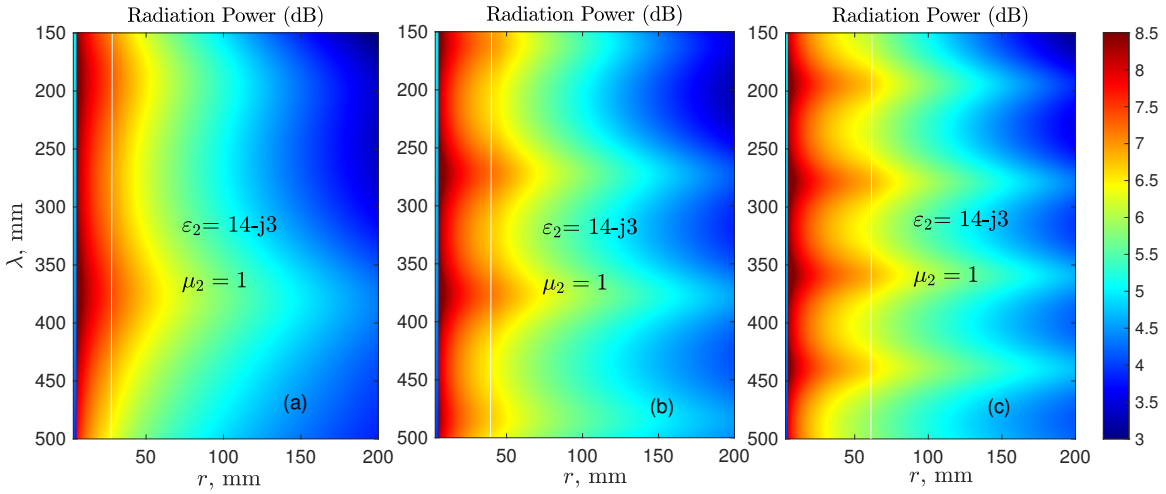

Figure 4.6: A 2-D illustration of the outwardly radiated power of the electric dipole antenna as a function of sphere radius and operating frequency. The relative permittivity of the middle sphere is kept at $\varepsilon_1 = 52$ and the inner radius is $a = 5$ mm, while (**a**) $b = 25$ mm (**b**) $b = 45$ mm (**c**) $b = 60$ mm.

4.4 Realization of Electrically Small Antennas in Biomedical Applications

Due to the drastically reduced size of electrically small antennas, they exhibit a very low radiation efficiency, narrow bandwidth, and a poor matching, particularly in contact with lossy media. In biomedical applications, where antennas are utilized to transmit electromagnetic energies in the human body like in radiation therapies [66] [67], direct contact between the antenna element and the human body is preferred. However, drastic reflections of the radiated electromagnetic fields are unavoidable for highly dispersive biological tissues, which leads to a poor matching between the antenna element and the bio-tissues [23], [68]. The following section investigates the realization of electrically small antennas in biomedical applications.

4.4.1 Infinitesimally Electric Dipole Antenna

In the previous sections, we utilized a dielectric material with a relatively high permittivity value at a single frequency to improve the power radiated by the electrically small antenna into the surrounding lossy medium. However, the method was investigated at a single permittivity value, i.e., assumed no dispersion in the permittivity or permeability of the materials in the middle and outer spheres. Therefore, by substituting the material in the outermost sphere with a highly dispersive material, the stored electromagnetic energies in (4.27) and (4.28) and the radiated power by the electrically small antenna should be recalculated to account for the permittivity dispersion.

Firstly, we assume that the material in the outermost sphere is replaced with biological tissues, while the material in the middle sphere has unknown values of permittivity, which we desire to evaluate. Therefore, the following procedure is pursued to find the optimum

matching between the electrically small antenna enclosed in the minimum sphere and the biological tissues in the outer sphere:

i. The breast fat tissue, with the measured frequency-dependent permittivity values $\varepsilon_2(\omega)$ taken from [68] as shown in Fig. 4.7a, is considered to represent the biological tissues in the outer sphere.

ii. The electric and magnetic energies stored in the middle and outer spheres are computed using (4.22)-(4.28) over a frequency range $0.6 \leq f \leq 1.8$ GHz.

iii. The complex permittivity values $\varepsilon_1(\omega)$ (real part) of the dielectric material in the middle sphere are numerically computed by compensating for the internally stored energies in the middle and outer spheres using (4.17) over the same frequency range in (ii).

iv. The Kramers-Kronig relations are applied to calculate the imaginary part from the real part of the complex permittivity values obtained in (iii) of the dielectric material in the middle sphere.

Due to the frequency dispersion of the permittivity of the biological tissues, the functions G_e and G_m in (4.22)-(4.28) are frequency-dependent and should account for the frequency derivatives of the dispersive permittivity and permeability.

Figure 4.7b (the red curve) shows the computed values of the real part of the complex permittivity $\varepsilon_1(\omega)$ of the dielectric material in the middle sphere using the derived equations (4.17)-(4.28). Since the real part of the complex permittivity $\varepsilon_1(\omega)$ is dispersive over a wide band of frequencies, the imaginary part must also be dispersive over the same frequency range. As a consequence, the Kramers-Kronig transformations are applied to calculate the imaginary part of the complex permittivity $\varepsilon_1(\omega)$ using the calculated real part (red curve) shown in Fig. 4.7b. Figure 4.7c manifests the calculated values of the imaginary part of $\varepsilon_1(\omega)$. The Kramers-Kronig transformations are then inversely applied to recalculate the real part (blue curve shown in Fig. 4.7b) to check for the consistency between the KK-transformed real and imaginary parts of $\varepsilon_1(\omega)$. A good match between the calculated values of the real part of $\varepsilon_1(\omega)$, referred to as initial values, and its KK-transformed values is depicted in Fig. 4.7b.

The radiated power by the electrically small antenna as a function of both sphere radius and operating frequency is depicted in Fig. 4.8. It is obvious that the matching between the ESA and the biological tissues is accomplished over a wide range of frequencies by placing a dielectric material with highly dispersive permittivity values between the antenna element and the bio-tissues. Subsequently, enclosing the infinitesimally electric dipole antenna with a dispersive dielectric material increases its operating frequency bandwidth and enhances its matching to surrounding lossy/dispersive media.

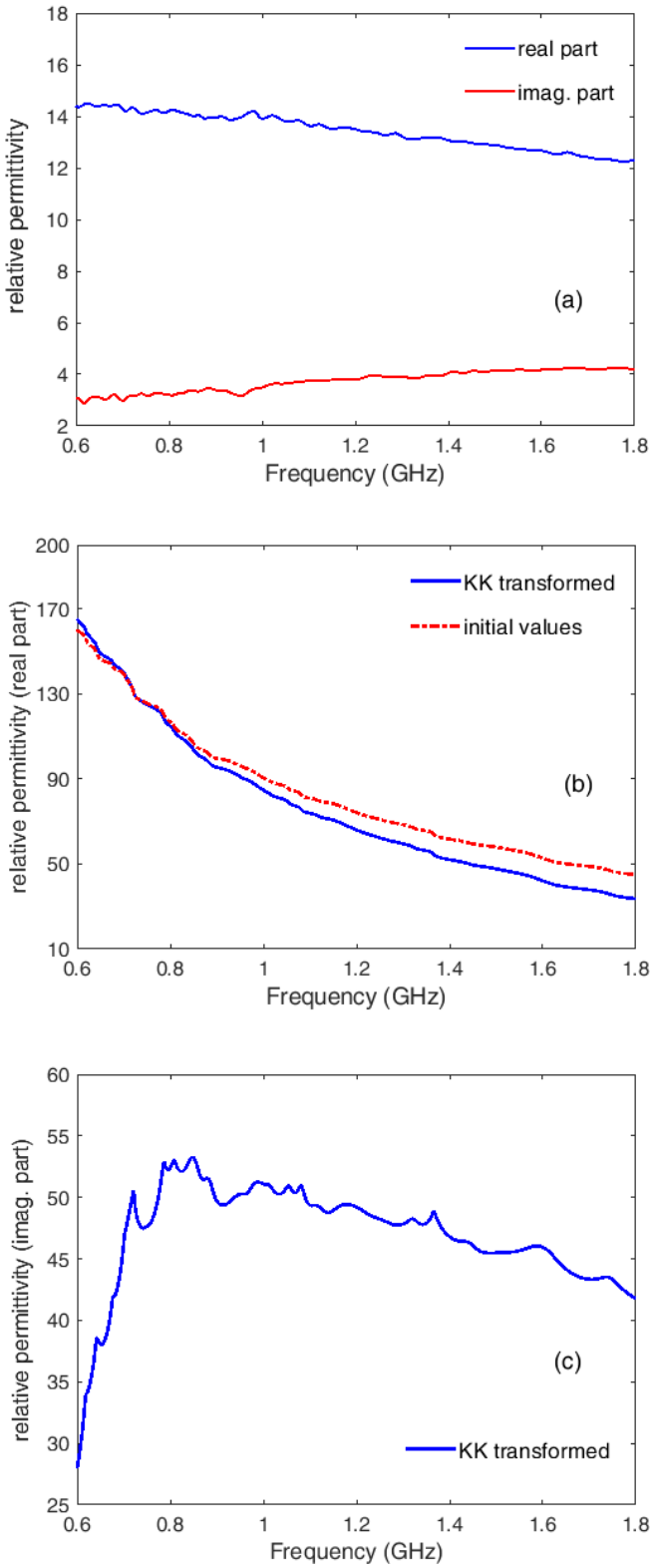

Figure 4.7: The complex values of $\varepsilon_1(\omega)$ and $\varepsilon_2(\omega)$, (**a**) the measured data of the complex permittivity $\varepsilon_2(\omega)$ of the breast fat tissue [68], (**b**) the real part of $\varepsilon_1(\omega)$ (red curve) obtained by (4.22)-(4.28) and its KK transformed values (blue curve) obtained from the imaginary part in Fig. 4.7c, (**c**) the imaginary part of $\varepsilon_1(\omega)$ obtained from the real part (red curve) in Fig. 4.7b using the KK transformations.

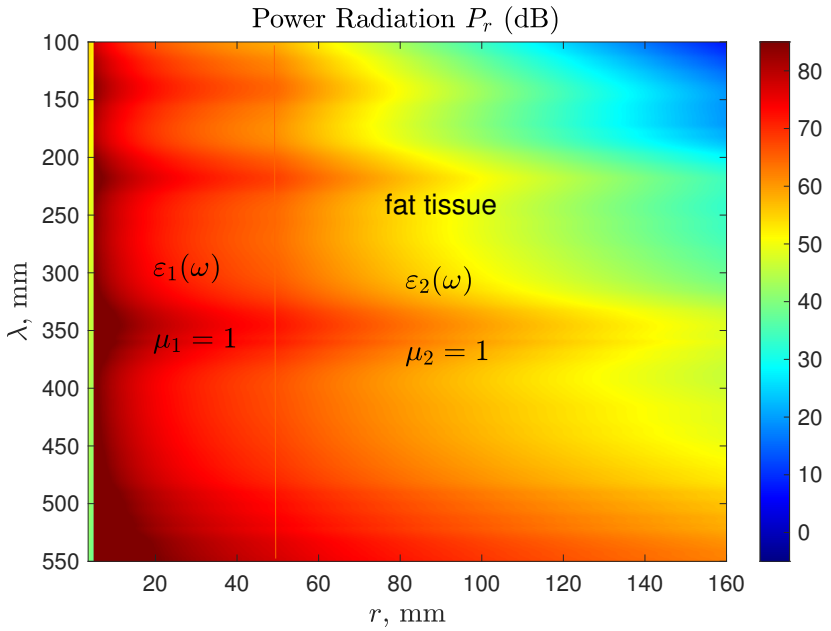

Figure 4.8: A 2-D illustration of the radiated power of the electrically small antenna immersed in a highly dispersive medium (referred to the breast fat tissue).

4.5 Spherical Multipole Expansion of Electrically Small Magnetic Antennas

By replacing the infinitesimally electric dipole in Fig. 4.1 with an infinitesimally magnetic dipole, and assuming the exact geometrical dimensions, only a TE_{10} mode exists in the three-layered sphere. The electric and magnetic fields in the inner sphere ($r < a$) are represented according to [61, Ch. 5], while outside the inner sphere ($r > a$), the electromagnetic fields are represented with the vectorial spherical multipole expansion [28]. Using the duality theorem [28], the TE mode can be exchanged with a TM mode, i.e., the electric and magnetic fields radiated by an infinitesimally electric dipole are dual to the magnetic and electric fields radiated by the infinitesimally magnetic dipole. Consequently, using the duality theorem, the radiated electromagnetic fields of the TE_{10} mode are related to the electromagnetic fields of the TM_{10} in the three-layered sphere using (4.7)-(4.10) as

$$H_r^p(r,\omega)|_{p=0} = \frac{I_h}{I_o}\frac{E_r^p(r,\omega)}{Z_0^2} \tag{4.29a}$$

$$H_\vartheta^p(r,\omega)|_{p=0} = \frac{I_h}{I_o}\frac{E_\vartheta^p(r,\omega)}{Z_0^2} \tag{4.29b}$$

$$E_\varphi^p(r,\omega)|_{p=0} = -\frac{I_h}{I_o}H_\varphi^p(r,\omega). \tag{4.29c}$$

For $r < a$, while for $a < r < b$ and $r > b$, the electric and magnetic fields are written as

$$H_r^p(r,\omega)|_{p=1,2} = \frac{b_{10}}{a_{10}} E_r^p(r,\omega) \tag{4.30a}$$

$$H_\vartheta^p(r,\omega)|_{p=1,2} = \frac{b_{10}}{a_{10}} E_\vartheta^p(r,\omega) \tag{4.30b}$$

$$E_\varphi^p(r,\omega)|_{p=1,2} = \frac{b_{10}}{a_{10}} Z_p^2 H_\varphi^p(r,\omega), \tag{4.30c}$$

where I_h is the magnetic excitation current, $m = 1$ and $n = 0$ for the TE_{10} mode, and $p = 0, 1, 2$ indicates the sphere layer-order. Likewise, the stored electric and magnetic energies in the TE_{10} mode of the infinitesimally magnetic dipole in the three-layered sphere are related to the stored electromagnetic energies of the TM_{10} mode of the infinitesimally electric dipole as

$$W_m^p(r,\omega)|_{p=1,2} = Re\left(\frac{\mu_p}{\varepsilon_p}\right)\left|\frac{b_{10}}{a_{10}}\right|^2 W_e^p(r,\omega) \tag{4.31a}$$

$$W_e^p(r,\omega)|_{p=1,2} = Re\left(\frac{\varepsilon_p}{\mu_p}\right)\left|\frac{b_{10}}{a_{10}}\right|^2 |Z_p|^4 W_m^p(r,\omega). \tag{4.31b}$$

We assume that the medium in the minimum sphere ($r < a$) enclosing the infinitesimally magnetic dipole is lossless, while the medium in the outermost sphere is lossy with known permittivity and permeability. The same previous procedure is followed to calculate the optimum values of the relative permittivity and permeability of the material in the middle sphere. The derived equations (4.29) to (4.31) are utilized to compute the stored electric and magnetic energies of the infinitesimally magnetic dipole in the three-layered sphere. By compensating for the stored energies in the middle and outer spheres, the permittivity and permeability values of the material in the middle sphere are calculated. Figure 4.9 shows the ratio between the stored magnetic and electric energies of the infinitesimally magnetic dipole enclosed in the three-layered sphere for $I_h = 1$, $a = 5$ mm, and the outer radius is chosen to be $b = 30, 40, 47.5$ mm. The operating frequency is kept at $f_0 = 1$ GHz, while the lossy material in the outer sphere is assumed to have a complex permittivity as $\varepsilon_2 = 14 - j3$.

It is evident in Fig. 4.9 that the stored magnetic energy predominates for low relative permittivity values and then decreases gradually as the permittivity increases. While the relative permittivity ε_1 still increases, the stored electric energy increases until it approaches the stored magnetic energy and the first resonance appears. In contrast to the infinitesimally electric dipole antenna, where the stored electric energy is predominant, the stored magnetic energy predominates for the infinitesimally magnetic dipole antenna. Placing a dielectric material with high permittivity values between the antenna element and the lossy material in the outer sphere increases the electric energy stored in the middle sphere enough to compensate for the magnetic energy stored in the outer sphere. In other words, the infinitesimally magnetic dipole antenna is matched with lossy media using dielectric material with high permittivity values.

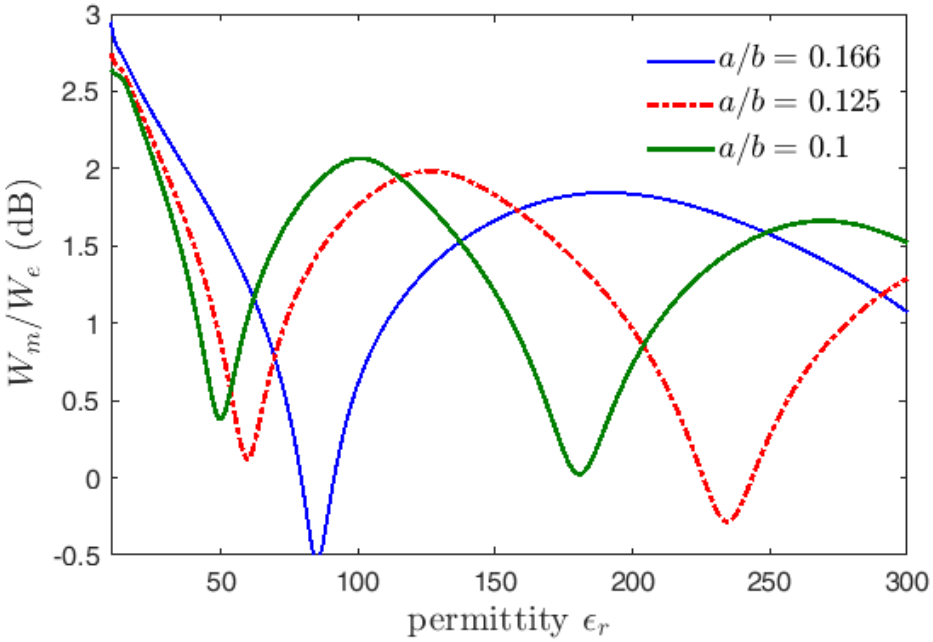

Figure 4.9: The ratio between the stored magnetic and electric energies of the infinitesimally magnetic dipole enclosed in the three-layered sphere.

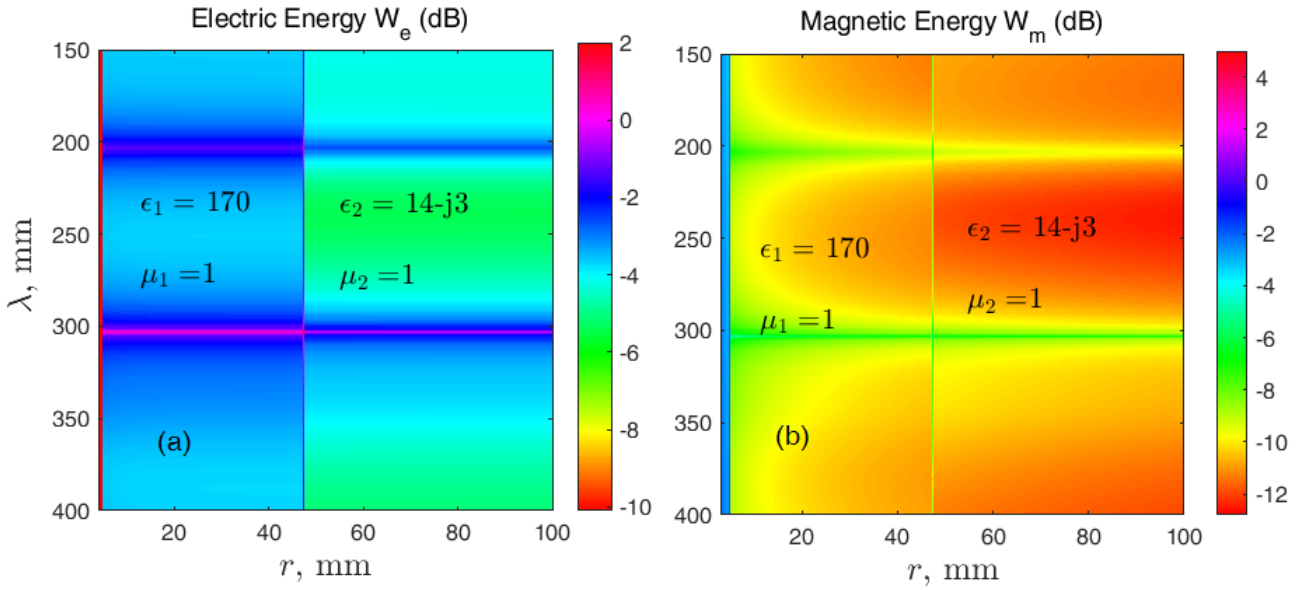

Figure 4.10: A 2-D illustration of the stored electric and magnetic energies of the infinitesimally magnetic dipole as a function of both sphere radius and operating frequency. The outer radius is selected to be $b = 30$ and 47.5 mm.

We assume the permittivity of the material in the outer sphere is maintained to be $\varepsilon_2 = 14 - j3$. In contrast, the relative permittivity value of the material in the middle sphere is chosen from the green curve at which the second resonance occurs, i.e., at $\varepsilon_1 = 170$ as shown in Fig. 4.9. By utilizing the derived formulas in (4.29)-(4.31), the stored

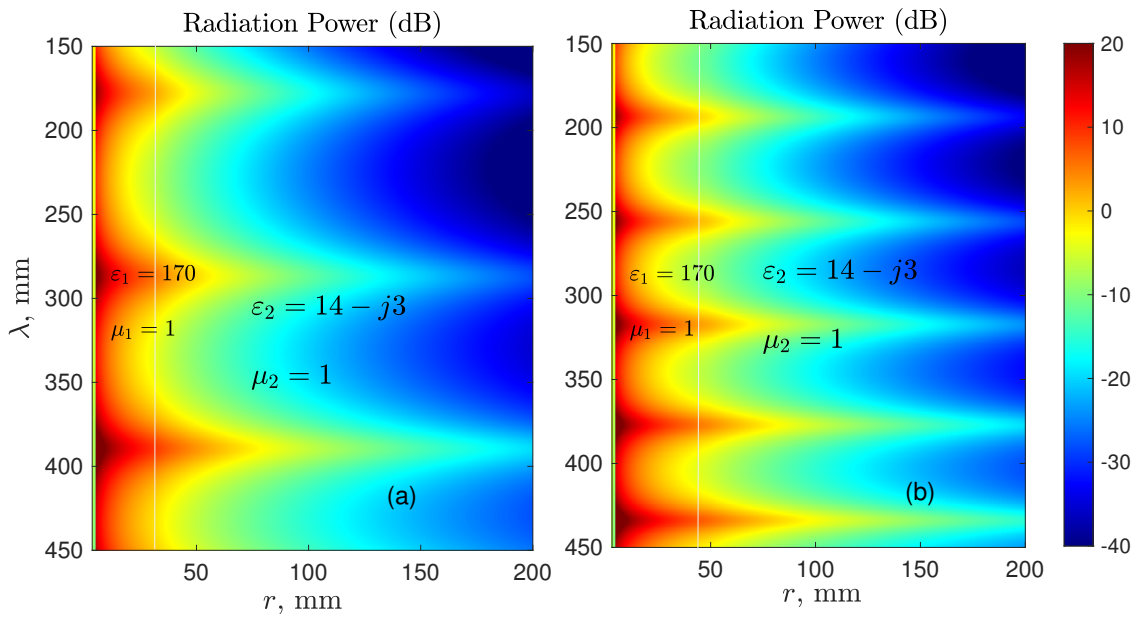

Figure 4.11: A 2-D illustration of the radiated power of the infinitesimally magnetic dipole element enclosed by a lossy medium. The outer radius is selected to be $b = 30$ and 47.5 mm, while the permittivity of the material contained in the middle sphere is $\varepsilon_1 = 170$.

electromagnetic energies of the infinitesimally magnetic dipole are calculated as a function of both the sphere radius and operating frequency, as shown in Fig. 4.10. The radiated power by the magnetic dipole is depicted in Fig. 4.11. The results demonstrate that the power matching between the infinitesimally magnetic dipole and the surrounding lossy medium is enhanced using a dielectric material.

In conclusion, the infinitesimally electric or magnetic dipole antennas are matched to a lossy or dispersive medium like biological tissues using a dielectric material with high permittivity values. The antenna element is assumed to be enclosed in a three-layered sphere, where the material in the outermost sphere is lossy. The spherical multipole expansion method is utilized to represent the electromagnetic fields radiated by the electrically small antenna element. The optimal values of the material's relative permittivity in the middle sphere, at which the matching occurs, are calculated by compensating for the stored electric and magnetic energies in the middle and outer spheres. However, the optimum matching is accomplished over a narrow frequency bandwidth when the material in the middle sphere has non-dispersive permittivity values. In contrast, using a dielectric material with a highly dispersive permittivity, the stored electromagnetic energies are compensated over a broader frequency bandwidth, and more power is transferred into the surrounding dispersive medium.

5. Effect Of Dispersive Magnetic Materials on the Performance of Electrically Small Antennas

This chapter investigates the effect of dispersive magnetic materials on the performance of electrically small antennas. Generally, miniaturizing the electrical size of any antenna degrades its performance due to the drastic increase in the reactive energy compared to the radiated energy, which reduces the radiation resistance and narrows the operating bandwidth. In contrast, reducing the stored electric and magnetic energies increases the radiation resistance and decreases the quality factor (Q-factor), which increases the operating bandwidth of electrically small antennas. Chu [69] derived an equation for the lower bounds of the Q-factor of a general and lossless omnidirectional antenna as shown in (5.1) by assuming no stored energy inside the minimum imaginary sphere enclosing the antenna except of that energy required to make the antenna tunable

$$Q_{\text{chu}} \cong e_c \frac{1}{(\kappa r)^3}. \tag{5.1}$$

Here κ and r are the wavenumber and the radius of the minimum sphere enclosing the antenna element, while the radiation efficiency e_c represents the losses. Many techniques have been proposed and investigated for reducing the Q-factor of electrically small antennas [70] [71]. In a brilliant work of Yaghjian [13], the role of the reactive energy of an electrically small antenna containing a dispersive material was discussed, where the lower bounds in (5.1) are halved using tuning elements consisting of highly dispersive dielectric or magnetic materials. However, the high reduction in the Q-factor was at the expense of reducing the radiation efficiency. Stuart [72] showed that enclosing the electrically small antenna with a high-permeability magnetic material can eliminate the stored electromagnetic energy, resulting in a Q-factor value close to Q_{chu}.

The following sections investigate the performance of a particular type of electrically small antennas, the top-loaded monopole antenna (also referred to as disk monopole) shown in Fig. 5.1 by coating the antenna element with a highly dispersive magnetic material [72]. The magnetic energy stored in the dispersive magnetic material compensates for the stored electric energy underneath the upper disk over a broad frequency range, increasing the operating bandwidth. In this work, the permeability values of the dispersive magnetic material coating the antenna are assumed unknown. After that, we mathematically calculate these values that lead to the optimum performance of the disk monopole antenna. The analysis is performed using the equations (4.19)-(4.22) of the stored electromagnetic energies in dispersive materials derived in the previous chapter and verified using the full-wave electromagnetic simulator

CST©. Due to the dispersion in the magnetic material, the Kramers-Kronig transformations are applied to interrelate the real and the imaginary parts of the frequency-dependent permeability values.

5.1 Top-Loaded Monopole Antenna

It was found in the literature [72] [73], that the stored electric energy of the top-loaded monopole antenna shown in Fig. 5.1 increases due to the capacitive loading of the upper disk, which in turn degrades its performance. According to Stuart [72], enclosing this antenna with a magnetic shell can eliminate the internally stored energy, resulting in decreasing the Q-factor to values close to the Chu Q-factor in (5.1). We further investigate this method by enclosing the antenna with a dispersive magnetic material as shown in Fig. 5.1b. However, we aim to get compensation between the stored electric energy under the upper disk and the stored magnetic energy in the dispersive magnetic material over a broad frequency range. The compensation for the stored electromagnetic energies assists in increasing the input impedance of the top-loaded monopole antenna over a broader frequency range and increases its operating bandwidth. In the following sections, the stored electric and magnetic energies, resonant modes, radiation efficiency, and the gain of the top-loaded monopole antenna will be mathematically and numerically analyzed in terms of the antenna geometrical dimensions.

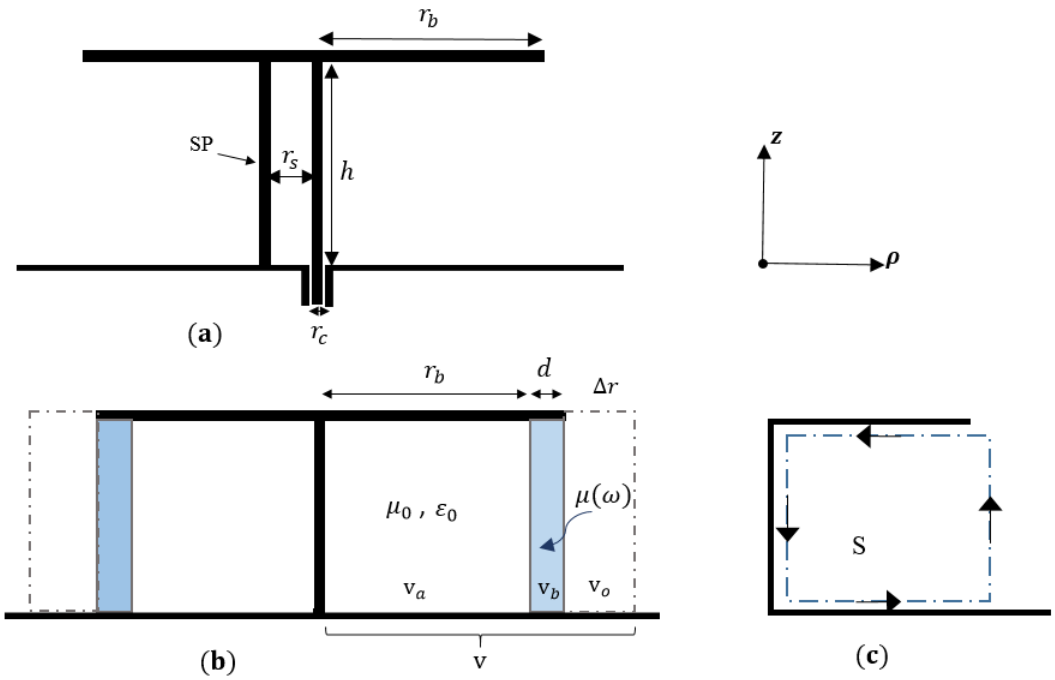

Figure 5.1: A Cross-sectional view of the top-loaded monopole antenna (**a**) without a magnetic material and (**b**) with a magnetic material enclosing the disk monopole antenna. The shorting post (SP) is removed in (**b**) due to the existence of the magnetic material as will be discussed later. (**c**) Illustration of the closed contour for Faraday's law.

5.2 Magnetic Material Effect on the Resonant Frequency

Figure 5.1a shows an electric monopole antenna consisting of a straight conducting wire of a height h and top-loaded with a conducting circular disk of radius r_b. The antenna is assumed concentric at the origin of the cylindrical coordinates (ρ, φ, z) with its center conductor placed parallel to the z-axis and the radial length in the ρ-direction. The disk radius and the height of the conducting wire are selected to be much smaller than the operating wavelength, i.e., $r_b, h \ll \lambda$. A coaxial transmission line, with a characteristic impedance of 50 Ω, is utilized to feed the antenna at the base of the center conductor. The upper disk is shorted to the ground plane by a conducting wire (shorting post) placed at a distance r_s from the center conductor and has the same height h.

For the geometrical dimensions $h = 40$ mm, $r_b = 50$ mm, $r_c = 2.1$ mm, $t = 0.7$ mm (these dimensions are considered and fixed for all the obtained results in this chapter) with no shorting wire and no dielectric or magnetic material present under the upper disk, the full-wave simulator gives a fundamental resonant frequency at 404.5 MHz. When the upper disk is shorted to ground at a distance $r_s = 7$ mm from the center conductor, the fundamental resonant frequency is 437 MHz.

The full-wave simulator produces both the electric field distribution and the input impedance of the fundamental resonant frequency of the shorted and non-shorted disk monopole antenna, as shown in Fig. 5.2. It is obvious that the electric field of the fundamental resonant frequency is uniformly polarized in the z-direction and parallel to the height of the center conductor while it slightly deviates in the radial direction near the edges of the upper disk. Consequently, the fundamental mode is clearly transverse magnetic (TM_z) with electric field components $\vec{E} = E_z\hat{z} + E_\rho\hat{\rho}$ and a magnetic field $\vec{H} = H_\varphi\hat{\varphi}$. Following the analysis of Stuart [72] the radial component of the electric field E_ρ vanishes directly under the upper disk when the antenna structure is enclosed with a magnetic shell, and thus the radial component E_ρ will not be considered for the calculations. In the case of connecting the upper disk to the antenna ground, the mutual coupling induced between the shorting wire and the center conductor assists in polarizing a part of the electric field vectors in the radial direction around the center conductor [73]. This change in the electric field vectors under the upper disk adds some additional resonances, which increases the antenna input resistance and hence shifts the resonant frequency to higher values. The latter is clearly shown in Fig. 5.2a, where additional resonances appear by shorting the antenna to the ground, unlike the non-shorted disk monopole antenna.

From the electric field distribution in Fig. 5.2b, it is clear that the stored electric energy under the upper disk is predominant for fundamental resonant mode. Stuart *et al.* [72] eliminated the stored electric energy in the cylindrical volume under the upper disk by enclosing the monopole antenna with a magnetic material of high permeability value. We follow the same procedure by coating the monopole antenna with a highly dispersive magnetic material [25]. However, we aim to investigate the effect of the dispersive magnetic material on the performance of the top-loaded monopole antenna. The resonant modes and the operating frequency bandwidth are calculated by compensating for the stored electric and magnetic energies under the upper disk. The dispersion in the permeability of the magnetic material can be utilized to achieve a relatively broad compensation between the stored electromagnetic

energies and hence increases the antenna's operating bandwidth.

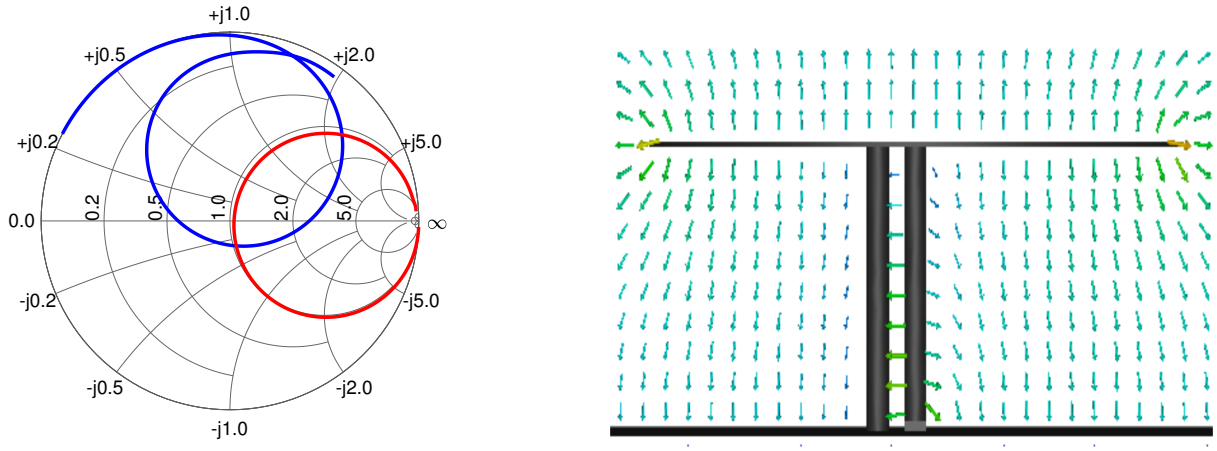

(a) **(b)**

Figure 5.2: **(a)** The input impedances of the non-shorted (red curve) and shorted (blue curve) disk monopole antenna. **(b)** The electric field distribution of the fundamental mode of the shorted disk monopole antenna at $f_0 = 437$ MHz.

5.2.1 Complete Filling with Non-dispersive Magnetic Material

This section analytically investigates the effect of magnetic materials on the resonant modes of the top-loaded monopole antenna. Firstly, we assume the whole cylindrical volume under the upper disk is filled with a non-dispersive magnetic material, i.e., the volume v_b, which contains the magnetic material as shown in Fig. 5.1b extends to the center conductor. By exciting the monopole antenna at the base of the center conductor with an input electric current $\mathrm{I}_e(\omega)$, the magnetic field under the upper disk can be derived in terms of the input current according to Ampères law as

$$H_\varphi(\omega, \rho) = \frac{I_e(\omega)}{2\pi\rho}, \tag{5.2}$$

while the electric field can be found by applying Faraday's law on the closed contour shown in Fig. 5.1

$$\oint_{C(S)} \vec{E} \cdot \mathrm{d}\vec{L} = -j\omega \iint_S \mu \vec{H} \cdot \mathrm{d}\vec{S} \tag{5.3a}$$

$$E_z(\omega, \rho) = -j\omega\mu_0\mu_r \frac{I_e(\omega)}{2\pi} \ln\left(\frac{\rho}{r_c}\right), \tag{5.3b}$$

where μ_r is the relative permeability of the magnetic material, while the permittivity is considered to be that of free space $\varepsilon = \varepsilon_0$. The complex input power of the antenna is

calculated in terms of its input impedance $Z_{in}(\omega) = R_{in}(\omega) + jX_{in}(\omega)$ [74] as

$$\begin{aligned} P_{in}(\omega) &= \frac{1}{2}|I_e(\omega)|^2 Z_{in}(\omega) \\ &= \frac{1}{2}|I_e(\omega)|^2 \left(R_{in}(\omega) + jX_{in}(\omega)\right) \\ &= P_{acc}(\omega) + j2\omega(W_m(\omega) - W_e(\omega)). \end{aligned} \tag{5.4}$$

Here, P_{acc} is the time-averaged power accepted by the antenna which is purely real and related to the input resistance R_{in}, while W_e and W_m are the stored electric and magnetic energies and represent the reactive power. Since the antenna is tuned at $\omega = \omega_0$, its input impedance is purely real, i.e. the imaginary part $X_{in}(\omega_0) = 0$. Consequently, the stored electric and magnetic energies are equal $W_{\mathrm{m}}(\omega_0) = W_{\mathrm{e}}(\omega_0)$. Substituting the magnetic and electric fields of (5.2) and (5.3) into (4.21) and compensating for the stored electric and magnetic energies, we get

$$\begin{aligned} W_m(\omega_0) &= W_e(\omega_0) \\ \underbrace{\iiint_{\mathrm{v}} \left(\frac{I_e(\omega)}{2\pi\rho}\right)^2 \mathrm{d}v}_{=\tilde{L}} &= \omega_0^2 \mu_r \underbrace{\iiint_{\mathrm{v}} \varepsilon_0\mu_0 \left(\frac{I_e(\omega)}{2\pi} \ln\left(\frac{\rho}{r_c}\right)\right)^2 \mathrm{d}v}_{=\tilde{C}}, \end{aligned} \tag{5.5}$$

and the resonant frequency of the top-loaded monopole antenna is obtained from (5.5) as

$$\omega_0 = \sqrt{\frac{\tilde{L}}{\mu_r \tilde{C}}}. \tag{5.6}$$

The validity of (5.6) is tested by comparing its output with that obtained by the frequency-domain solver CST© for the same geometrical dimensions considered above in Section 5.2. For a relative permeability $\mu_r = 8$, equation (5.6) gives a resonant frequency $f_0 = 312$ MHz while the frequency-domain solver gives 304 MHz. The difference between the obtained values is due to neglecting the radial component of the electric field, as suggested above in Section 5.2.

5.2.2 Partial Filling with Non-dispersive Magnetic Material

If the volume under the upper disk is partially filled with a magnetic material, equation (5.6) is no longer valid. By assuming the space in the cylindrical volumes v_a and v_0 is vacuum with $\varepsilon = \varepsilon_0$ and $\mu = \mu_0$ as shown in Fig. 5.1, while the volume v_b is filled with a non-dispersive magnetic material, equation (5.5) can be recast as

$$\begin{aligned} \mu_r\mu_0 \underbrace{\iiint_{\mathrm{v}} \left(\frac{I_e(\omega)}{2\pi\rho}\right)^2 \mathrm{d}v}_{=\tilde{L}} &= \omega_0^2\mu_r^2 \underbrace{\iiint_{\mathrm{v}_b} \varepsilon_0\mu_0^2 \left(\frac{I_e(\omega)}{2\pi} \ln\left(\frac{\rho}{r_c}\right)\right)^2 \mathrm{d}v}_{=\tilde{C}_1} \\ &\quad + \omega_0^2 \underbrace{\iiint_{\mathrm{v}_a+\mathrm{v}_o} \varepsilon_0\mu_0^2 \left(\frac{I_e(\omega)}{2\pi} \ln\left(\frac{\rho}{r_c}\right)\right)^2 \mathrm{d}v}_{=\tilde{C}_2}. \end{aligned} \tag{5.7}$$

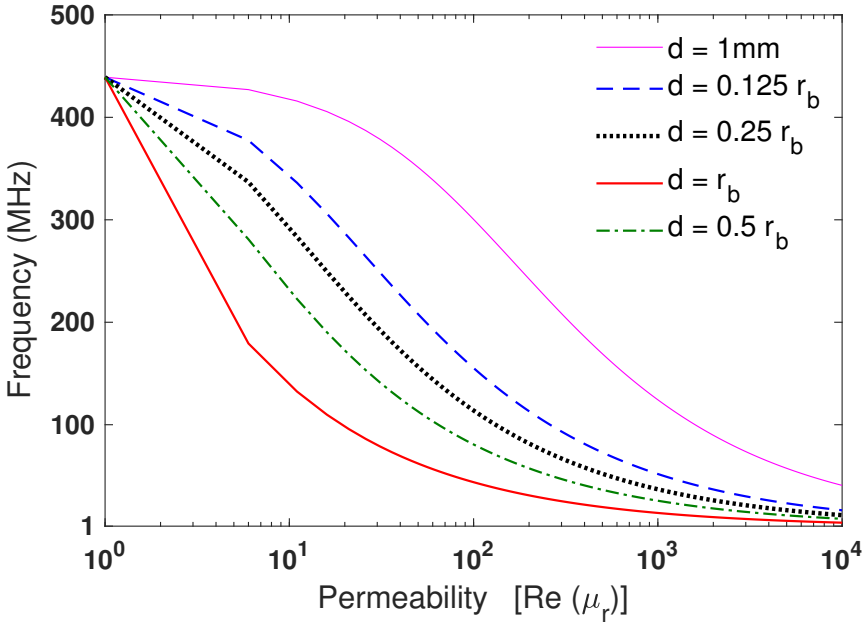

(a)

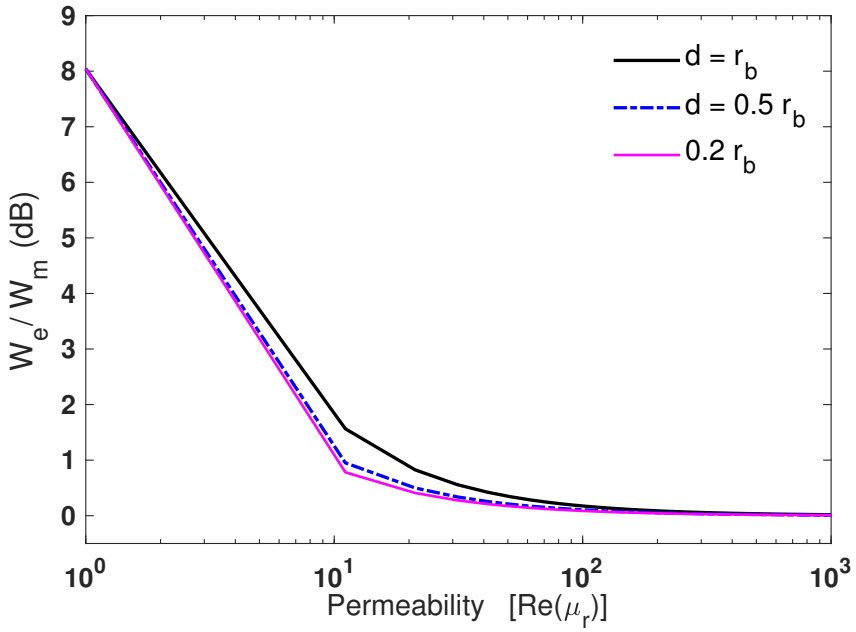

(b)

Figure 5.3: (**a**) The resonant frequency of the top-loaded monopole antenna for different values of the magnetic material thickness as calculated using (5.6). (**b**) The ratio between the stored electric and magnetic energies in the existence of the magnetic material.

Subsequently, the resonant frequency is written using (5.7)

$$\omega_0 = \sqrt{\frac{\mu_r \mu_0 \tilde{L}}{\mu_r^2 \tilde{C}_1 + \tilde{C}_2}}. \tag{5.8}$$

Equations (5.6) and (5.8) demonstrate that the resonant frequency is a function of the geometrical dimensions of both the top-loaded monopole antenna and the thickness of the magnetic material. We solve (5.8) to the exact geometrical dimensions considered in Section 5.2 and with different values of the magnetic material thickness. It is evident in Fig. 5.3a that the resonant frequency correlates inversely with the relative permeability. For example, for the free space case ($\mu_r = 1$) where no magnetic material exists, the top-loaded monopole antenna produces a resonant frequency of $f_0 = 437$ MHz. After that, any further increase in the relative permeability of the magnetic material results in a drastic decrease in the operating frequency, i.e., the stored magnetic energy in the magnetic shell increases enough to compensate for the stored electric energy under the upper disk, as shown in Fig. 5.3b. However, there are upper limitations to the maximum value of the relative permeability, i.e., the stored magnetic energy in the magnetic material reaches a plateau such that any further increase in the relative permeability offers a little increase in the stored magnetic energy. Consequently, a slight reduction in the resonant frequency is produced, as shown in Fig. 5.3b and Fig. 5.3a. On the other hand, there are lower bounds for the lowest fundamental resonant frequency, which the top-loaded monopole antenna can produce regardless of any further increase in the relative permeability value of the magnetic material. For example, figure 5.3a manifests that any further increase in the relative permeability beyond $\mu_r > 1000$ offers a slight decrease in the resonant frequency.

5.2.3 Partial Filling with a Dispersive Magnetic Material

Since the magnetic material is considered dispersive with a frequency-dependent relative permeability $\mu_r(\omega) = \mu'(\omega) - j\mu''(\omega)$, the stored magnetic energy can be computed according to (4.22b) as

$$\begin{aligned} W_{\mathrm{m}}(\omega) &= \frac{1}{4}\left\{ \frac{\mathrm{d}[\omega\mu'(\omega)]}{\mathrm{d}\omega} \iiint\limits_{\mathrm{v}_b} \mu_0 \mid H_\varphi \mid^2 \mathrm{d}v + \iiint\limits_{\mathrm{v}_a+\mathrm{v}_0} \mu_0 \mid H_\varphi \mid^2 \mathrm{d}v \right\} \\ &= \frac{\mid I_e(\omega) \mid^2}{4}\left\{ \frac{\mathrm{d}[\omega\mu'(\omega)]}{\mathrm{d}\omega} \underbrace{\frac{\mu_0}{(2\pi)^2} \iiint\limits_{\mathrm{v}_b} \frac{1}{\rho^2}\mathrm{d}v}_{=\tilde{L}_1} + \underbrace{\frac{\mu_0}{(2\pi)^2} \iiint\limits_{\mathrm{v}_a+\mathrm{v}_0} \frac{1}{\rho^2}\mathrm{d}v}_{=\tilde{L}_2} \right\} \\ &= \frac{\mid I_e(\omega) \mid^2}{4}\left\{ \frac{\mathrm{d}[\omega\mu'(\omega)]}{\mathrm{d}\omega} \tilde{L}_1 + \tilde{L}_2 \right\}, \end{aligned} \tag{5.9}$$

where v_0 represents an equivalent expression for the volume outside the upper disk, which is virtually extended by Δr as shown in Fig. 5.1b. This equivalent extension is due to the fringing fields at the edges of the upper disk. According to [75, Eq. 33], Δr can be approximately estimated as

$$\Delta r \approx \left[\frac{2r_b h}{\pi}\left(\ln(\frac{r_b}{2h}) + 0.665\frac{h}{r_b}\right) + r_b^2\right]^{\frac{1}{2}} - r_b. \tag{5.10}$$

The stored electric energy is calculated using (4.22a) as

$$\begin{aligned} W_{\mathrm{e}}(\omega) &= \frac{1}{4}\left\{\iiint\limits_{\mathrm{v}_b} \varepsilon_0 \mid E_z \mid^2 \mathrm{d}v + \iiint\limits_{\mathrm{v}_0+\mathrm{v}_a} \varepsilon_0 \mid E_z \mid^2 \mathrm{d}v\right\} \\ &= \frac{\mid I_e(\omega) \mid^2}{4}\left\{\omega^2\mu'^2(\omega)\underbrace{\iiint\limits_{\mathrm{v}_b} \frac{\mu_0^2\varepsilon_0}{(2\pi)^2}\ln^2\left(\frac{\rho}{r_c}\right)\mathrm{d}v}_{=\tilde{R}_1} + \omega^2\underbrace{\iiint\limits_{\mathrm{v}_0+\mathrm{v}_a} \frac{\mu_0^2\varepsilon_0}{(2\pi)^2}\ln^2\left(\frac{\rho}{r_c}\right)\mathrm{d}v}_{=\tilde{R}_2}\right\} \\ &= \frac{\mid I(\omega) \mid^2}{4}\left\{\omega^2\mu'^2(\omega)\tilde{R}_1 + \omega^2\tilde{R}_2\right\}. \end{aligned} \tag{5.11}$$

At resonance, the stored electric and magnetic energies are equal. Therefore, using (5.9) and (5.11) we get

$$\frac{\mathrm{d}[\omega\mu'(\omega)]}{\mathrm{d}\omega}\tilde{L}_1 - \omega^2\mu'^2(\omega)\tilde{R}_1 = \omega^2\tilde{R}_2 - \tilde{L}_2. \tag{5.12}$$

After some operations, (5.12) is rewritten as

$$\frac{d\mu'(\omega)}{d\omega} + \frac{\mu'(\omega)}{\omega} - \frac{\tilde{R}_1}{\tilde{L}_1}\omega\mu'^2(\omega) = \omega\mu_0^2\frac{\tilde{R}_2}{\tilde{L}_1} - \frac{\mu_0}{\omega}\frac{\tilde{L}_2}{\tilde{L}_1}. \tag{5.13}$$

Equation (5.13) clearly represents the *Riccati* differential equation which is generally difficult to be solved.

Numerically, the integrals $\tilde{L}_2, \tilde{R}_2$ have infinitesimal values due to the direct relation with μ_0^2, ε_0 and thus can be neglected, while the integrals $\tilde{L}_1, \tilde{R}_1$ can not be omitted for very high permeability $\mu'(\omega) \gg 1$ according to the following inequalities

$$\frac{\mathrm{d}[\omega\mu'(\omega)]}{\mathrm{d}\omega}\tilde{L}_1 \gg \tilde{L}_2 \tag{5.14a}$$

$$\mu'^2(\omega)\tilde{R}_1 \gg \tilde{R}_2. \tag{5.14b}$$

These inequalities demonstrate that most of the stored electric and magnetic energies are concentrated within the magnetic material. Subsequently, by neglecting the right side of (5.12), the *Riccati* differential equation (5.13) reduces to the *Bernoulli* linear differential equation as

$$\frac{d\mu'(\omega)}{d\omega} + \frac{\mu'(\omega)}{\omega} = \frac{\tilde{R}_1}{\tilde{L}_1}\omega\mu'^2(\omega). \tag{5.15}$$

The solution of (5.15) can be easily obtained as

$$\mu'(\omega) = \frac{\tilde{L}_1}{\omega(A_0\tilde{L}_1 - \tilde{R}_1\omega)}. \tag{5.16}$$

where A_0 is an arbitrary constant of dimension Am/V.

Equation (5.16) verifies that the relative permeability of the magnetic material is frequency-dependent and a function of the geometrical dimensions of the top-loaded monopole antenna. However, only the real part $\mu'(\omega)$ of the relative permeability can be calculated using (5.16). The imaginary part $\mu''(\omega)$ can be directly computed from the real part $\mu'(\omega)$ using the Kramers-Kronig transformations as

$$\mu'(\omega) = 1 + \frac{2}{\pi} \int_0^\infty \frac{\psi \mu''(\psi) - \omega \mu''(\omega)}{\psi^2 - \omega^2} d\psi \tag{5.17a}$$

$$\mu''(\omega) = \frac{-2\omega}{\pi} \int_0^\infty \frac{\mu'(\psi) - \mu'(\omega)}{\psi^2 - \omega^2} d\psi. \tag{5.17b}$$

By selecting the thickness of the magnetic material $d = 1$ mm and assuming two arbitrarily values of the constant $A_0 = 2\text{x}10^{-12}$ and $3\text{x}10^{-13}$ while keeping the exact geometrical dimensions of the top-loaded monopole antenna unchanged, the real part $\mu'(\omega)$ is calculated using (5.16) as indicated to as original values (solid curves) in Fig. 5.4a. The values of the imaginary part $\mu''(\omega)$ of the complex permeability are computed using the KK-integral of (5.17b) as depicted in Fig. 5.17b. To check for the consistency between the calculated values of $\mu'(\omega)$ and $\mu''(\omega)$, an additional KK-transform using (5.17a) is applied on the data shown in Fig. 5.4b. It is obvious that the obtained results (broken curves in Fig. 5.4a) are in good agreement with the original values of $\mu'(\omega)$ (solid curves).

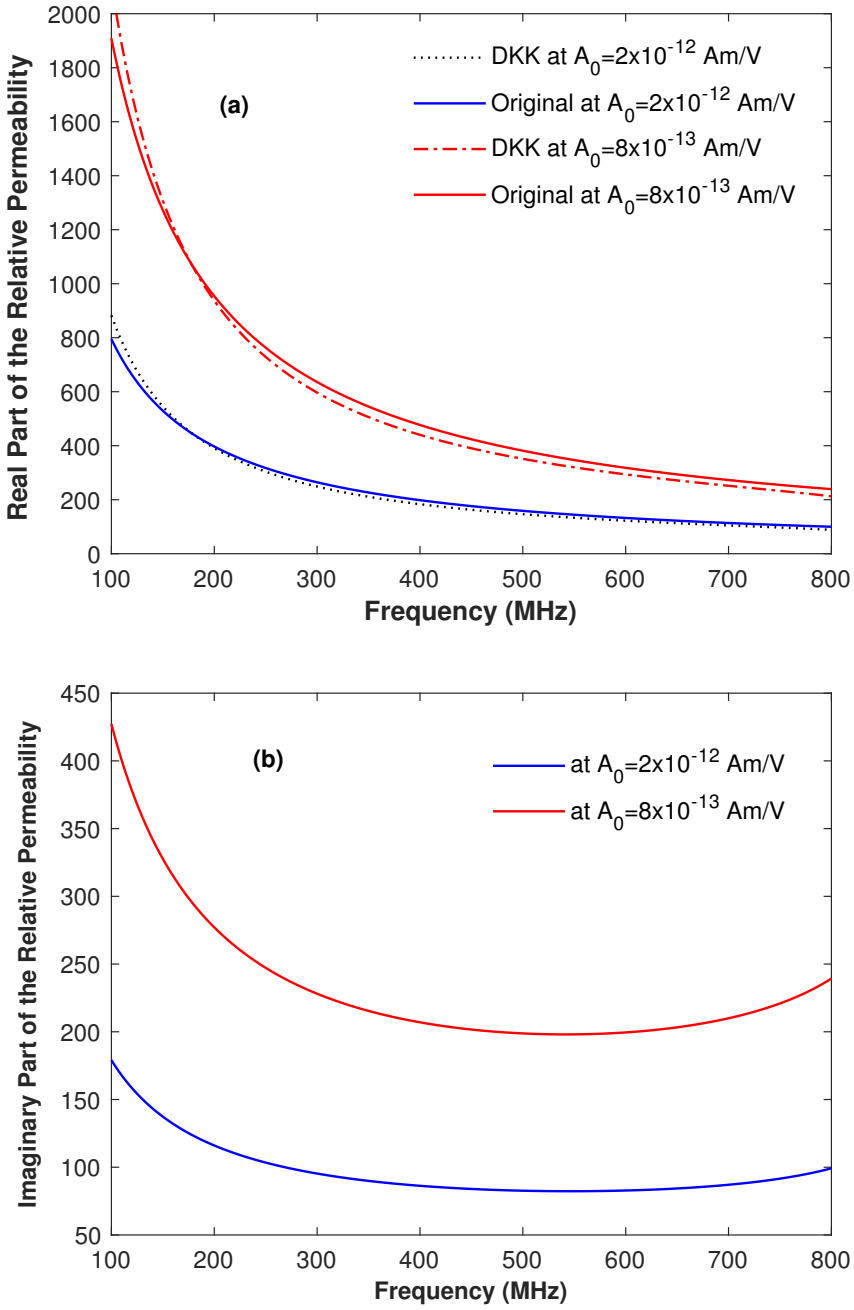

Figure 5.4: The real and the imaginary parts of the relative permeability of the dispersive magnetic material calculated for two different values of A_0 and for the geometrical dimensions mentioned in Section 5.2 and $d = 1$ mm. (**a**) A comparison between the original values of the relative permeability (real part (μ') shown in solid curves) calculated using (5.16) and the double Kramers-Kronig (DDK) transformed values (broken curves) calculated using (5.17)a. (**b**) The imaginary part of the relative permeability μ'' calculated using (5.17)b from the original values of μ'.

5.3 Numerical Results

Equations (5.9)-(5.17), which solve for the frequency-dependent permeability of the magnetic material, are numerically validated by comparing their outputs, for particular values of μ_r and exact geometrical dimensions, with known solutions, for instance, when the top-loaded monopole antenna does not contain a magnetic material. Firstly, we utilize the frequency-domain solver CST© to simulate the monopole antenna in the existence of the magnetic material. After that, the calculated values of the complex permeability, shown in Fig. 5.4, are used to designate the magnetic properties of the dispersive magnetic material in the frequency-domain simulator.

The following sections investigate the effect of the dispersion in the magnetic material on the disk monopole antenna, such as the input impedance, operating bandwidth, radiation efficiency, and gain. The analysis is mathematically performed and numerically verified using the frequency-domain solver.

5.3.1 Effect of the Dispersion on the Input Impedance and Bandwidth

Due to the substantial reduction in the radiation resistance of the top-loaded monopole antenna, the upper disk is shorted to the ground plane to increase the input impedance and tunes the antenna at an exact frequency [73], as illustrated in Section 5.2. This is because the mutual currents induced between the center conductor and the shorting wire change the electric field vectors under the upper disk and add some additional resonances, making the antenna tunable and increasing the radiation resistance. However, an additional increase in the radiation resistance can be accomplished by enclosing the monopole antenna with magnetic material according to [72]. The induced magnetic current in the magnetic material contributes to the total dipole moment produced by the electric current alone, leading to an increase in the radiation resistance. To illustrate this effect, we follow the approach of Stuart *et al.* [72] by feeding the top-loaded monopole antenna with a uniform electric current $I_e(\omega)$. Consequently, the induced electric dipole moment m_{i_e} at the center conductor (monopole) is calculated according to [76] as

$$m_{i_e} = \frac{2hI_e}{j\omega}. \tag{5.18}$$

Where h is the height of the monopole and the factor of 2 accounts for the ground plane [72, Eq. (10)]. The induced magnetization $\vec{M}$ in the magnetic material is related to the magnetic flux density as $\vec{B} = \mu_0(\vec{H} + \vec{M})$. Therefore the Maxwell-Faraday equation (2.3a) can be rewritten as

$$\begin{aligned} \vec{\nabla} \times \vec{E} &= -j\omega\mu_0(\vec{H} + \vec{M}) \\ &= -j\omega\mu_0\vec{H} + \vec{J}_m, \end{aligned} \tag{5.19}$$

where $\vec{J}_m = -j\omega\mu_0\vec{M}$ is the magnetic current source. According to Wheeler [76], the induced magnetic current I_m in the magnetic material enclosing the top-loaded monopole antenna produces an electric dipole moment m_{i_m} at the center conductor which can be represented as

$$m_{i_m} = \varepsilon_0 I_m A. \tag{5.20}$$

Where $A = \pi\rho^2$ is the cross-sectional area of the circular cylinder under the upper disk. The magnetic current I_m is written in terms of the magnetic current density $\vec{J}_m$ as

$$I_m = -j2\omega\mu_0 X_m H_\varphi h d. \tag{5.21}$$

Since the magnetic current I_m is uniform through the magnetic material, the induced electric dipole moment $\vec{m}_{i_m}$ is concentric at the base of the monopole antenna and points upward parallel to the z-axis. Since the magnetic current I_m has units of volts, the induced electric dipole moment in (5.20) has units of (Coulomb-meter) similar to (5.18). Consequently, the two electric dipole moments m_{i_e} and m_{i_m} add in-phase at the center of the antenna to give a total electric dipole moment as

$$p_e = m_{i_e} + m_{i_m}. \tag{5.22}$$

The radiated power is computed in terms of the total electric dipole moment [61] as

$$P_{\mathrm{r}} = \frac{1}{2}|I_e|^2 R_{\mathrm{r}} = \frac{\pi\eta_0}{6}\left(\frac{\omega}{\lambda_0}\right)^2 |p_e|^2, \tag{5.23}$$

where η_0 and λ_0 are the free space impedance and wavelength, respectively. Using (5.18) to (5.23) and the constitutive relation of the magnetic susceptibility $X_m = \mu_r - 1$, the radiation resistance of the top-loaded monopole antenna coated by a magnetic material can be written as

$$R_{\mathrm{r}} = \frac{4\pi\eta_0}{3|I_e|^2}\left(\frac{h}{\lambda_0}\right)^2 \left(I_e + \kappa^2 A H_\varphi(\mu_r - 1)d\right)^2. \tag{5.24}$$

The second term in the brackets in (5.24) represents the effect of the magnetic material on the antenna radiation resistance. The factor $(\mu_r - 1)d$ is only related to the magnetic material, i.e., for the free space case $\mu_r = 1$, the radiation resistance reduces to the well-known equation of the monopole antenna [61]

$$R_{\mathrm{r}} = \frac{4\pi\eta_0}{3}\left(\frac{h}{\lambda_0}\right)^2. \tag{5.25}$$

Using (5.2) and for a complex permeability $\mu_r = \mu' - j\mu''$, the radiation resistance in (5.24) is recast to

$$R_{\mathrm{r}} = \frac{4\pi\eta_0}{3}\left(\frac{h}{\lambda_0}\right)^2 \left[\left(1 + \kappa^2 A\frac{(\mu'-1)d}{2\pi\rho}\right) - j\kappa^2 A\frac{\mu'' d}{2\pi\rho}\right]^2. \tag{5.26}$$

It is clear that both the real and the imaginary parts of the complex permeability contribute to the radiation resistance. On the other hand, the input resistance of the top-loaded monopole antenna is derived using (5.4) and ([74], Eq. (18)) as

$$\begin{aligned} R_{\mathrm{in}} &= R_r + R_l \\ &= R_{\mathrm{r}} + \frac{\omega}{2}\iiint\limits_{\mathrm{v}_b} \mu'' \mid H_\phi \mid^2 \mathrm{d}v + \frac{\omega}{2}\iiint\limits_{\mathrm{v}_o+\mathrm{v}_a} \left(\varepsilon_0 \mid E_z \mid^2 + \mu_0 \mid H_\phi \mid^2\right) \mathrm{d}v, \end{aligned} \tag{5.27}$$

where R_l is loss resistance and is computed from the integrals in (5.27). Equations (5.26) and (5.27) demonstrate that both the real and the imaginary parts of the complex permeability

of the magnetic material contribute to the radiation and input resistances of the top-loaded monopole antenna. For a highly dispersive permeability $\mu_r(\omega) >> 1$, the radiation resistance and the input impedance can be increased over a broad frequency range.

By selecting the thickness of the magnetic material d=1 mm, the frequency-domain solver calculates the input impedance of the top-loaded monopole antenna with and without the dispersive magnetic material as depicted in Fig. 5.5. An input impedance matching over a broad frequency range is achieved by coating the cylindrical volume under the upper disk with a dispersive magnetic material compared with the conventional one, where no magnetic material exists.

Likewise, the operating bandwidth increases when the antenna contains a dispersive magnetic material, as illustrated in the simulated reflection coefficient in Fig. 5.6. However, the dispersion in the magnetic material assists in increasing the bandwidth only over the low frequencies, i.e., for the frequencies lower than the fundamental resonant frequency of the monopole antenna when no magnetic material exists. This result is interpreted from the inverse relationship between the relative permeability and the operating frequency, as shown in (5.16). The relative permeability is not only a function of the operating frequency but also depends on the geometrical dimensions of the monopole antenna, i.e., the presence of a magnetic material under the upper disk changes the operating frequency to values below the fundamental resonant frequency.

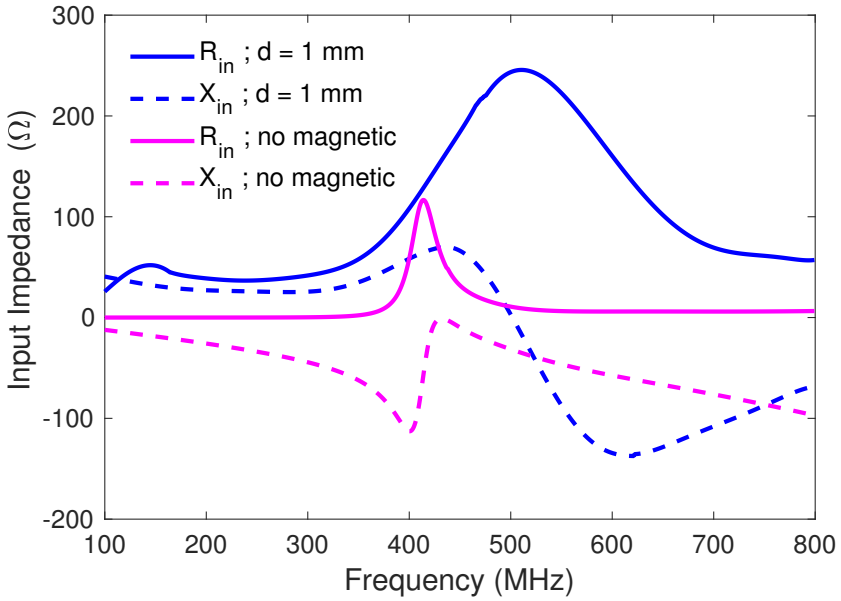

Figure 5.5: Input impedance of the top loaded monopole antenna without magnetic material (shown in pink curves) and with magnetic material (shown in blue curves). Results are numerically obtained using the frequency-domain solver CST© and the calculated values of the complex permeability in Fig. 5.4.

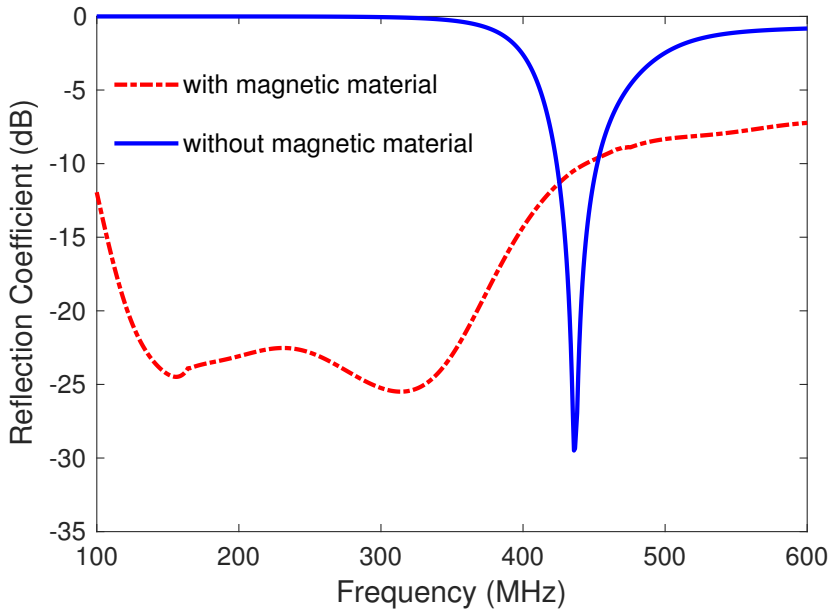

Figure 5.6: A comparison between the input reflection coefficients of the top-loaded monopole antenna without magnetic material (blue curve) and with magnetic material (red curve), where $d = 1$ mm and the complex relative permeability is chosen from Fig. 5.4 at $A_0 = 8\text{x}10^{-13}\ Am/V$.

5.3.2 The Magnetic Dispersion Effect on the Stored Electromagnetic Energy

The capacitive loading of the upper disk of the monopole antenna in the absence of the magnetic material produces a large electric field around the center conductor, as derived in (5.3), where the electric field inversely correlates with the disk radius. Therefore, a large size of the upper disk increases the stored electric energy leading to a drastic decrease in the radiation resistance. We desire to reduce the stored electric energy while maintaining the geometrical dimensions of the top-loaded monopole antenna unchanged. Stuart *et al.*, [72] eliminated the stored electric energy at single frequencies by enclosing the monopole antenna with a thin shell of high-permeability non-dispersive magnetic material. Following the same approach but with the monopole antenna enclosed by a highly dispersive magnetic material, the stored magnetic energy in the magnetic material compensates for the stored electric energy under the upper disk over a broader frequency range. The frequency-domain solver is utilized to illustrate the effect of the dispersive magnetic material on the stored electromagnetic energies of the top-loaded monopole antenna. The calculated values of the complex permeability shown in Fig. 5.4 are used to characterize the magnetic material in the frequency-domain simulator.

Figure 5.7 depicts the simulated electric field distribution under the upper disk when the dispersive magnetic material coats the monopole antenna. It is evident that the magnetic material drastically affects the electric field distribution. For instance, by selecting a complex permeability of $\mu_r = 200 - j92$, the electric field magnitudes under the upper disk remain unchanged. However, as the value of the real and the imaginary parts of μ_r increase, the electric field gradually decreases, as shown in Fig. 5.8b,c. Notice that the electric field can

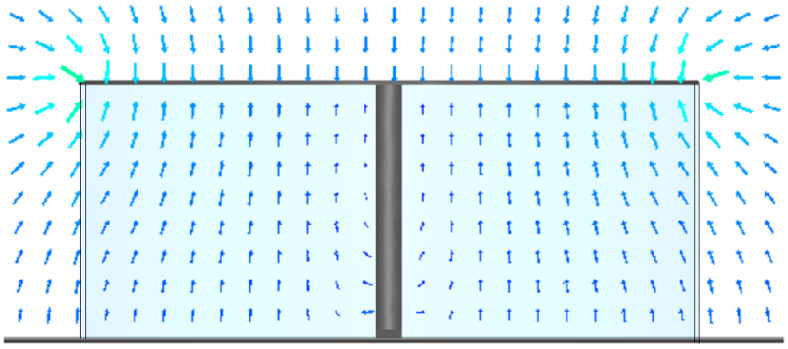

(a) at $\mu_r = 200 - j92$ and $f_0 = 388$ MHz.

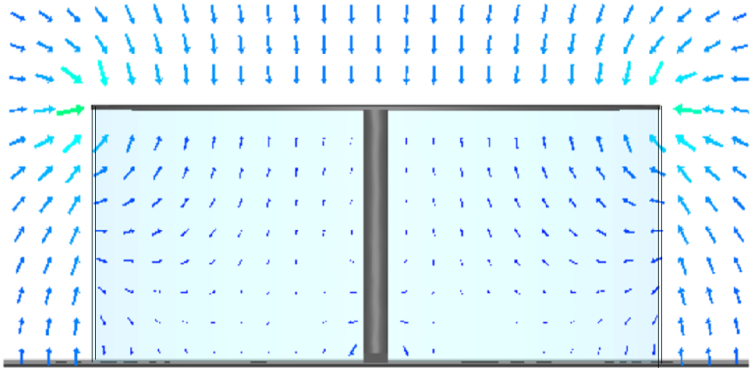

(b) at $\mu_r = 880 - j266.2$ and $f_0 = 233$ MHz.

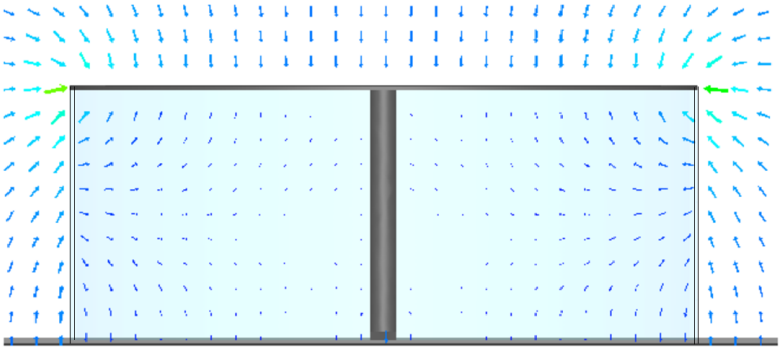

(c) at $\mu_r = 1947 - j402$ and $f_0 = 128$ MHz.

Figure 5.7: The distribution of the electric field vectors under the upper disk of the electric monopole antenna at different values of the frequency-dependent permeability.

be eliminated only in the cylindrical volume enclosed by the magnetic material, i.e., the area under the upper disk, while the electric field amplitudes outside stay unchanged regardless of the relative permeability value.

The reduction in the electric field magnitudes highly affects the stored electric energy under the upper disk. However, only the real part of the complex permeability affects both the electric field and the stored electric energy as derived in (5.11), i.e., a high reduction in the stored electric energy can only be accomplished for large values of the real part of the complex permeability regardless of the value of the imaginary part. For example, Fig. 5.8 depicts the top-loaded monopole antenna's stored electric energy for different complex permeability values. For small values of the complex permeability, a slight reduction in the stored electric energy under the upper disk is accomplished, as illustrated in Fig. 5.8a, while, in contrast, a drastic reduction in the stored electric energy occurs for large values of the permeability. Nevertheless, it is clear that the stored electric energy still reduces at different frequencies as the permeability values increase, demonstrating the concept of deploying highly dispersive magnetic materials to eliminate the stored electric energy over a broad frequency range.

5.3.3 Effect of the Dispersion on the Gain

Although the high dispersion in the real part of the complex permeability of the magnetic material significantly reduces the stored electric energy and increases the operating bandwidth, the imaginary part degrades both the radiation efficiency and the gain of the top-loaded monopole antenna. From (5.4), the accepted power $P_{acc}(\omega)$ is calculated according to ([74] Eq. (44)) as

$$P_{acc}(\omega) = \frac{1}{2}|I_e(\omega)|^2 R_{\text{in}} = P_r(\omega) + P_l(\omega), \tag{5.28}$$

where R_{in} is the input resistance of the monopole antenna and is computed using (5.27). The radiated power $P_r(\omega)$ is calculated as

$$P_r(\omega) = \frac{1}{2}|I_e(\omega)|^2 R_{\text{r}}, \tag{5.29}$$

where R_r is the radiation resistance as in (5.26), while $P_l(\omega)$ refers to the power loss and is computed from the internal losses of the antenna as

$$\begin{aligned} P_l(\omega) &= \frac{1}{2}|I_e(\omega)|^2 R_l \\ &= |I_e(\omega)|^2 \omega \Bigg(\iiint\limits_{\text{v}_b} \mu'' \mid H_\phi \mid^2 \, \text{d}v + \iiint\limits_{\text{v}_o+\text{v}_a} \left(\varepsilon_0 \mid E_z \mid^2 + \mu_0 \mid H_\phi \mid^2 \right) \text{d}v \Bigg). \end{aligned} \tag{5.30}$$

The first integral of (5.30), which computes the power loss in the magnetic material, is a function of the imaginary part of the complex permeability. From (5.28)-(5.30), the radiation efficiency of the top-loaded monopole antenna is calculated as

$$e_c(\omega) = \frac{P_r(\omega)}{P_r(\omega) + P_l(\omega)}. \tag{5.31}$$

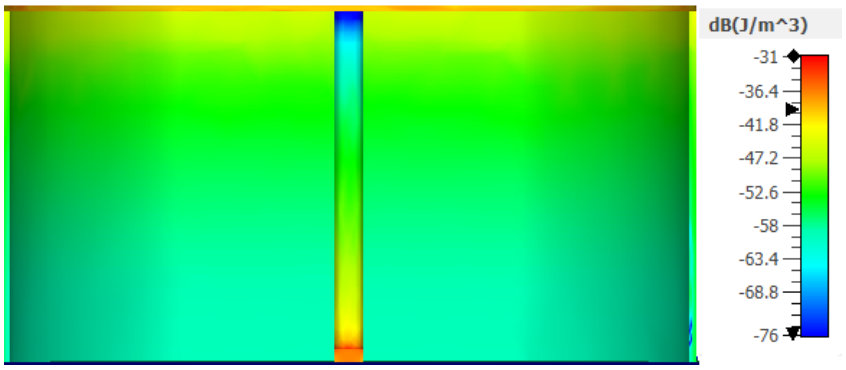

(a) at $\mu_r = 200 - j92$ and $f_0 = 388$ MHz.

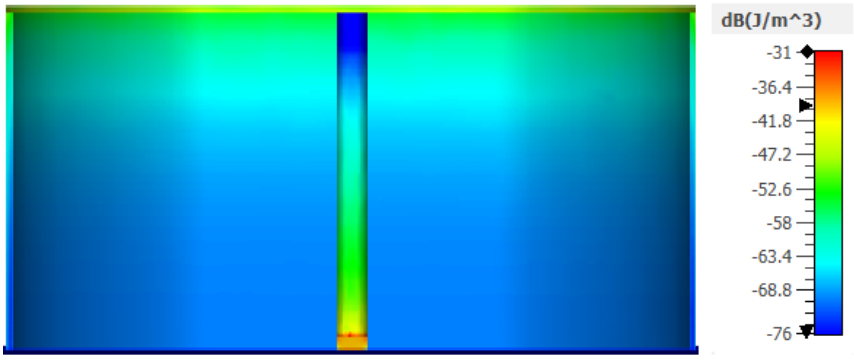

(b) at $\mu_r = 880 - j266.2$ and $f_0 = 233$ MHz.

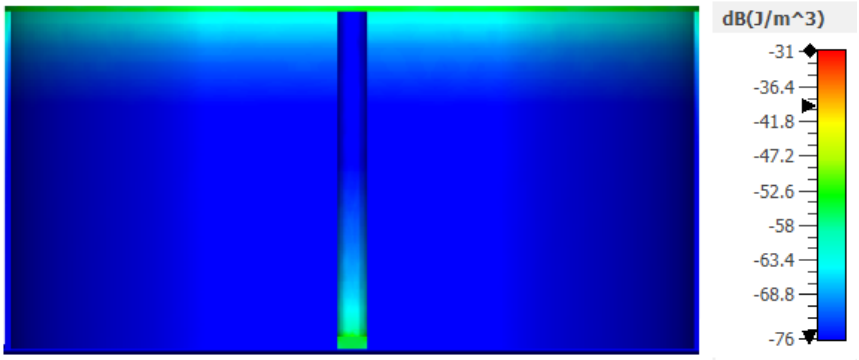

(c) at $\mu_r = 1947 - j402$ and $f_0 = 128$ MHz.

Figure 5.8: The stored electric energy of the top-loaded monopole antenna coated with the magnetic material of different values of the complex permeability **(a)** $\mu_r = 200 - j92$, **(b)** $\mu_r = 880 - j266.2$, and **(c)** $\mu_r = 1947 - j402$.

It is evident from (5.31) that the radiation efficiency inversely correlates with the imaginary part of the complex permeability of the magnetic material. The gain $G(\omega)$ of the top-loaded monopole antenna can be calculated according to [61, Ch. 2] using (5.31) as

$$G(\omega) = e_c(\omega)D(\omega), \tag{5.32}$$

where $D(\omega)$ refers to the antenna directivity and is dimensionless. We again utilize the frequency-domain simulator to numerically estimate both the radiation efficiency and the gain of the electric monopole antenna in the existence of the dispersive magnetic material. The validity of the results is tested by comparing them with that of the monopole antenna, where no magnetic material exists.

Equations (5.28)-(5.32) are numerically validated using the frequency domain solver. Figure 5.9 depicts the simulated radiation efficiency of the top-loaded monopole antenna with and without the dispersive lossy magnetic material. The loss tangent $\tan(\delta) = \mu''/\mu'$ refers to the magnetic losses. The value of the real part of the complex permeability is selected and fixed to be equal to $\mu' = 420$, while the imaginary part is changeable as $\tan(\delta) = 0, 0.25, 0.5$. The radiation efficiency is negatively affected by the increasing magnetic losses of the dispersive magnetic material. The antenna has a low radiation efficiency even by enclosing the monopole antenna with a non-dispersive magnetic material, i.e., $\tan(\delta) = 0$. For instance, the efficiency is still lower than 30% for any value of the loss tangent.

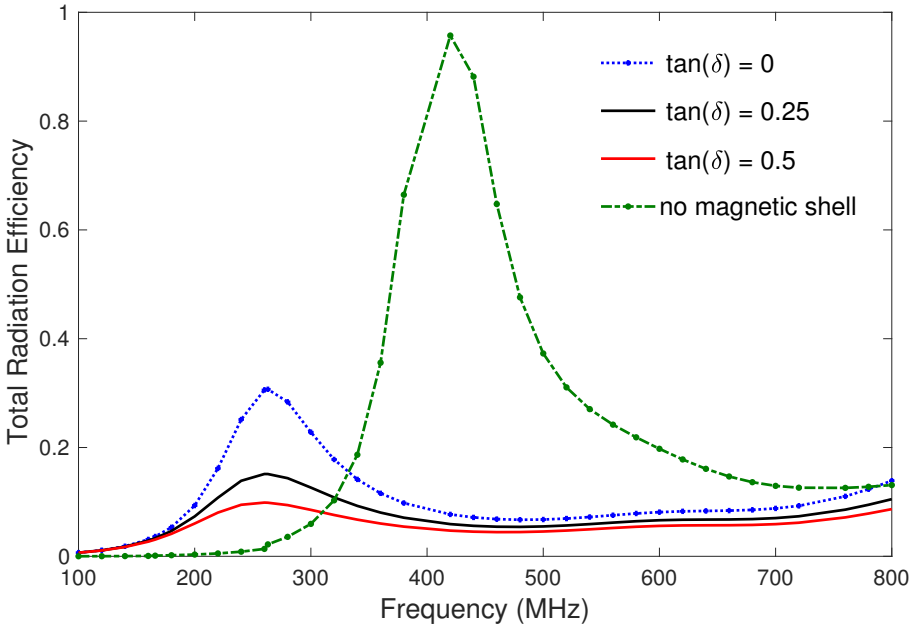

Figure 5.9: A comparison between the radiation efficiency of the top-loaded monopole antenna with and without the dispersive magnetic material. The real part of the complex permeability is kept equal to $\mu' = 420$, while the imaginary part is assumed changeable for different values of the magnetic losses $\tan(\delta) = 0, 0.25, 0.5$.

The high reduction in the radiation efficiency due to the magnetic losses degrades the antenna gain according to (5.31)-(5.32). Therefore, the dispersive lossy magnetic material strongly affects the gain and directivity of the top-loaded monopole antenna. For instance, for the open disk monopole antenna, i.e., no magnetic material exists, the efficiency approaches unity as shown in Fig. 5.9; thus, the gain and directivity are nearly equal as illustrated in Fig. 5.10. In contrast, the radiation efficiency $e_c(\omega)$ decreases by increasing the relative permeability, resulting in a rapid reduction in the gain of the monopole antenna compared with the directivity.

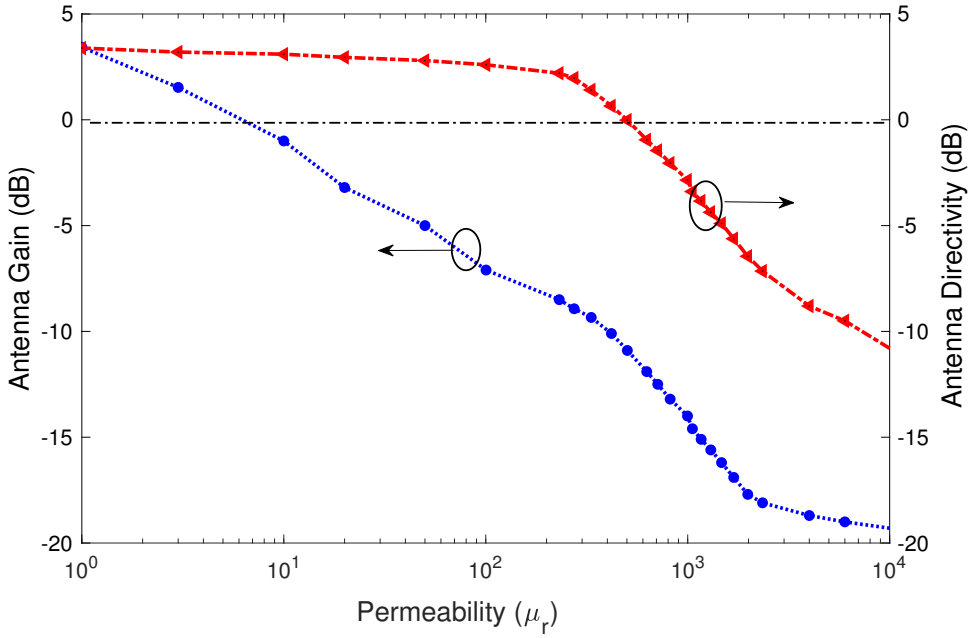

Figure 5.10: A comparison between the gain and directivity of the top-loaded monopole antenna in the presence of a the dispersive lossy magnetic material.

5.4 Enclosing the Monopole Antenna with a Slotted-Magnetic Material

This section numerically investigates the effect of the existence of slots in the magnetic material on the performance of the top-loaded monopole antenna. It will be shown that enclosing the monopole antenna with a longitudinally slotted magnetic material reduces the stored electric energy and increases the gain of the top-loaded monopole antenna. The analysis is numerically validated using the full-wave simulator CST©.

5.4.1 Non-dispersive Slotted-Magnetic Material

By a longitudinal cutting in the magnetic material, which coats the monopole antenna as shown in Fig. 5.11, the induced magnetic dipole moment in (5.20) and both the radiation

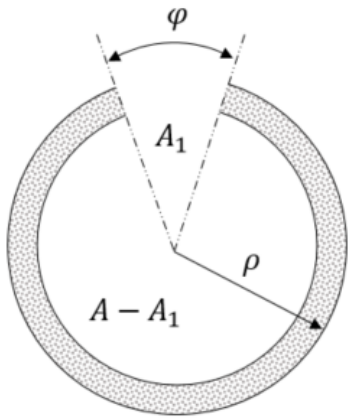

Figure 5.11: A cross-sectional top view of the magnetic material with a longitudinal slot.

resistance and input impedance in (5.26) and (5.27) are no longer accurate. To account for the effect of slots on the antenna radiation resistance, we assume, for simplicity, that the magnetic field H_φ is still uniform everywhere and defined as in (5.2). If the slotted sector of the magnetic material (referred to as $A_1 = \frac{1}{2}\phi\rho^2$) is contained free space, the induced magnetic dipole moment m_{i_m} can be rewritten as

$$m_{i_m} \cong \varepsilon_0 I_m (A - lA_1), \tag{5.33}$$

where $l = 0, 1, 2, 3, ...$ refers to the number of sectors, when the magnetic material is evenly cut into several sectors. Consequently, the radiation resistance in (5.24) can be recast using (5.33) as

$$R_{\mathrm{r}} \cong \frac{4\pi\eta_0}{3}\left(\frac{h}{\lambda_0}\right)^2\left(1 + \frac{\kappa^2 A}{2\pi\rho}(\mu_r - 1)d - \frac{\kappa^2 l A_1}{2\pi\rho}(\mu_r - 1)d\right)^2. \tag{5.34}$$

It is evident that the radiation resistance in (5.34) is smaller than its counterpart in (5.24), i.e., the presence of slots in the magnetic material affects both the magnetic dipole moment and the radiation resistance, which assists in changing the resonant modes of the top-loaded monopole antenna. By increasing either the area of the slotted sector or the number of sectors, the radiation resistance in (5.34) approaches to (5.25).

To illustrate the effect of slots on the electric field and the resonant modes, we assume a non-dispersive magnetic material with two slots encloses the top-loaded monopole antenna. The frequency-domain solver simulates the electric field distribution under the upper disk as shown in Fig. 5.12. It is clear that the electric field distribution is different from that of the closed magnetic material shown in Fig. 5.7, i.e., the resonant mode is no longer a transverse magnetic TM_z. Instead, a part of the electric field radially deviates near the magnetic material, i.e., the electric field has not only a z component but also an angular E_φ and radial E_ρ components. However, the slotted-magnetic material still reduces the electric field around the center conductor, which reduces the stored energy.

Equation 5.34 proves that both the permeability values and the geometrical dimensions of the magnetic material contribute to the radiation resistance, i.e., the resonant frequency can be shifted up or down by changing either the size of slots or the relative permeability value, as depicted in Fig. 5.13.

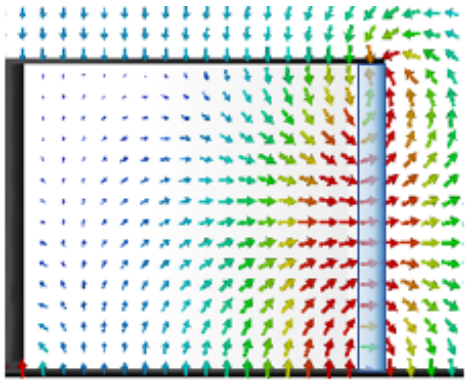

(a) Front view

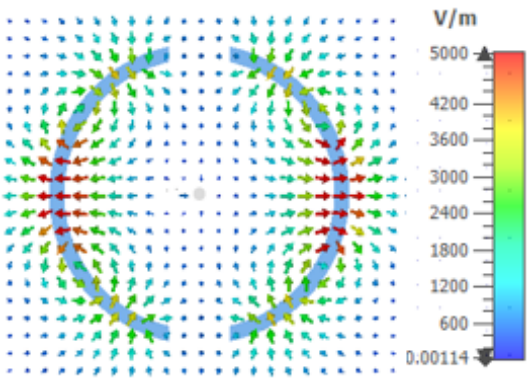

(b) Top view

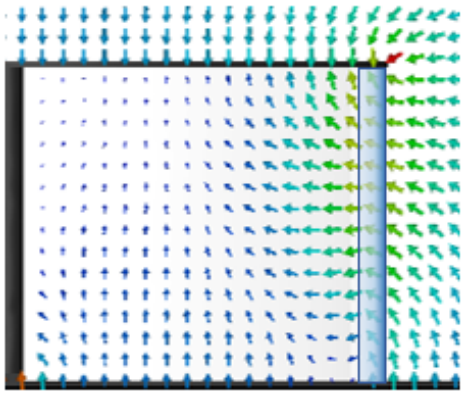

(c) Front view

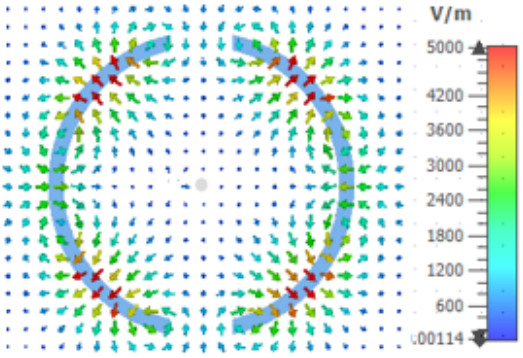

(d) Top view

Figure 5.12: The electric field distribution under the upper disk of the top-loaded monopole antenna when the magnetic material has two sectors with size $\varphi = 30^{o}$ and thickness $d = 5$ mm. The electric field distribution shown in cross-sectional views is illustrated at two different resonant frequencies **(a)**, **(b)** at $f_0 = 391$ MHZ, and **(c)**, **(d)** at $f_0 = 423$ MHZ.

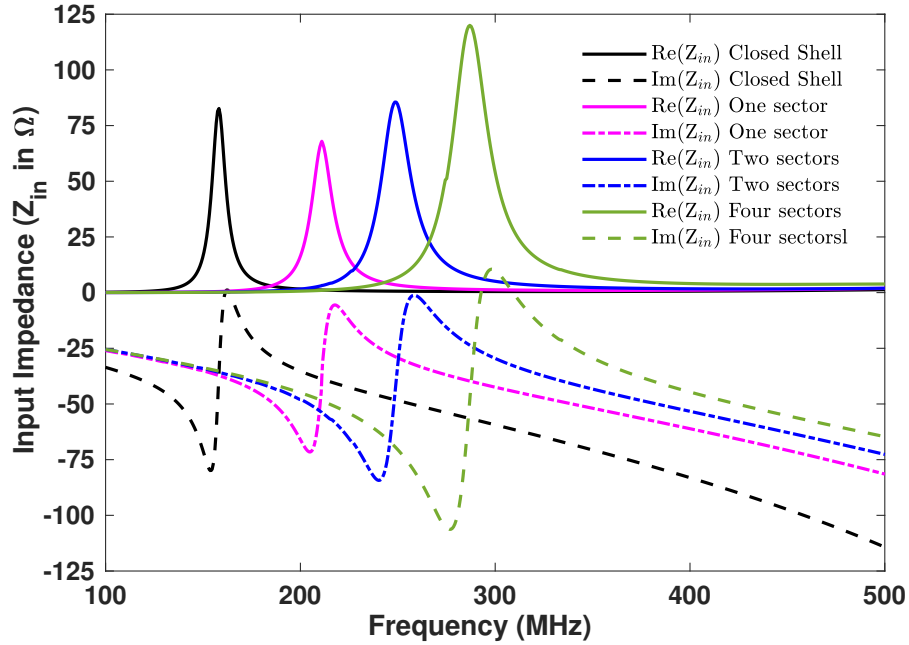

(a)

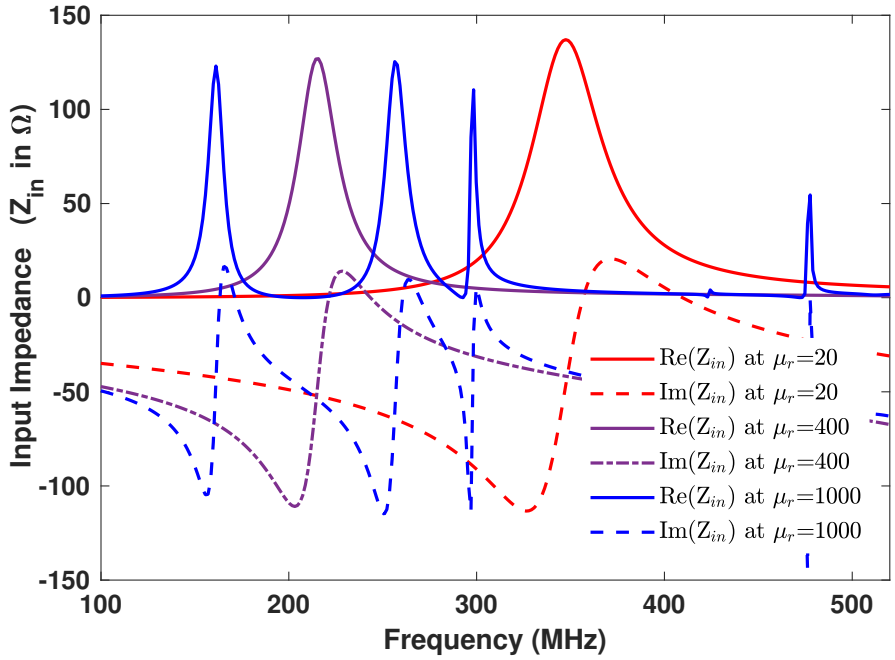

(b)

Figure 5.13: The input impedance of the top-loaded monopole antenna with both closed and slotted-magnetic material. The magnetic material is assumed non-dispersive **(a)** with a real-valued permeability $\mu_r = 200$, thickness $d = 2$ mm, and different sectors, **(b)** with two sectors and different values of the relative permeability.

5.4.2 Gain and Efficiency

One of the distinctive features of the presence of slots in the magnetic material is that the monopole antenna's radiation efficiency and gain are improved compared to the closed magnetic material. Substituting of (5.24) and (5.34) into (5.23) we get

$$P_{r_1}(\omega) = |I_e|^2 \frac{2\pi\eta_0}{3}\left(\frac{h}{\lambda_0}\right)^2\left(1+\frac{\kappa^2 A}{2\pi\rho}(\mu_r-1)d\right)^2 \tag{5.35a}$$

$$P_{r_2}(\omega) = |I_e|^2 \frac{2\pi\eta_0}{3}\left(\frac{h}{\lambda_0}\right)^2\left(1+\frac{\kappa^2 A}{2\pi\rho}(\mu_r-1)d-\frac{\kappa^2 l A_1}{2\pi\rho}(\mu_r-1)d\right)^2, \tag{5.35b}$$

where (5.35a) refers to the radiated power of the top-loaded monopole antenna coated with a closed magnetic material, while (5.35a) is the radiated power when slots exist in the magnetic material. Equation (5.35b) can be rewritten in terms of (5.35a) as

$$\begin{aligned} P_{r_2}(\omega) &= P_{r_1}(\omega) + |I_e|^2 \frac{\eta_0}{6\pi\rho^2}\left(\frac{h}{\lambda_0}\right)^2\left(\kappa^2 l A_1(\mu_r-1)d\right)^2 \\ &\quad - |I_e|^2 \frac{\eta_0 l A_1}{3\pi\rho}\left(\frac{\kappa h}{\lambda_0}\right)^2\left(1+\frac{\kappa^2 A}{2\pi\rho}(\mu_r)d\right) \\ &= P_{r_1}(\omega) + P_\mu(\omega). \end{aligned} \tag{5.36}$$

Substituting of (5.35) and (5.36) into (5.28), the accepted power of the monopole antenna for both the closed and slotted-magnetic material can be written as

$$P_{acc_1}(\omega) = P_{r_1}(\omega) + P_l(\omega) \tag{5.37a}$$

$$P_{acc_2}(\omega) = P_{r_1}(\omega) + P_l(\omega) + P_\mu(\omega). \tag{5.37b}$$

The gain of the top-loaded monopole antenna is calculated using (5.32) and (5.37) as

$$G(\omega) = \frac{4\pi U(\theta,\varphi)}{P_{acc}(\omega)}, \tag{5.38}$$

where U is the maximum radiation intensity calculated from the far fields [14]. Substituting of (5.37) into (5.38), we get

$$G_1(\omega) = \frac{4\pi U(\theta,\varphi)}{P_{r_1}(\omega) + P_l(\omega)} \tag{5.39a}$$

$$G_2(\omega) = \frac{4\pi U(\theta,\varphi)}{P_{r_1}(\omega) + P_l(\omega) + P_\mu(\omega)}. \tag{5.39b}$$

It is clear from (5.39) that the gain inversely correlates with the relative permeability of the magnetic material. However, (5.39b) demonstrates that the number of slots in the magnetic material can increase the gain of the monopole antenna, i.e., by increasing either the size or the number of slots in the magnetic material, the denominator decreases leading to an increase in the gain compared to (5.39a).

We maintain the geometrical dimensions of the top-loaded monopole antenna unchanged while assuming the magnetic material is non-dispersive with different slots. Figure 5.14

depicts the relationship between the relative permeability and the top-loaded monopole antenna's gain and radiation efficiency. The antenna's radiation efficiency rapidly decreases for the closed magnetic material as the permeability increases. For instance, the efficiency decreases to values less than 50% when the relative permeability increases more than $\mu_r > 400$. In contrast, the presence of slots in the magnetic material improves the radiation efficiency, i.e., the efficiency is still greater than 80% for any increase in the relative permeability. Likewise, the gain dramatically decreases as μ_r increases for the closed magnetic material, while a significant improvement in the gain occurs when the slots exist.

5.4.3 Dispersive Slotted-Magnetic Material

Assuming the slotted-magnetic material is highly dispersive with a frequency-dependent permeability $\mu_r(\omega) = \mu'(\omega) - j\mu''(\omega)$, the radiation resistance in (5.34) is recast as

$$R_{\rm r}(\omega) = \frac{4\pi\eta_0}{3}\left(\frac{h}{\lambda_0}\right)^2\left(1 + \frac{\kappa^2(A - lA_1)}{2\pi\rho}(\mu'(\omega) - 1)d - j\frac{\kappa^2(A - lA_1)}{2\pi\rho}(\mu''(\omega)d)\right)^2. \quad (5.40)$$

It is evident that the radiation resistance is complex where both the real and the imaginary parts of the complex permeability contribute in (5.40). The full-wave simulator calculates the input impedance and the reflection coefficient of the top-loaded monopole antenna as shown in Fig. 5.15. The values of the dispersive permeability, obtained using the Kramers-Kronig transformations shown in Fig. 5.4 are utilized to set the magnetic properties of the magnetic material in the frequency-domain simulator. It is obvious that the monopole antenna has a broader input impedance matching for the closed magnetic material compared to that of the slotted-magnetic material. The presence of slots in the dispersive magnetic material can again improve the antenna gain; however, it comes at the expense of narrowing the operating bandwidth.

Eventually, the radiation resistance in (5.40) is smaller than that in (5.26). Therefore, by substituting (5.40) into (5.39b), the gain can be improved where the radiation resistance contributes to the denominator of (5.39b), i.e., the monopole antenna's radiation efficiency and gain can be improved when slots in the magnetic material exist, as clearly depicted in Fig. 5.16.

In conclusion, enclosing the top-loaded monopole antenna with a dispersive or non-dispersive magnetic material reduces the stored electric energy and increases the radiation resistance. Moreover, the dispersion in the permeability of the magnetic material increases the input impedance over a broad bandwidth. However, completely coating the monopole antenna with a magnetic material degrades both the efficiency and the gain due to the increased magnetic losses. This problem can be solved by longitudinal slots in the magnetic material. The existence of slots changes both the radiation resistance and the input impedance, which assists in improving both the gain and the radiation efficiency.

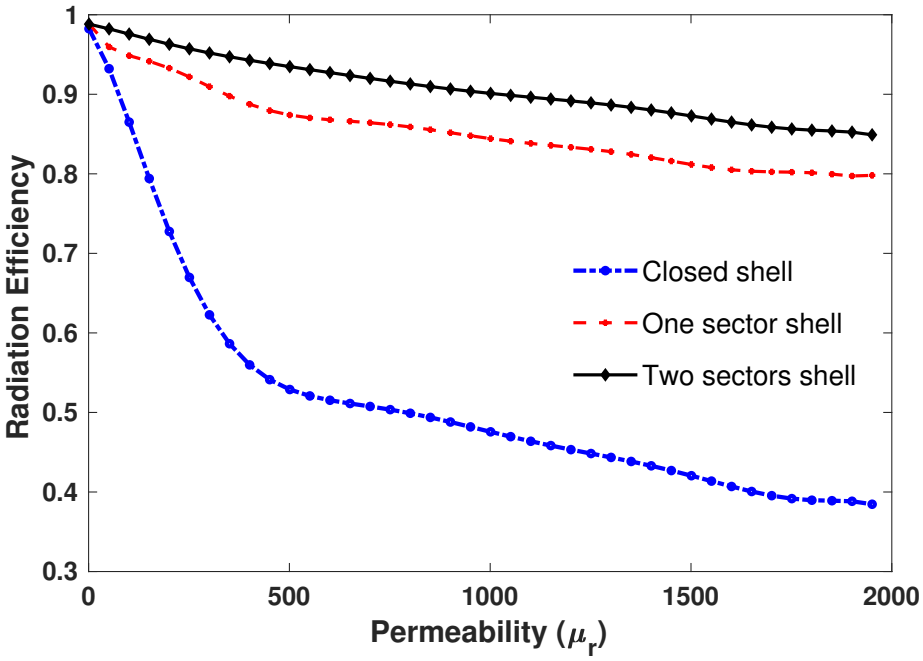

(a)

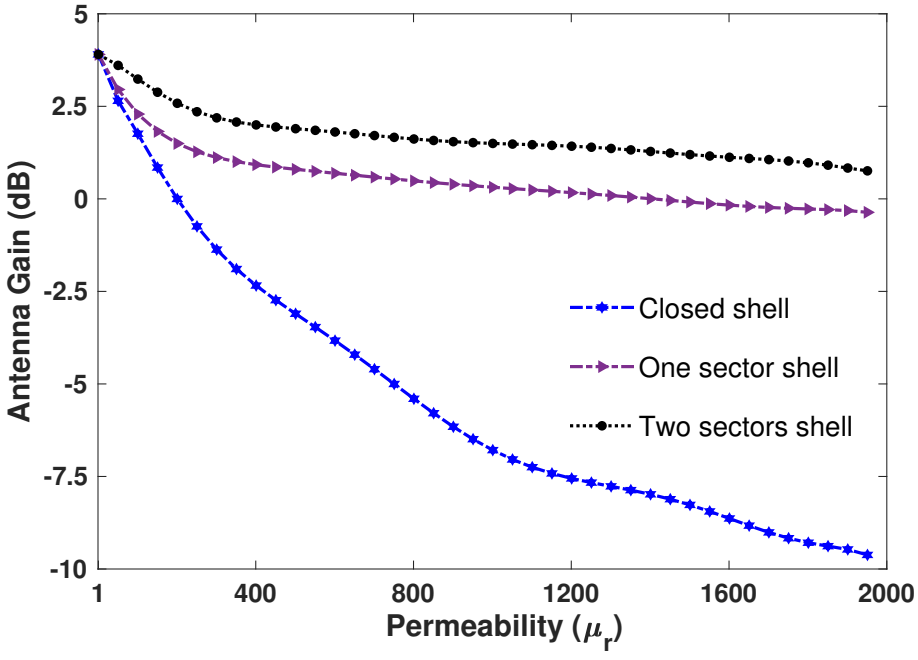

(b)

Figure 5.14: **(a)** The radiation efficiency and **(b)** the gain of the top-loaded monopole antenna as a function of the magnetic permeability. The thickness of the magnetic material is kept at $d = 5$ mm, and the slot size at $\varphi = 30°$.

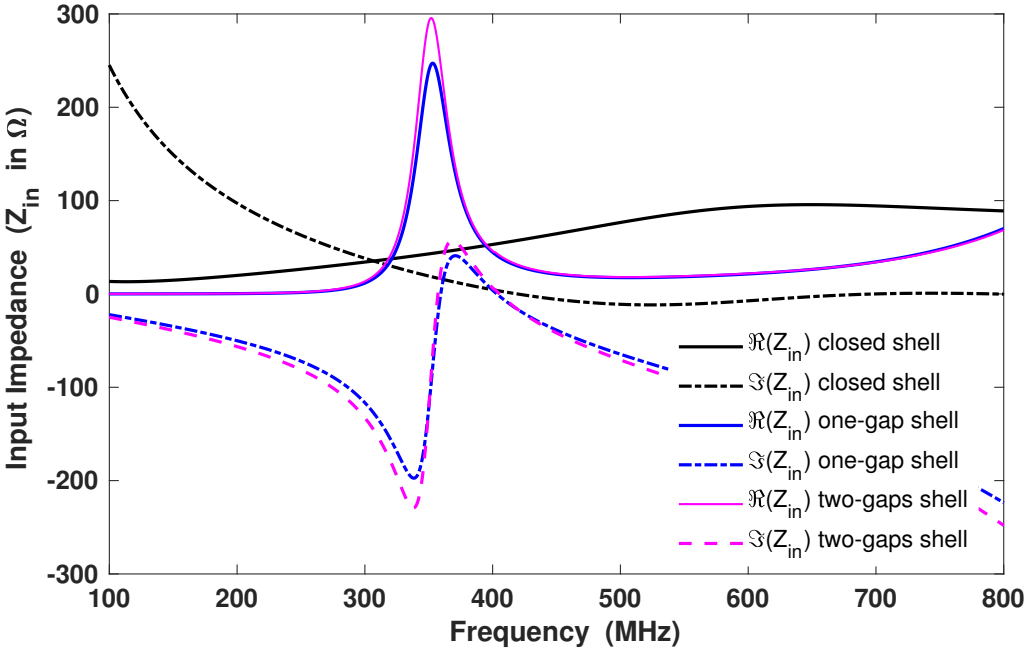

(a)

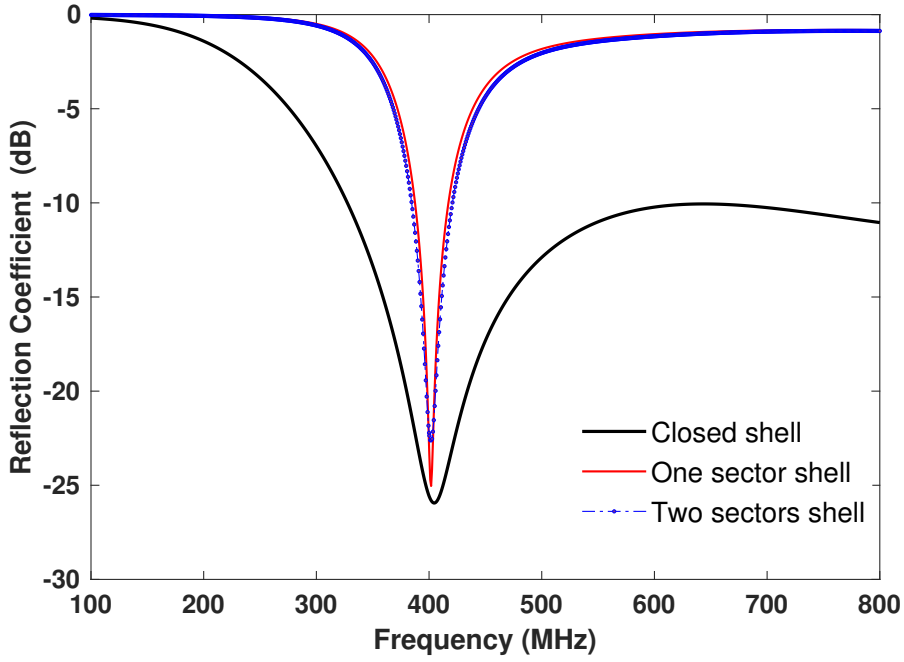

(b)

Figure 5.15: **(a)** The input impedance and **(b)** the reflection coefficient of the top-loaded antenna for a dispersive magnetic material. The thickness and the slot size of the magnetic material are kept at $d = 5$ mm and $\varphi = 30^{\circ}$, respectively.

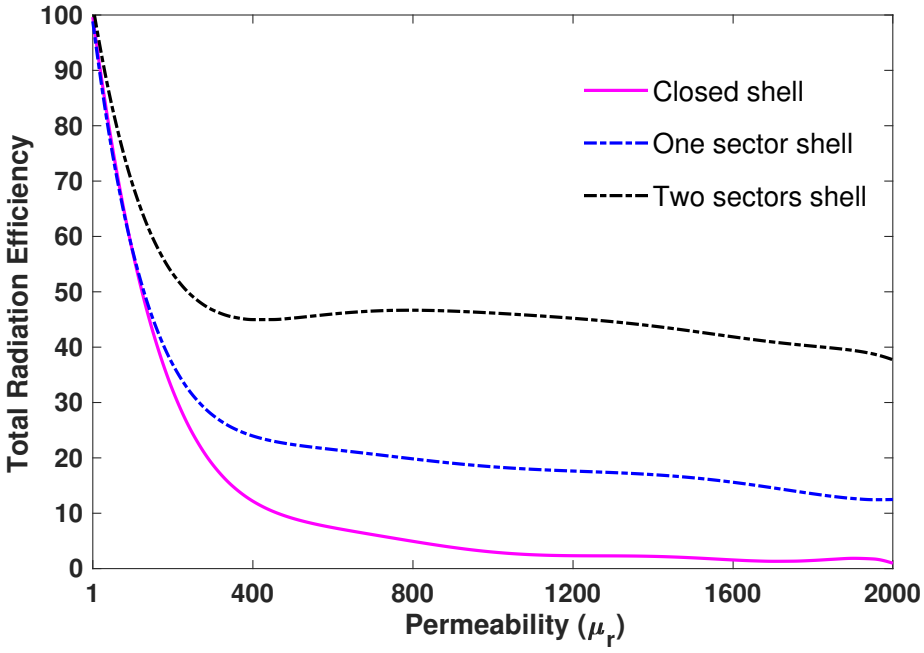

(a)

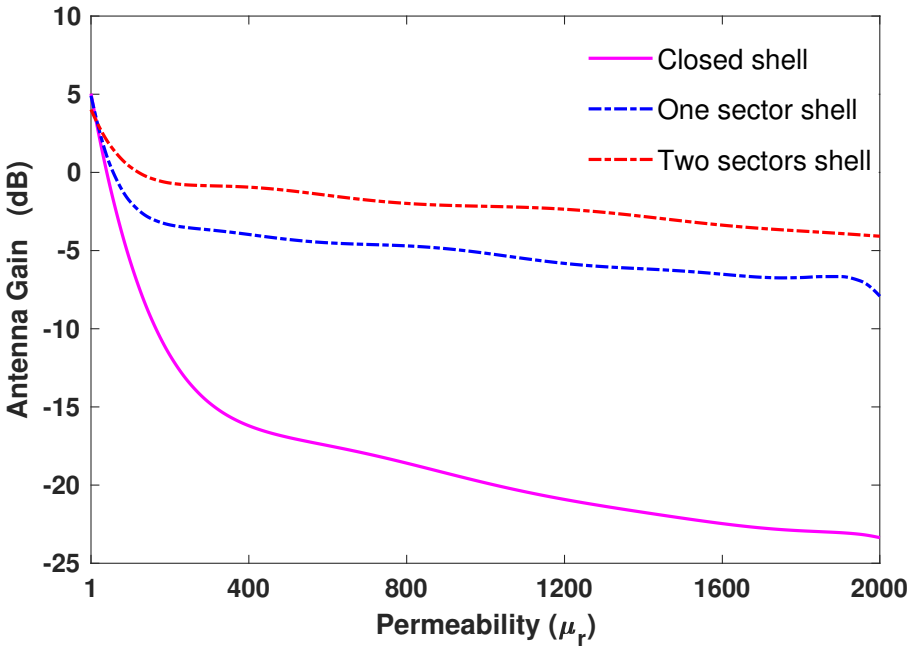

(b)

Figure 5.16: **(a)** The efficiency and **(b)** the gain of the top-loaded monopole antenna for the exact geometrical dimensions of the magnetic material shown in Fig. 5.15.

6. Conclusion and Outlook

Among the main drawbacks of electrically small antennas are the poor input impedance matching, the narrow operating bandwidth, a significant increase in the stored electromagnetic energy, and the drastic reduction in the radiation resistance, particularly when the antenna element is placed inside or outside a lossy medium like in biomedical applications. Therefore, in this thesis we introduce an effective method to improve the performance of electrically small antennas utilizing the natural dispersion in dielectric and magnetic materials. As a result, it was found that the performance of an electrically small antenna can be enhanced by enclosing the antenna element with a highly dispersive dielectric or magnetic material. For instance, when the antenna element is placed in the center of a multi-layered sphere filled with highly dispersive lossy material, the spherical multipole expansion can be utilized to give a complete description of the radiated electromagnetic field of the antenna at any point in the surrounding media. This method accurately evaluates the optimum matching between the antenna element and the surrounding dispersive media. On the other hand, the Kramers-Kronig relations were used throughout the thesis as a solution method to interrelate the real and the imaginary parts of the frequency-dependent permittivity and permeability of the dielectric and magnetic material utilized to enclose the antenna.

Moreover, the Kramers-Kronig transformations were utilized to investigate a practical problem for calculating the electric conductivity of frequency-dependent dielectric or magnetic materials. In frequency-dependent lossy materials, the imaginary part of the complex relative permittivity or permeability includes the conductivity part that depends on the free-moving charges, which is very hard to discern during measurements. However, when measuring any material's permittivity and permeability, the experimental results give only complex-valued relative permittivity and permeability. We utilized the KK-transformations to separate the conductivity from the complex-valued permittivity and permeability. Firstly, the method was numerically investigated and employed on some artificially synthesized materials with randomly selected permittivity and permeability values. After that, the method was verified on natural materials found in the literature.

It was found that the strong reflections of the radiated electromagnetic fields result in poor compatibility between the antenna and the surrounding medium when placed inside or outside a lossy medium, like biomedical tissues. Therefore, we extensively investigated the method of the spherical multipole expansion for expanding the antenna's radiated electromagnetic fields in the multi-layered sphere and its application for evaluating the optimum matching between the antenna element and the surrounding lossy biomedical tissue. Firstly, we assumed that the electrically small antenna element is placed in the center of a three-layered sphere. Furthermore, the medium in the outermost sphere is assumed lossy

with known relative permittivity and permeability values, while the middle sphere contains a dielectric or magnetic material with unknown relative permittivity and permeability values. Consequently, the next step was to find the values of this material's relative permittivity and permeability. By treating the three-layered sphere as a boundary value problem, the multipole amplitudes of the spherical harmonics can be calculated everywhere. Next, the optimal values of the material's relative permittivity and permeability in the middle sphere were calculated by compensating for the stored electromagnetic energies in each sphere. Finally, the robustness of this method was verified by a direct application to natural biomedical tissue like women's breast fat tissues.

Another electrically small antenna, the top-loaded monopole antenna, was investigated in Chapter 5. The numerical study of this type of antenna found in the literature [72], [73] demonstrated that the stored electric energy drastically increases by increasing the top disk radius, which reduces the radiation resistance and makes the antenna unrealizable. Moreover, the operating bandwidth of this type of antenna is very narrow. Therefore, we followed the approach of Yaghjian [72] but by surrounding the monopole antenna with a highly dispersive lossy magnetic material with a frequency-dependent permeability. It was found that the magnetic energy stored in the dispersive magnetic material compensates for the stored electric energy under the top disk, leading to an increase in both the input impedance and the radiation resistance over a broad frequency range. Furthermore, enclosing the antenna with a magnetic material induces an electric dipole moment at the center of the antenna, adding to the electric field's total electric dipole moment and shifting the resonant frequency to lower values. Therefore, enclosing the top-loaded monopole antenna with a highly dispersive magnetic material could reduce the stored electric energy and increase the operating bandwidth of the monopole antenna. However, the reduction in the stored electric energy and the dramatic increase in the operating bandwidth were at the expense of degrading the antenna's radiation efficiency and gain. Consequently, we suggested that the existence of longitudinal slots in the magnetic material could improve both the gain and the radiation efficiency of the top-loaded monopole antenna. The analysis was mathematically performed and numerically verified using the frequency-domain simulator CST©. The obtained results demonstrated the validity of the suggested method by comparing the numerical results with that obtained by the mathematical calculations. The Kramers-Kronig transformations were applied to interrelate the real and the imaginary parts of the frequency-dependent permeability of the magnetic material enclosing the antenna.

Publications that were made throughout the thesis are [25], [45].

As an outlook we note that the matching method between the electrically small antenna and lossy materials like biomedical tissues can be intensively investigated using other types of antennas. For instance, unlike using infinitesimally small electric and magnetic dipoles, the validity of this method should be tested using types of antennas with complicated excitation sources. Moreover, verifying this method by comparing its outputs with experimental results will be of a potential interest in this topic.

A. Derivation of the Kramers-Kronig Integrals

A.1 Cauchy Integrals

Most of the following derivations are taken from [49], [77] with some modifications. One consequence of Cauchy's theorem is that the contour integral of any holomorphic function along a closed contour Γ vanishes [49] as in (A.1):

$$\oint_{\Gamma} \beta(\nu) d\nu = 0 \tag{A.1}$$

where $\beta(\nu) = \beta'(\nu) - j\beta''(\nu)$ is any complex function represented in the complex plane and $\nu = \psi - j\Omega$ is the complex frequency. Cauchy's theorem relates the real and the imaginary parts of $\beta(\nu)$ to one another, i.e., the real part can be computed from the imaginary part and vice versa. Accordingly, for calculating $\beta'(\nu)$ in terms of $\beta''(\nu)$, we consider there is a pole on the real axis of the complex plane at $+\omega_c$ as shown in Fig. A.1. Therefore, equation (A.1) is recast to (A.2) to contain a singular value at $+\omega_c$

$$\oint_{\Gamma} \frac{\beta(\nu) - \beta'(\omega_c)}{\nu - \omega_c} d\nu = 0 \tag{A.2}$$

The numerator is subtracted by $\beta'(\omega_c)$ to prevent the integral from exhibiting a pole at $+\omega_c$. In order to maintain the even and odd symmetries of the complex function $\beta(\nu)$, another term should be introduced to (A.2) to give a pole at the complementary point $-\omega_c$ as

$$\oint_{\Gamma} \left\{ \frac{\beta(\nu) - \beta'(\omega_c)}{\nu - \omega_c} - \frac{\beta(\nu) - \beta'(\omega_c)}{\nu + \omega_c} \right\} d\nu = 0 \tag{A.3}$$

The integral (A.3) can be broken up into an integral on the large semi-circle Γ, an integral on the real axis, and two integrals on the infinitesimal semi-circles (at γ_c and $-\gamma_c$) as

$$\begin{aligned} &\int_{-\infty}^{\infty} \left\{ \frac{\beta(\nu) - \beta'(\omega_c)}{\nu - \omega_c} - \frac{\beta(\nu) - \beta'(\omega_c)}{\nu + \omega_c} \right\} d\nu + \oint_{\gamma_c} \left\{ \frac{\beta(\nu) - \beta'(\omega_c)}{\nu - \omega_c} - \frac{\beta(\nu) - \beta'(\omega_c)}{\nu + \omega_c} \right\} d\nu \\ &+ \oint_{-\gamma_c} \left\{ \frac{\beta(\nu) - \beta'(\omega_c)}{\nu - \omega_c} - \frac{\beta(\nu) - \beta'(\omega_c)}{\nu + \omega_c} \right\} d\nu + \oint_{\Gamma} \left\{ \frac{\beta(\nu) - \beta'(\omega_c)}{\nu - \omega_c} - \frac{\beta(\nu) - \beta'(\omega_c)}{\nu + \omega_c} \right\} d\nu = 0 \end{aligned} \tag{A.4}$$

Since the integral on the real axis is taken sufficiently large (from $-\infty$ and ∞), the radius of the semicircle Γ goes to infinity and its integral vanishes. The first integral of (A.4) refers to the integral on the real axis; thus, it should contain only real frequency ψ. The second

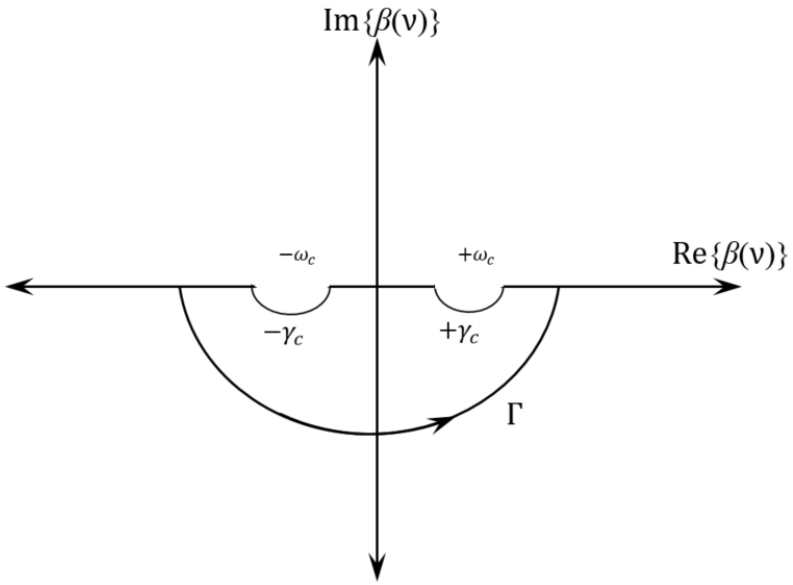

Figure A.1: Manifestation of the contour path Γ of the Cauchy's integral theorem with two poles at $\pm\omega_c$.

integral is performed at $+\omega_c$; thus, the the term $1/(\nu+\omega_c)$ can be neglected because γ_c has only a pole at $-\omega_c$. Likewise, the first term of the third integral can be neglected. After some simplifications, (A.4) is rewritten as

$$\int_{-\infty}^{\infty} \frac{2\omega_c\big\{\beta(\psi)-\beta'(\omega_c)\big\}}{\psi^2-\omega_c^2}d\psi + \oint_{\gamma_c}\frac{\beta(\nu)}{\nu-\omega_c}d\nu + \oint_{-\gamma_c}\frac{\beta(\nu)}{\nu+\omega_c}d\nu = 0 \tag{A.5}$$

The function $\beta(\nu)$ has even and odd properties at the frequency $\pm\omega_c$ defined as

$$\beta(\omega_c) = \beta'(\omega_c) - j\beta''(\omega_c) \quad \text{on the path } +\gamma_c \tag{A.6a}$$

$$\beta(\omega_c) = \beta'(\omega_c) + j\beta''(\omega_c) \quad \text{on the path } -\gamma_c \tag{A.6b}$$

By substituting (A.6) into (A.5) and expanding $\beta(\psi)$ into its real and imaginary parts and after some simplifications, we get

$$\int_{-\infty}^{\infty} \frac{2\omega_c\big\{\beta'(\psi)-j\beta''(\psi)-\beta'(\omega_c)\big\}}{\psi^2-\omega_c^2}d\psi = \oint_{\gamma_c}\frac{j\beta''(\omega_c)}{\nu-\omega_c}d\nu + \oint_{-\gamma_c}\frac{j\beta''(\omega_c)}{\nu+\omega_c}d\nu \tag{A.7}$$

To evaluate the integral on the infinitesimal semicircles $\pm\gamma_c$, we let

$$\nu = \begin{cases} re^{j\theta}+\omega_c & \text{at} \quad +\omega_c \\ re^{j\theta}-\omega_c & \text{at} \quad -\omega_c \end{cases}$$

where r is the radius of the infinitesimal semicircles and $0 \le \theta \le \pi$. The integrals of the right side of (A.7) are calculated as

$$j\beta''(\omega_c)\oint_{\gamma_c}\frac{jre^{j\theta}}{re^{j\theta}}d\theta + j\beta''(\omega_c)\oint_{-\gamma_c}\frac{jre^{j\theta}}{re^{j\theta}}d\theta = -2\pi\beta''(\omega_c) \tag{A.8}$$

By substituting (A.8) into (A.7) and after some simplifications, we get

$$\beta''(\omega_c) = \frac{-2\omega_c}{\pi} \int_0^\infty \frac{\beta'(\psi) - \beta'(\omega_c)}{\psi^2 - \omega_c^2} d\psi \tag{A.9}$$

It is evident in (A.9) that the imaginary part of $\beta(\nu)$ at a frequency ω_c can be expressed in terms of its real part.
For evaluating the real part of $\beta(\nu)$ in terms of its imaginary part, we interchange the real and the imaginary parts of (A.3). This can be accomplished by multiplying $\beta(\nu)$ by $(j\nu)$ to get

$$j\nu\beta(\nu) = \tilde{\beta}(\nu) = j\nu\beta'(\nu) + \nu\beta''(\nu) \tag{A.10}$$

where $\tilde{\beta}(\nu) = \tilde{\beta}'(\nu) - j\tilde{\beta}''(\nu)$. Equation (A.3) can be recast to (A.11) using equation (A.10).

$$\oint_\Gamma \left\{ \frac{\tilde{\beta}(\nu) - \tilde{\beta}'(\omega_c)}{\nu - \omega_c} - \frac{\tilde{\beta}(\nu) - \tilde{\beta}'(\omega_c)}{\nu + \omega_c} \right\} d\nu = 0 \tag{A.11}$$

The even and odd symmetries of the real and the imaginary parts of $\tilde{\beta}(\nu)$ are expressed as

$$\tilde{\beta}'(\nu) = \nu\beta''(\nu) \qquad \text{even function} \tag{A.12a}$$

$$\tilde{\beta}''(\nu) = -\nu\beta'(\nu) \qquad \text{odd function} \tag{A.12b}$$

By following the same procedure applied on (A.5)-(A.9), the real part of $\beta(\nu)$ is calculated at ω_c in terms of the imaginary part according to

$$\beta'(\omega_c) = \frac{2}{\pi} \int_0^\infty \frac{\psi\beta''(\psi) - \omega_c\beta''(\omega_c)}{\psi^2 - \omega_c^2} d\psi \tag{A.13}$$

By replacing $\omega_c = \omega$ in (A.9) and (A.13), the real and the imaginary parts of $\beta(\nu)$ can be calculated over the whole frequency range $0 \leq \omega \leq \infty$. These integrals are also known as the Kramers-Kronig relations. It is evident from the above derivations that the real and the imaginary parts of any frequency-dependent complex function are interrelated, provided that this function has an analytical continuation in the complex frequency domain.

B. Derivation of the Stored Energy in Dispersive Material

B.1 Landau Approach

The energy associated with the electromagnetic fields can be described by the instantaneous Poynting vector [26] as

$$\vec{S} = \vec{E} \times \vec{H} \tag{B.1}$$

The following derivations are taken from [26], [63]. By applying the divergence theorem and using the identity $\left[\nabla \cdot (\vec{E} \times \vec{H}) = (\nabla \times \vec{E}) \cdot \vec{H} - (\nabla \times \vec{H}) \cdot \vec{E}\right]$ and the Maxwell's equations (2.1a) and (2.1b), equation (B.1) can be written as

$$\nabla \cdot \vec{S} = -(\vec{E} \cdot \frac{\partial \vec{D}}{\partial t} + \vec{H} \cdot \frac{\partial \vec{B}}{\partial t}) - \vec{E} \cdot \vec{J} \tag{B.2}$$

The first term of the right side of (B.2) represents the time varying electromagnetic energy density, which is defined as

$$\begin{aligned} \frac{\partial w}{\partial t} &= \frac{\partial w_e}{\partial t} + \frac{\partial w_m}{\partial t} \\ &= \vec{E} \cdot \frac{\partial \vec{D}}{\partial t} + \vec{H} \cdot \frac{\partial \vec{B}}{\partial t} \end{aligned} \tag{B.3}$$

where w_e and w_m are the electric and the magnetic energy densities, respectively. Since we are interested in the absolute value of the electromagnetic energy density, (B.1) is rewritten as

$$\langle \vec{S} \rangle = \frac{1}{2} \mathrm{Re}\{\vec{E} \times \vec{H}^*\} \tag{B.4}$$

and (B.3) as

$$\langle \nabla \cdot \vec{S} \rangle = \frac{1}{4} \{ \vec{E} \cdot \frac{\partial \vec{D}^*}{\partial t} + \vec{E}^* \cdot \frac{\partial \vec{D}}{\partial t}) \} \tag{B.5}$$

The time-varying electric and magnetic fields are represented by

$$\vec{E}(t) = \vec{E}_o(t) e^{j\omega t} \tag{B.6a}$$

$$\vec{H}(t) = \vec{H}_o(t) e^{j\omega t} \tag{B.6b}$$

where $\vec{E}_o(t)$ and $\vec{H}_o(t)$ are considered to vary slowly with respect to $2\pi/\omega$. Using Fourier series [65], $\vec{E}_o(t)$ is expanded as

$$\vec{E}_o(t) = \sum_{\phi} \vec{E}_\phi e^{j\phi t} \tag{B.7}$$

where $\phi \ll \omega$. The partial derivative of the electric field density in (B.5) can be written in the frequency domain using Fourier transforms as

$$\frac{\partial \vec{D}}{\partial t} = \xi(\omega)\vec{E} = j\omega\varepsilon(\omega)\vec{E} \tag{B.8}$$

By substituting (B.6a) and (B.7) into (B.8) we get

$$\frac{\partial \vec{D}}{\partial t} = \xi(\omega+\phi)\vec{E}_\phi e^{j(\phi+\omega)t} \tag{B.9}$$

The term $\xi(\omega+\phi)$ can be expanded utilizing Taylor series as

$$\xi(\omega+\phi) = \xi(\omega) + \phi\frac{d\xi(\omega)}{d\omega} + \frac{\phi^2}{2}\frac{d^2\xi(\omega)}{d\omega^2} + ... \tag{B.10}$$

By neglecting the high order terms of ϕ, (B.9) is recast to

$$\frac{\partial \vec{D}}{\partial t} = \xi(\omega)\vec{E}_\phi e^{j(\phi+\omega)t} - j\frac{d\xi(\omega)}{d\omega}\frac{d\vec{E}_\phi}{dt}e^{j\omega t} \tag{B.11}$$

Using the definition of $\xi(\omega)$ in (B.8), (B.11) can be rewritten as

$$\frac{\partial \vec{D}}{\partial t} = j\omega\varepsilon(\omega)\vec{E}_o(t)e^{j\omega t} + \frac{d\{\omega\varepsilon(\omega)\}}{d\omega}\frac{d\vec{E}_\phi}{dt}e^{j\omega t} \tag{B.12}$$

Substitute (B.12) into (B.5) and neglect the imaginary parts of $\varepsilon(\omega)$, then the time-averaged electric energy density can be represented as

$$\frac{\partial w_e}{\partial t} = \frac{1}{4}\frac{d\{\omega\varepsilon(\omega)\}}{d\omega}\frac{d}{dt}\{\vec{E}\cdot\vec{E}^*\} \tag{B.13}$$

Likewise for the magnetic energy density

$$\frac{\partial w_m}{\partial t} = \frac{1}{4}\frac{d\{\omega\mu(\omega)\}}{d\omega}\frac{d}{dt}\{\vec{H}\cdot\vec{H}^*\} \tag{B.14}$$

From (B.13) and (B.14), the total time-averaged energy density can be written as

$$W = \frac{1}{2}\left\{\frac{d\{\omega\varepsilon(\omega)\}}{d\omega} \mid \vec{E} \mid^2 + \frac{d\{\omega\mu(\omega)\}}{d\omega} \mid \vec{H} \mid^2\right\} \tag{B.15}$$

It is evident in (B.15) that time-averaged energy density in a frequency-dependent medium depends on the frequency-dependent permittivity $\varepsilon(\omega)$ and permeability $\mu(\omega)$. Equation (B.15) will be used throughout the thesis for calculating the internally stored electromagnetic energies in dispersive materials.

List of Symbols

Symbol	Description
$\vec{E}$	Electric field intensity in V/m
$\vec{H}$	Magnetic field intensity in A/m
$\vec{B}$	Magnetic flux density Wb/m
$\vec{D}$	Electric flux density Coul/m
$\vec{J}_e, \vec{J}_m$	Electric and magnetic current densities A/m^2, V/m^2
$\vec{M}$	Magnetization A/m
ϱ	Electric charge density Coul/m^3
I_e, I_m	Electric current (A) and magnetic current (V)
J_e^{imp}, J_m^{imp}	The impressed electric and magnetic currents in A and V
ε_0, μ_0	The permittivity and permeability of free space in F/m and H/m
ε_r, μ_r	The relative permittivity and the relative permeability
ε_{eff}	The effective relative permittivity
κ	The wavenumber 1/m
$\varepsilon = \varepsilon' - j\varepsilon''$	Complex relative permittivity
$\mu = \mu' - j\mu''$	Complex relative permeability
χ_e, χ_m	The electric and the magnetic susceptibilities
σ_e	The electric conductivity in S/m
η	The intrinsic impedance in Ω
W_e, W_m	The time-averaged electric and magnetic stored energies Joule/m^3
P_{rad}, P_{acc}, P_l	The radiation, accepted, and loss powers in Watt
ω	The angular frequency rad/ s
m_{i_e}, m_{i_m}	The dipole moments due to the electric and magnetic currents, respectively
R_r, R_{in}	The radiation and input resistances in Ω
$G(\omega), D(\omega)$	The gain and directivity of the antenna

Bibliography

[1] M. D. Haslam and B. Raeymaekers, "A Composite Index to Quantify Dispersion of Carbon Nanotubes in Polymer-based Composite Materials," *Composites Part B: Engineering*, vol. 55, pp. 16–21, 2013.

[2] T. Tsutaoka, M. Ueshima, T. Tokunaga, T. Nakamura, and K. Hatakeyama, "Frequency Dispersion and Temperature Variation of Complex Permeability of Ni-Zn Ferrite Composite Materials," *Journal of Applied Physics*, vol. 78, no. 6, pp. 3983–3991, 1995.

[3] T. Nakamura, T. Tsutaoka, and K. Hatakeyama, "Frequency Dispersion of Permeability in Ferrite Composite Materials," *Journal of Magnetism and Magnetic Materials*, vol. 138, no. 3, pp. 319–328, 1994.

[4] B. Nøst, B. Hansen, and E. Haslund, "Dielectric Dispersion of Composite Material," *Physica Scripta*, vol. 1992, no. T44, p. 67, 1992.

[5] P. Wells, "Absorption and Dispersion of Ultrasound in Biological Tissue," *Ultrasound in Medicine and Biology*, vol. 1, no. 4, pp. 369–376, 1975.

[6] D. G. Stavenga, H. L. Leertouwer, and B. D. Wilts, "Quantifying the Refractive Index Dispersion of a Pigmented biological tissue using jamin–lebedeff interference microscopy," *Light: Science and Applications*, vol. 2, no. 9, pp. e100–e100, 2013.

[7] R. Pelluri, N. Gupta, and B. Appasani, "A multi Band Absorber Using Band Gap Structures," in *2015 International Conference on Microwave and Photonics (ICMAP)*. IEEE, 2015, pp. 1–2.

[8] F. Costa, A. Kazemzadeh, S. Genovesi, and A. Monorchio, "Electromagnetic Absorbers Based on Frequency Selective Surfaces," in *Forum Electromagn. Res. Methods Appl. Technol.*, vol. 37, no. 1, 2016, pp. 1–23.

[9] Y. He, W. Feng, S. Guo, J. Wei, Y. Zhang, Z. Huang, C. Li, L. Miao, and J. Jiang, "Design of a Dual-band Electromagnetic Absorber with Frequency Selective Surfaces," *IEEE Antennas and Wireless Propagation Letters*, vol. 19, no. 5, pp. 841–845, 2020.

[10] E. Sano and E. Akiba, "Electromagnetic Absorbing Materials Using Nonwoven Fabrics Coated with Multi-walled Carbon Nanotubes," *Carbon*, vol. 78, pp. 463–468, 2014.

[11] D. Micheli, R. Pastore, C. Apollo, M. Marchetti, G. Gradoni, V. M. Primiani, and F. Moglie, "Broadband Electromagnetic Absorbers Using Carbon Nanostructure-based Composites," *IEEE Transactions on Microwave Theory and Techniques*, vol. 59, no. 10, pp. 2633–2646, 2011.

[12] F. M. Idris, M. Hashim, Z. Abbas, I. Ismail, R. Nazlan, and I. R. Ibrahim, "Recent Developments of Smart Electromagnetic Absorbers Based Polymer-composites at Gigahertz Frequencies," *Journal of Magnetism and Magnetic Materials*, vol. 405, pp. 197–208, 2016.

[13] A. D. Yaghjian, "Overcoming the Chu Lower Bound on Antenna Q with Highly Dispersive Lossy Material," *IET Microwaves, Antennas and Propagation*, vol. 12, no. 4, pp. 459–466, 2018.

[14] A. Arbabi and S. Safavi-Naeini, "Maximum Gain of a Lossy Antenna," *IEEE Transactions on Antennas and Propagation*, vol. 60, no. 1, pp. 2–7, 2011.

[15] A. Karlsson, "Physical Limitations of Antennas in a Lossy Medium," *IEEE Transactions on Antennas and Propagation*, vol. 52, no. 8, pp. 2027–2033, 2004.

[16] C. Niamien, S. Collardey, A. Sharaiha, and K. Mahdjoubi, "Compact Expressions for Efficiency and Bandwidth of Patch Antennas Over Lossy Magneto-dielectric Materials," *IEEE Antennas and Wireless Propagation Letters*, vol. 10, pp. 63–66, 2011.

[17] K. Ito, K. Saito, T. Taniguchi, and H. Yoshimura, "Temperature Distribution in and Around Array Applicator for Interstitial Microwave Hyperthermia Combined with Interstitial Radiation Therapy," *Proc. 27th Intl. URSI Gen. Assembly, Maastricht*, 2002.

[18] G. M. Vlăsceanu, R.-M. Amărandi, M. Ioniță, T. Tite, H. Iovu, L. Pilan, and J. S. Burns, "Versatile Graphene Biosensors for Enhancing Human Cell Therapy," *Biosensors and Bioelectronics*, vol. 117, pp. 283–302, 2018.

[19] C. Gabriel and A. Peyman, "Dielectric Properties of Biological Tissues; Variation with Age," *Conn's Handbook of Models for Human Aging*, pp. 939–952, 2018.

[20] G. R. Rani and G. Raju, "Transmission and Reflection Characteristics of Electromagnetic Energy in Biological Tissues," *International Journal of Electronics and Communication Engineering*, vol. 6, no. 1, pp. 119–129, 2013.

[21] H. Cano-Garcia, P. Kosmas, and E. Kallos, "Enhancing Electromagnetic Transmission Through Biological Tissues at Millimeter Waves Using Subwavelength Metamaterial Antireflection Coatings," in *2015 9th International Congress on Advanced Electromagnetic Materials in Microwaves and Optics (Metamaterials)*. IEEE, 2015, pp. 43–45.

[22] E. Handoko, A. Mangasi, S. Iwan, M. Randa, and M. Alaydrus, "Measurement of Complex Permittivity and Permeability of Hexagonal Ferrite Composite Material Using a Waveguide in Microwave Band," in *2016 International Conference on Radar, Antenna, Microwave, Electronics, and Telecommunications (ICRAMET)*. IEEE, 2016, pp. 28–30.

[23] G. G. Bellizzi, K. Sumser, and M. T. Bevacqua, "On the Optimal Matching Medium and the Working Frequency in Deep Pelvic Hyperthermia," *IEEE Journal of Electromagnetics, RF and Microwaves in Medicine and Biology*, vol. 5, no. 3, pp. 223–230, 2020.

[24] A. Arayeshnia, A. Madannejad, J. Ebrahimizadeh, F. Ravanbakhsh, M. D. Perez, and R. Augustine, "Miniaturized CPW-fed Bowtie Slot Antenna for Wearable Biomedical Applications," in *2020 14th European Conference on Antennas and Propagation (EuCAP)*. IEEE, 2020, pp. 1–4.

[25] M. Bakry and L. Klinkenbusch, "Application of Kramers-Kronig Transformations to Increase the Bandwidth of Small Antennas," *Advances in Radio Science*, vol. 17, no. B., pp. 65–70, 2019.

[26] J. D. Jackson, *Classical Electrodynamics*. Wiley and Sons, Inc., 1999.

[27] D. M. Pozar, *Microwave Engineering*. John Wiley & Sons, 2009.

[28] L. Klinkenbusch, *Feldtheorie III: Sphärische Multipolanalyse, Vorlesungsmanuskript*. Ruhr-Universität, Bochum, 1998.

[29] I. L. Rasskazov, A. Moroz, and P. S. Carney, "Electromagnetic Energy in Multilayered Spherical Particles," *JOSA A*, vol. 36, no. 9, pp. 1591–1601, 2019.

[30] C. H. Ziener, F. T. Kurz, L. R. Buschle, and T. Kampf, "Orthogonality, Lommel Integrals and Cross Product Zeros of Linear Combinations of Bessel Functions," *SpringerPlus*, vol. 4, no. 1, pp. 1–26, 2015.

[31] R. O'Connell, "The Equation of Motion of an Electron," *Physics Letters A*, vol. 313, no. 5-6, pp. 491–497, 2003.

[32] N. W. Ashcroft and N. D. Mermin, "Solid State Physics. Thomson Learning," *Inc., Florence*, 1976.

[33] V. Lucarini, J. J. Saarinen, K.-E. Peiponen, and E. M. Vartiainen, *Kramers-Kronig Relations in Optical Materials Research*. Springer Science and Business Media, 2005, vol. 110.

[34] S. Mustafaeva, "Frequency Dispersion of Dielectric Coefficients of Layered TlGaS2 Single Crystals," *Physics of the Solid State*, vol. 46, no. 6, pp. 1008–1010, 2004.

[35] S. Kumar, B. Lively, L. Sun, B. Li, and W. Zhong, "Highly Dispersed and Electrically Conductive Polycarbonate/Oxidized Carbon Nanofiber Composites for Electrostatic Dissipation Applications," *Carbon*, vol. 48, no. 13, pp. 3846–3857, 2010.

[36] T.-M. Pan, C.-S. Liao, H.-H. Hsu, C.-L. Chen, J.-D. Lee, K.-T. Wang, and J.-C. Wang, "Excellent Frequency Dispersion of Thin Gadolinium Oxide High-k Gate Dielectrics," *Applied Physics Letters*, vol. 87, no. 26, p. 262908, 2005.

[37] J. Sethuraman and R. Sirohi, "Dispersion Relations in Fraunhofer Diffraction," *JOSA*, vol. 69, no. 6, pp. 907–909, 1979.

[38] H. A. Kramers, "La Diffusion de la Lumiere par les Atomes," in *Atti Cong. Intern. Fisica (Transactions of Volta Centenary Congress) Como*, vol. 2, 1927, pp. 545–557.

[39] R. d. L. Kronig, "On the Theory of Dispersion of X-rays," *Josa*, vol. 12, no. 6, pp. 547–557, 1926.

[40] H. M. Nussenzveig, *Causality and Dispersion Relations*. Academic, New York, 1972.

[41] M. Urquidi-Macdonald, S. Real, and D. D. Macdonald, "Applications of Kkramers—Kronig Transforms in the Analysis of Electrochemical Impedance Data—III. Stability and Linearity," *Electrochimica Acta*, vol. 35, no. 10, pp. 1559–1566, 1990.

[42] D. D. Macdonald and M. Urquidi-Macdonald, "Kramers-Kronig Transformation of Constant Phase Impedances," *Journal of The Electrochemical Society*, vol. 137, no. 2, pp. 515–517, 1990.

[43] M. Schönleber, D. Klotz, and E. Ivers-Tiffée, "A method for Improving the Robustness of Linear Kamers-Kronig Validity Tests," *Electrochimica Acta*, vol. 131, pp. 20–27, 2014.

[44] S. C. Chapra, R. P. Canale *et al.*, *Numerical Methods for Engineers*. Boston: McGraw-Hill Higher Education,, 2010.

[45] M. Bakry and L. Klinkenbusch, "Using the Kramers-Kronig Transforms to Retrieve the Conductivity from the Effective Complex Permittivity," *Advances in Radio Science*, vol. 16, no. B., pp. 23–28, 2018.

[46] C. A. Hall and W. W. Meyer, "Optimal Error Bounds for Cubic Spline Interpolation," *Journal of Approximation Theory*, vol. 16, no. 2, pp. 105–122, 1976.

[47] N. Li, G.-W. Huang, Y.-Q. Li, H.-M. Xiao, Q.-P. Feng, N. Hu, and S.-Y. Fu, "Enhanced Microwave Absorption Performance of Coated Carbon Nanotubes by Optimizing the Fe3O4 Nanocoating Structure," *ACS applied materials and interfaces*, vol. 9, no. 3, pp. 2973–2983, 2017.

[48] L. Kong, C. Wang, X. Yin, X. Fan, W. Wang, and J. Huang, "Electromagnetic Wave absorption Properties of a Carbon Nanotube Modified by a Tetrapyridinoporphyrazine Interface Layer," *Journal of Materials Chemistry C*, vol. 5, no. 30, pp. 7479–7488, 2017.

[49] J. Mathews and R. Howell, *Complex Aanalysis for Mathematics and Engineering*. Jones and Bartlett Publishers, 2012.

[50] N. Hu, *Composites and Their Properties*. BoD–Books on Demand, 2012.

[51] S. M. Yadav and K. B. Yusoh, "Mechanical and Physical Properties of Wood-plastic Composites Made of Polypropylene, Wood Flour and Nanoclay," *Proceeding-Kuala Lumpur International Agriculture, Forestry and Plantation September*, pp. 12–13, 2015.

[52] J.-M. Oh, T. T. Biswick, and J.-H. Choy, "Layered Nanomaterials for Green Materials," *Journal of Materials Chemistry*, vol. 19, no. 17, pp. 2553–2563, 2009.

[53] J. A. Schuller, S. Karaveli, T. Schiros, K. He, S. Yang, I. Kymissis, J. Shan, and R. Zia, "Orientation of Luminescent Excitons in Layered Nanomaterials," *Nature Nanotechnology*, vol. 8, no. 4, p. 271, 2013.

[54] S. Stankovich, D. A. Dikin, G. H. Dommett, K. M. Kohlhaas, E. J. Zimney, E. A. Stach, R. D. Piner, S. T. Nguyen, and R. S. Ruoff, "Graphene-based Composite Materials," *Nature*, vol. 442, no. 7100, p. 282, 2006.

[55] Y. Zhang, Z.-R. Tang, X. Fu, and Y.-J. Xu, "TiO2- Graphene Nanocomposites for Gas-phase Photocatalytic Degradation of Volatile Aromatic Pollutant: is TiO2-Graphene Truly Different from Other TiO2- Carbon Composite Materials?" *ACS Nano*, vol. 4, no. 12, pp. 7303–7314, 2010.

[56] J. Gittleman and B. Abeles, "Comparison of the Effective Medium and the Mmaxwell-Garnett Predictions for the Dielectric Constants of Ganular Metals," *Physical Review B*, vol. 15, no. 6, p. 3273, 1977.

[57] E. M. Cheng, M. F. B. A. Malek, M. Ahmed, K. Y. You, K. Y. Lee, and H. Nornikman, "The Use of Dielectric Mixture Equations to Analyze the Dielectric Properties of a Mixture of Rubber Tire Dust and Rice Husks in a Microwave Absorber," *Progress in Electromagnetics Research*, vol. 129, pp. 559–578, 2012.

[58] M. Y. Koledintseva, R. E. DuBroff, and R. W. Schwartz, "Maxwell Garnett Model for Dielectric Mixtures Containing Conducting Particles at Optical Frequencies," MISSOURI UNIV-ROLLA, Tech. Rep., 2006.

[59] Z. Wang and Z. Guang-Lin, "Microwave Absorption Properties of Carbon Nanotubes-epoxy Composites in a Frequency Range of 2-20 GHz," *Open Journal of Composite Materials*, vol. 3, no. 2, p. 17, 2013.

[60] A. D. Yaghjian, M. Gustafsson, and L. Jonsson, "Minimum Q for Lossy and Lossless Electrically Small Dipole Antennas," *Progress in Electromagnetics Research*, vol. 143, pp. 641–673, 2013.

[61] C. A. Balanis, *Antenna Theory: Analysis and Design*. John Wiley & Sons, 2016.

[62] A. D. Yaghjian, "Internal Energy, Q-Energy, Poynting's Theorem, and the Stress Dyadic in Dispersive Material," *IEEE Transactions on Antennas and Propagation*, vol. 55, no. 6, pp. 1495–1505, 2007.

[63] F. D. Nunes, T. C. Vasconcelos, M. Bezerra, and J. Weiner, "Electromagnetic Energy Density in Dispersive and Dissipative Media," *JOSA B*, vol. 28, no. 6, pp. 1544–1552, 2011.

[64] J. S. McLean, "A Re-examination of the Fundamental Limits on the Radiation Q of Electrically Small Antennas," *Transactions on Antennas and Propagation*, vol. 44, no. 5, p. 672, 1996.

[65] L. D. Landau, J. Bell, M. Kearsley, L. Pitaevskii, E. Lifshitz, and J. Sykes, *Electrodynamics of Continuous Media*. Elsevier, 2013, vol. 8.

[66] O. B. Debnath, K. Ito, K. Saito, and M. Uesaka, "Design of Invasive and Non-invasive Antennas for the Combination of Microwave-hyperthermia with Radiation Therapy," in *2015 IEEE MTT-S 2015 International Microwave Workshop Series on RF and Wireless Technologies for Biomedical and Healthcare Applications (IMWS-BIO)*. IEEE, 2015, pp. 71–72.

[67] T. P. Ryan and C. L. Brace, "Interstitial microwave treatment for cancer: historical basis and current techniques in antenna design and performance," *International Journal of Hyperthermia*, vol. 33, no. 1, pp. 3–14, 2017.

[68] S. Di Meo, L. Pasotti, I. Iliopoulos, M. Pasian, M. Ettorre, M. Zhadobov, and G. Matrone, "Tissue-Mimicking Materials for Breast Phantoms up to 50 GHz," *Physics in Medicine and Biology*, vol. 64, no. 5, p. 055006, 2019.

[69] L. J. Chu, "Physical Limitations of Omni-directional Antennas," *Journal of Applied Physics*, vol. 19, no. 12, pp. 1163–1175, 1948.

[70] R. C. Hansen and R. E. Collin, *Small Antenna Handbook*. Wiley Online Library, 2011.

[71] A. D. Yaghjian and H. R. Stuart, "Lower Bounds on the Q of Electrically Small Dipole Antennas," *IEEE Transactions on Antennas and Propagation*, vol. 58, no. 10, pp. 3114–3121, 2010.

[72] H. R. Stuart and A. D. Yaghjian, "Approaching the Lower Bounds on Q for Electrically Small Electric-dipole Antennas Using High Permeability Shells," *IEEE Transactions on Antennas and Propagation*, vol. 58, no. 12, pp. 3865–3872, 2010.

[73] Z. Hu, Z. Shen, W. Wu, and J. Lu, "Low-profile Top-hat Monopole Yagi Antenna for End-fire Radiation," *IEEE Transactions on Antennas and Propagation*, vol. 63, no. 7, pp. 2851–2857, 2015.

[74] A. D. Yaghjian and S. R. Best, "Impedance, Bandwidth, and Q of Antennas," *IEEE Transactions on Antennas and Propagation*, vol. 53, no. 4, pp. 1298–1324, 2005.

[75] W. C. Chew and J. A. Kong, "Effects of Fringing Fields on the Capacitance of Circular Microstrip Disk," *IEEE Transactions on Microwave Theory and Techniques*, vol. 28, no. 2, pp. 98–104, 1980.

[76] H. A. Wheeler, "A Helical Antenna for Circular Polarization," *Proceedings of the IRE*, vol. 35, no. 12, pp. 1484–1488, 1947.

[77] G. B. Kauffman, "Electrochemical Impedance Spectroscopy. By Mark E. Orazem and Bernard Tribollet." 2009.